Performance Enhancement of Thermal Energy Storage System using Bio-based Composite PCM

by

Soroush Ebadi

A Thesis

presented to

The University of Guelph

In partial fulfilment of requirements
for the degree of

Master of Applied Science

in

Engineering

Guelph, Ontario, Canada

ABSTRACT

PERFORMANCE ENHANCEMENT OF THERMAL ENERGY STORAGE USING BIO-BASED COMPOSITE PCM

Soroush Ebadi
MASc, University of Guelph, 2018

Advisors:
Dr. Shohel Mahmud
Dr. Amir A. Aliabadi

Latent Heat Thermal Energy Storage (LHTES) systems have been used in many applications such as solar energy for storing heat, thermal management of electronic devices, and thermal management of buildings. Phase Change Materials (PCM) are the storage medium used in LHTES systems used to store the thermal energy. PCMs suffer from their low thermal conductivity, which significantly affects the performance of LHTES systems. Different approaches for enhancing the thermal conductivity of PCMs including dispersing highly conductive nanoparticle to the PCM, using metal fins, and displacing conductive porous material into the PCM have been proposed by the researchers. In the present study, effects of dispersing nanoparticles into PCM and displacing porous material to the PCM filled a vertical cylindrical LHTES system have been numerically and experimentally investigated. Copper oxide nanoparticles and copper mesh were used to improve the thermal conductivity of the PCMs.

Dedication

At first I would like to give my sincerest and humble thank to the Almighty, the most gracious and the most merciful

To my beloved parent, sister and brother

To all my teachers

To all my friends

Acknowledgement

I would like to express my humble and sincere thanks to my advisors Dr. Shohel Mahmud and Dr. Amir A. Aliabadi for their endless effort, guidance and support to successfully complete my thesis. Their kind concern and encouragement of thinking new ideas and to implement them practically helped me to finish my graduate studies and research work. Their motivation and recommendation helped me to go one step ahead towards PhD program.

I am thankful to Dr. Syeda Tasnim, who helped me time to time by giving useful suggestions and guidance in the completion of my thesis work. The author would like to thank graduate office staff for their support. I am also thankful to Mike Speagle for his help in lab activities. Besides, I would like to thank all of my lab mates. I got their utmost attentions and help when I needed most which I really appreciate.

I am also thankful to Ministry of Research and Innovation, Ontario and NSERC Canada for the financial support through my supervisor's ERA, Discovery, and Engage Grants.

Finally, I am extremely thankful to my family members for their unconditional love, support and blessings throughout my life.

Table of Contents

List of Figures

Chapter 2

Chapter 3

Chapter 4

Part I

Part II

Chapter 5

List of Tables

Chapter 2

Chapter 3

Chapter 4

Part II

Chapter 5

Co-Authorship Statement

The research described within this thesis was developed collaboratively by Soroush Ebadi, Dr. Shohel Mahmud, and Dr. Amir A. Aliabadi. The research contained within the five chapters was developed to address two different approaches for enhancing the thermal performance of a cylindrical LHTES system. All initial drafts of the manuscripts prepared for this thesis were prepared by Ebadi and were later reviewed by Mahmud and Aliabadi.

Chapter 1

1.1. Introduction

1.1.1. Background

Nowadays, the global warming concern due to burning of fossil fuels, limitation in the natural gas and oil reservoirs, and increase in the worldwide population have forced researchers and energy suppliers to develop alternative clean energy systems such as renewable energies or using the energy more efficiently. Thermal Energy Storage (TES) systems are one of the systems developed with the aim of storing/ releasing thermal energy efficiently that can balance the ratio between demand and supply. Sensible heat TES system, latent heat TES system, thermos-chemical TES systems are the three major groups of TES systems. Latent heat TES systems have two main advantages over the other type which are including as (i) the potential of storing more energy and (ii) releasing the thermal energy at a constant temperature during the operations. As a result, more efforts have been made by researchers to improve the performance of latent heat TES systems. Latent heat TES systems can be used in solar thermal power plants to store the excess amount of heat and release that at the demand time, in buildings for heating and cooling purposes, and in thermal management applications especially cooling down the electronic devices. LHTES systems use specific materials to store the thermal energy, which are known as Phase Change Materials (PCMs). PCMs have a specific melting temperature which the phase change process happens at this temperature. In other words, if the surrounding temperature is higher than melting point of the PCM, the melting process occurs while solidification process occurs if the surrounding temperature is lower than melting point of the PCM. A wide range of PCMs including hydrated salts, paraffin waxes, organic, and non-organic compounds with different melting temperatures are available in the market that could be used in a LHTES system as the storage medium. Although PCMs have proper features for storing thermal energy, they suffer from a low thermal conductivity, which degrades the performance of a LHTES system. Having low thermal conductivity leads to a lower heat transfer rate during charging (melting) and discharging (solidifications).Various method for improving the thermal conductivity of PCMs have been purposed by researchers which can be categorized as follows : (i) optimizing the geometry of PCMs container which can enhance the natural convection during operation, (ii) inserting metal fins to the PCM’s container which enhanced the effective heat transfer surface area, (iii) dispersing

highly conductive nanoparticles into the PCM, and (iv) displacing conductive porous medium inside the PCM's container. In this thesis focuses on the using porous medium and nanoparticles to enhance the thermal performance of a cylindrical LHTES system. To do so, several experimental setups and numerical simulations have been developed to study the different aspects of using nanoparticles and porous material for enhancing the thermal conductivity of PCMs.

1.1.2. Motivation and Objectives

The motivation of this thesis was to design and develop an efficient cylindrical LHTES system that can be used for heating/ cooling purposes of the buildings or storing the thermal energy generated by the solar thermal systems.

The overall objectives behind this research work include:

Conducting a comprehensive literature review on the status of LHTES systems.

Developing several experimental setups to investigate the thermal performance of a cylindrical LHTES system with different operating conditions such as various volume/weight fractions of nanoparticles, different porosities of porous material and different isothermal boundary conditions.

Developing various simulation models using COMSOL multiphysics to study the details of heat transfer phenomenon during the charging process of a cylindrical LHTES system.

1.1.3. Scope of this Research

The research work is divided into five chapters based on the overall objectives. An overview of each of the chapter follows.

Chapter 2: Melting of Nano-PCM (Copper Oxide Nanoparticles Dispersed into Coconut Oil) inside a Cylindrical Thermal Energy Storage System: Numerical Study

In this chapter, a numerical investigation on the detailed melting process of a bio-based nano-PCM (i.e. copper oxide nanoparticles dispersed into coconut oil) has been performed. A comparison between different aspects of using nano-PCM instead of pure PCM such as the rate of melting fraction, the trend of Nusselt number, and the amount of energy stored inside a cylindrical LHTES system have been conducted.

Chapter 3: Detailed Experimental Investigation of the Melting Process of a Bio-based Nano-PCM (Copper Oxide Nanoparticles Dispersed into Coconut Oil) filled Vertical Cylindrical Thermal Energy Storage System

This chapter presents an experimental investigation on the thermal characteristics of a cylindrical LHTES system filled with nano-PCM. The nano-PCM was prepared by dispersing copper oxide nano-particles into coconut oil. Different procedures by using a magnetic stirrer and an ultrasound sonicator were performed to ensure the homogeneity of the nano-PCM mixture. Melting visualization for c-LHTES filled with nano-PCM and bio-based PCM was performed to compare the thermal performance of the cylindrical LHTES system in presence of nanoparticles. In addition, the temperature distributions at the center of cylindrical LHTES for the case filled with nano-PCM was compared to the case that pure PCM was used.

Chapter 4: An Experimental and Numerical Investigation On Vertical Cylindrical Thermal Energy Storage System : part I : Use of pure RT-35 as the PCM and part II: Use of the RT-35 enhanced with copper oxide nanoparticles

The primary purpose of this chapter is investigating the effect of using a different PCM on the thermal performance of the cylindrical LHTES system. To do so, a different PCM called Rubitherm 35 (RT-35) with the melting point of 35 $^{\circ}$C was used. The chapter consists of two parts: (i) part I, which the pure RT-35 was used as the storage medium inside the LHTES system and (ii) part (II) , which investigates the effect of using nano enhanced PCM (i.e. copper oxide nanoparticles were dispersed into the pure RT-35. Both numerical and experimental investigations of thermal performance of cylindrical LHTES system are included in this chapter.

Chapter 5: Thermal Energy Storage System with Metal Mesh Porous Medium

The use of porous material for enhancing the thermal performance of a cylindrical LHTES system is studied in this chapter. Metal foams and metal meshes can be displaced into the PCM's container to enhance the thermal conductivity of the PCM. To do so, copper mesh with two different porosities was placed into cylindrical LHTES system filled with n-octadecane as the base PCM. Twelve thermocouples (i.e. eight at the wall of LHTES system and four at the center of LHTES system) were attached to the cylindrical LHTES system to monitor the temperature distribution

inside the PCM. Nusselt number, heat transfer rate, and energy stored have been calculated by using the results obtained from experimental work.

1.1.4. Publications from Present Research Work

The work presented in this thesis is based on submitted or published papers submitted to the respective field of peer-reviewed international journals and conferences.

Chapter 2: **Soroush Ebadi**, Syeda H. Tasnim,Amir A. Aliabadi, Shohel Mahmud, "Melting of Nano-PCM inside a Cylindrical Thermal Energy Storage System: Numerical Study with Experimental Verification, " Energy Conversion and Management (Elsevier), 166 (2018) 241-259.

Chapter 3: **Soroush Ebadi**, Syeda H. Tasnim,Amir A. Aliabadi, Shohel Mahmud, "An Experimental Investigation of the Melting Process of a Bio-based Nano-PCM filled Vertical Cylindrical Thermal Energy Storage System," Applied Thermal Engineering (Elsevier), 2017 ATE_2017_5407, (Under review)

Chapter 4 (part I): **Soroush Ebadi**, Manar Al-Jethelah, Syeda Tasnim, Shohel Mahmud, "An Experimental and Numerical Investigation On Vertical Cylindrical Thermal Energy Storage System : Pure RT-35 as the PCM," Journal of Openphysics (Degruyter), 2017, OPENPHYS-D-17-00113. (Under review).

Chapter 4 (part II): **Soroush Ebadi**, Mohammadhossein Hajiyan, Syeda Tasnim, Amir A. Aliabadi ,Shohel Mahmud, "Effect of Adding Nanoparticles to a Phase Change Material Used in vertical cylindrical Thermal Energy Storage System," Accepted to be published in CSME transactions, 2018.

Chapter 5: **Soroush Ebadi**, Syeda Tasnim, Amir A. Aliabadi ,Shohel Mahmud, "Thermal Energy Storage System with Metal Mesh Porous Medium, (Under preparation, 2018).

Chapter 2

Melting of Nano-PCM (copper oxide nanoparticles dispersed into coconut oil) inside Cylindrical Thermal Energy Storage System: Numerical Study

"A version of this chapter has been published in Energy Conversion and Management journal: Soroush Ebadi, Syeda H. Tasnim, Amir A. Aliabadi, Shohel Mahmud, "Melting of Nano-PCM inside a Cylindrical Thermal Energy Storage System: Numerical Study with Experimental Verification" Energy Conversion and Management (Elsevier), 166 (2018) 241-259.

2.1.Introduction

The ongoing increase in the worldwide population and industrial units is accompanied by a significant demand for energy. On the other hand, the limitation in the sources of conventional fossil fuels and the environmental issues associated with their uses, have caused several concerns and challenges such as security of energy supply and global climate change [1- 4]. To overcome these issues, exploitation of renewable energies (e.g. solar energy, geothermal, wind energy, etc.) has been considered by energy suppliers. However, due to the fluctuations and inability to control the sources of the renewable energies, it is more efficient for these systems to be used with energy storage systems [5]. Thermal Energy Storage (TES) systems are developed with an aim to store thermal energy in an efficient and reliable manner. TES systems have been used in a wide range of applications for heating/cooling purposes including building thermal management, food processing applications, Heating, Ventilation, and Air Conditioning (HVAC) systems, and solar power plants for storing thermal energy during the day and release it during the night and cloudy days. In general, TES systems are divided into three main groups: sensible, latent, and thermo-chemical heat storage. Due to the effective use of Phase Change Materials (PCM) in improving Latent Heat Thermal Energy Storage (LHTES) systems, more impetus has been provided by researchers to develop the LHTES system with PCMs. Utilizing PCMs in LHTES systems have provided advantages of high energy density and an almost constant operating temperature [6]. In these systems, thermal energy is stored during the melting process and released during the solidification process. A wide range of PCMs with various melting temperatures including Paraffin waxes, organic and non-organic compounds, and hydrated salts are available for use in LHTES

systems. A comprehensive information regarding different types of PCMs is available in [7]. To select a proper PCM, different parameters including phase change temperature, stability, amount of latent heat, and thermal conductivity should be considered [8]. Although having desirable attributes for storing thermal energy, PCMs suffer from low thermal conductivity, which results in a lower melting/solidification rate and reduction in the efficiency of LHTES systems [9]. Different approaches for enhancing the thermal conductivity of a PCM have been suggested by researchers, which can be categorized into two main groups. The first group is a geometric approach that is related to a modification in the design of the shape of the enclosure or inserting highly conductive fixed materials such as metal fins and porous materials inside the enclosure [10]. The second approach is based on combining PCM with highly conductive nanoparticles (e.g. copper oxide and aluminum oxide particles) to increase the thermal conductivity of the PCM [11, 12, 13]. Although using the reported methods can enhance the thermal conductivity of a PCM, some challenges are remained. For instance, by adding high volume/weight fraction of nanoparticles to a PCM, sedimentation occurs, which has a negative effect on the thermal conductivity of nano-PCM after several cycles of operation [14]. On the other hand, inserting conductive materials (e.g. metal fin, porous material) into the PCM reduces the volume of filled PCM. Because of the lower amount of PCM, lower amount of stored energy will be achieved [15, 16]. Different types of geometrical configurations including rectangular, spherical, cylindrical, and annular containers have been studied as a TES system. These are necessitated by the different applications and limitations of the occupied space. A complete description of TES systems with different geometries filled with nano-PCMs can be found in [5, 6]. Cylindrical containers can be used both horizontally and vertically, which have invoked a significant interest due to the ease of its manufacturing process. Studying vertical cylindrical containers filled with PCM/nano-PCM, which is the primary focus of the present paper, have been investigated by several researchers. A brief review of studying vertical cylindrical container filled with PCM/nano-PCM is shown in Table.1.

Table 1: Summary of studies on the melting process of PCM/nano-PCM in a vertical cylindrical enclosure

Authors	Type of study	Melting condition	PCM/nano-PCM	Highlighted findings
Sparrow and Broadbent [17]	Experimental and Numerical	Isothermal heating from the sides, insulated from the bottom	Eicosane as the PCM	▪ Fluid motion has a significant effect on the rate of melting and heat transfer. ▪ Experimental results showed a 50% more transfer of energy compared to numerical results. ▪ Initial sub-cooling of PCM significantly decreased the melting rate.
Wenzhen et al. [18]	Analytical	Isothermal heating from the sides and the bottom	Eicosane as the PCM	▪ An insignificant effect of heat conduction is observed on the melting rate in the liquid phase. ▪ Increasing the Stefan number leaded to an increase in the melting rate.
Wu and Lacroix [19]	Numerical	Isothermal heating from the sides, top, and the bottom	Depends on the Prandtl number	▪ The bottom surface had the highest rate of heat transfer. ▪ Conduction was dominated at the top. ▪ For the case heated from the walls, Benard convection occurred earlier than the case heated only from the bottom.
Jones et al. [20]	Experimental and Numerical	Isothermal heating from the sides, constant temperature at the bottom and insulated from the top	Eicosane as the PCM	▪ Four melting regimes including pure conduction, mixed conduction and convection, convection dominant, and shrinking solid occurred during melting process were observed. ▪ Good agreement between numerical and experimental results were observed for Stefan numbers up to 0.1807.
Shmueli et al. [21]	Numerical with comparison with previous experimental work	Isothermal heating from the sides, insulated from the bottom	RT-27 as the PCM	▪ The effect of the mushy zone parameter (C) on the melting process was studied, and it was found that C= 10^8 for this parameter had good agreement with experimental work. ▪ At the beginning of melting process, conduction was the dominant form where with ongoing heating process natural convection dominated. This changed the solid shape to conical shape.
Wu et al. [22]	Numerical	heating from the bottom	Copper nanoparticles in Paraffin as the nano-PCM	▪ Adding nanoparticles to the PCM enhanced the thermal conductivity of the PCM. ▪ Using 1 wt. % of the nano-PCM enhanced melting time up to 13.1%.
Sciacovelli et al. [23]	Numerical	Isothermal heating by using an inner tube at the center of a shell and tube	Copper nanoparticles in Paraffin as the nano-PCM	▪ An improvement in melting rate caused by adding nanoparticles was reported. ▪ A 4% volume fraction of nanoparticles in PCM leads to a 15% decrease in charging time.

Authors	Type of study	Melting condition	PCM/nano-PCM	Highlighted findings
		TES system		
Zeng et al. [10]	Experimental	Heated from the bottom and insulated from the lateral walls	Carbon nanotubes dispersed in 1-dodeconal as the nano-PCM	▪ Melting rate was degraded due to decrease of natural convection in the melting process because of increasing viscosity by adding carbon nanotubes.
Fan et al. [24]	Experimental	Isothermally heated from the bottom	Graphene nanoplatelets dispersed in 1-tetradecanol as the nano-PCM	▪ With a 3 wt. % of nanoparticles at the boundary temperature of 55 °C, there was a 8% improve in melting rate. ▪ Due to the suppression of natural convection by increasing the temperature of boundary condition, the melting rate was degraded.
Alshaer et al. [25]	Experimental	Isoflux heating from the bottom	Multi wall carbon nano tubes placed in RT-65 as the nano-PCM and carbon foam as the porous material	▪ A significant increase in the heat transfer rate was reported by using carbon nanotubes and carbon foam.
Das et al[26]	Numerical	Isothermal heating by using inner tube inside the shell and tube TES system	n-eicosane and carbon allotropes as the nano-PCM	▪ A 15 % and 25 % decrease in the melting time were observed by using 1% volume fraction of single-walled carbon nanotubes (SWCNT) and graphene nanoplatelets (GnP) respectively. ▪ A 1.5 % increase in the melting rate was observed by inclusion of 1% volume fraction of nano-diamond.

There are other recently published works regarding the use of nanoparticles to enhance the thermal performance of a LHTES system. For instance, the volumetric heat generation effect during melting/solidification process of nano-PCM filled horizontal cylindrical geometries were studied by Bechiri and Mansouri [27]. Several researchers also investigated the thermal performance of a shell and tube LHTES system filled with nano-PCM [28-33]. In general, it is reported that dispersing nanoparticles at low volume fractions increases the heat transfer rate and as a result of that the time required for melting/solidification process is decreased. Nonetheless, Parsazadeh and Duan [33] have stated that dispersion of nanoparticles into the PCM increases the melting time due to the degradation of natural convection caused by the addition of Al_2O_3 into the paraffin wax. The recent investigations regarding the use of nano-PCM in a rectangular LHTES system revealed that dispersion of highly conductive nanoparticles into the PCM enhances the thermal conductivity

of the PCM [34-37]. However, it is mentioned that addition of nanoparticles to the PCM enlarges the viscosity of PCM, which lead to a decrease in the natural convection that could lower the thermal performance of the LHTES system [35, 36]. In addition, nano-PCMs have been also used for several thermal management applications [38-41]. In general, it is concluded that dispersion of nanoparticles at low volume/weight fractions can enhance the amount of removed heat, which can enhance the performance of thermal systems.

According to the published works available in the literature, it is identified that the melting process of a nano-PCM filled in a vertical C-TES system, which is isothermally heated from its lateral walls and the top and insulated from the bottom, has not been extensively investigated. In the present paper, a numerical investigation on melting process of a bio-based PCM (coconut oil) enhanced with copper oxide (CuO) nanoparticles is performed. Effect of using different volume fractions (ϕ) of nanoparticles (i.e. ϕ= 0%, 3%, 5%), different heights of filled nano-PCM representing different Rayleigh (Ra) numbers (i.e. Ra_{nl} = 10^6, 10^7, and 10^8) on the melting rate, heat and energy transfer characteristics are studied. Moreover, the behavior of solid-liquid interface at different time intervals is studied as well.

In summary, in the present article, the authors first time studied the melting process of an edible coconut oil PCM with CuO nanoparticles inside a cylindrical enclosure with isothermal surrounding and adiabatic bottom walls. The relatively inexpensive coconut oil PCM is edible, having the melting temperature (≈24^{o}C) close to the typical lab temperature (22 to 23^{o}C), and exhibits excellent stability and very small sedimentation for longer uses once nanoparticles are incorporated compared to many other commercially available PCMs reported in the literature. Properties of the nano-PCM were measured and compared with the modeled equation, a maximum discrepancy of ±5% was observed for the thermal conductivity of nano-PCM. Comprehensive numerical simulation is performed to visualize the progression of the melting process with the experimental comparison; calculate the melt fraction, Nusselt number, and energy storage rate.

2.2.Modeling and Analysis

A schematic diagram of the vertical C-TES system is presented in Fig. 1.

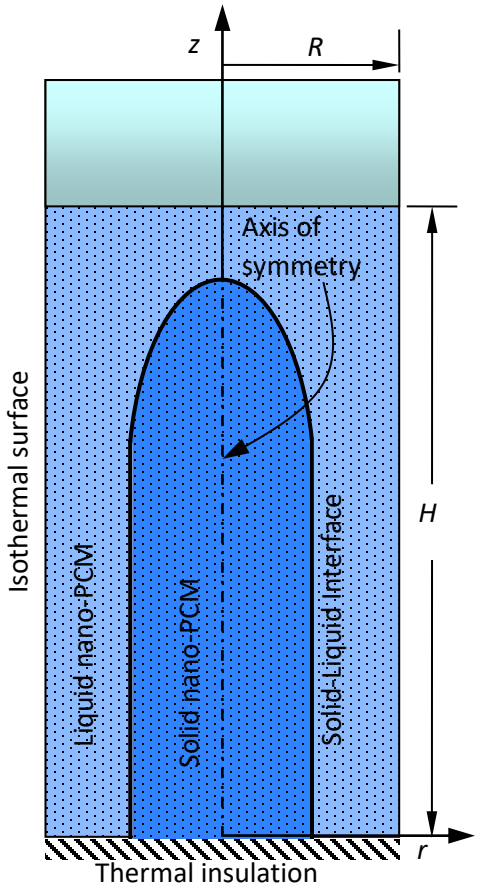

Fig. 1. Schematic diagram of the problem under consideration with dimensions

A numerical investigation of the melting process of a bio-based PCM (melting temperature T_m) enhanced with different volume fractions of nanoparticles (i.e. 0%, 3%, and 5% of copper oxide nanoparticles) inside the C-TES system is performed in this work based on the enthalpy-porosity technique. The vertical C-TES system is assumed to have inner diameter (d=2R) of 4.44 cm and is filled with a nano-PCM at different heights (H). The C-TES system is isothermally heated from its lateral walls and the top, and insulated from the bottom. The initial temperature (T_0) of the system is assumed to be 23°C, while the lateral wall temperature (T_h) is 34°C. It is worth mentioning that the physical expansion of the PCM during the phase change process was not considered in this work. For the temperature range considered in this paper, the volume expansion of the coconut oil was observed to be small (i.e. approximately 3% for a 20°C temperature difference) in our experimental work as opposed to many other commercially available PCMs (e.g., Rubitherm, n-octadecane, etc.) reported in the literature. For example, our experiments showed that Rubitherm

22 (RT-22) PCM shows almost 10 to 12% expansion during melting which has melting temperature (~22^{o}C), close to the melting temperature of coconut oil (~24^{o}C).

2.2.1. Properties of PCM and nanoparticles

The properties of the copper oxide nanoparticles [24, 25] and the coconut oil used as the PCM are presented in Table 2.

Table 2: Thermophysical properties of copper oxide nanoparticles [42, 43] and coconut oil

Thermo-physical properties	Coconut oil		Copper Oxide nanoparticle
	Liquid	Solid	
β (1/K)- Coefficient of Thermal Expansion	7×10^{-4}	___	85×10^{-7}
h (kJ/kg)- Latent heat of fusion	103		___
k (W/m K)- Thermal conductivity	0.166	0.228	18
μ (Pa.s)- Viscosity	0.0268	___	___
c_p (kJ/kg K)- Specific heat	1.67	3.75	0.54
ρ (kg/m^3)- Density	918	920	6500
T_m ($^{\circ}$C) - Melting Temperature	24		-

The food grade PCM used in the work (i.e., coconut oil) is obtained from a local supplier. For the comparison purpose, the price of the obtained coconut oil and some widely used paraffin based and organic PCMs are as follows: (i) coconut oil: ~$8.0/kg (from DESI), (ii) n-octadecane: ~$144/kg (from VWR), (iii) Lauric Acid: ~$89.0/kg (from VWR), and (iv) RT-25: ~ €13.97/kg (from Rubitherm). However, the local supplier could not provide any information on thermophysical properties other than the melting temperature information only. Therefore, the thermophysical properties of PCM (i.e., coconut oil) and nano-PCM (CuO nanoparticles dispersed in coconut oil PCM) were directly measured in our facilities at the University (Advanced Energy Conversion and Control Lab, Bio-Innovation Research Lab, and Food Research Lab). Properties are measured for a temperature range from 10 to 40 ^{o}C and for the volume fractions of nanoparticles from 0 to 3.5%. Thermal conductivity measurements for PCM and nano-PCM were performed using KD2 Pro handheld device and TPS-500 system. The measured conductivities were identified within the ±5% error limit with the modeled equations presented in Eq. (8) and Eq. (9). Dynamic

viscosity measurements for PCM and nano-PCM were performed using a Rotational Viscometer and a Vibration Viscometer. The measured viscosities were identified within the ±2.5% error limit with the modeled equation presented in Eq. (7). Density measurements for PCM and nano-PCM were performed using a DMA 35 Density meter. The measured densities were identified within the ±1.0% error limit with the modeled equation presented in Eq. (5) and Eq. (6). Specific heat and heat of fusion measurements for PCM and nano-PCM were performed using a Differential Scanning Calorimeter (DSC). The measured densities were identified within the ±1.0% error limit with the modeled equation presented in Eq. (12) and Eq. (13).

2.2.2. Approximations and Modeled Equations

In the current numerical model, the molten or the liquid form of nano-PCM is assumed to be a Newtonian incompressible fluid, and laminar flow is considered for liquid phase bio-based nano-PCM. The density term in the liquid phase of nano-PCM varies linearly with the variation in the temperature, the Boussinesq approximation is adopted in this model. In addition, it is assumed that between the PCM and nanoparticles, the local thermal equilibrium exists. To simplify the problem, a 2-D axisymmetric model is developed. As the melting process starts, thermal energy will flow from the lateral sides of the enclosure to the bio-based nano-PCM. As time advances, the liquid-solid interface can be seen. The principal differential equations, which govern the melting process, are listed below [44]:

Mass conservation equation: $\frac{\partial u}{\partial r}+\frac{u}{r}+\frac{\partial w}{\partial z}=0$ (1)

where *u* and *w* are the components of velocity in the radial and axial directions, respectively.

Energy conservation equation: $\frac{\partial T}{\partial t}+u\frac{\partial T}{\partial r}+w\frac{\partial T}{\partial z}=\frac{k}{\rho C_p}\left[\frac{1}{r}\frac{\partial}{\partial r}\left(r\frac{\partial T}{\partial r}\right)+\frac{\partial^2 T}{\partial z^2}\right]$ (2)

where *T*, *t, k, ρ,* and C_p represent temperature, time, thermal conductivity, density, and specific heat at constant pressure, respectively.

Momentum conservation equation (radial direction): (3)

$$\rho\left(\frac{\partial u}{\partial t}+u\frac{\partial u}{\partial r}+w\frac{\partial u}{\partial z}\right)=-\frac{\partial p}{\partial r}+\mu\left(\frac{\partial^2 u}{\partial r^2}+\frac{1}{r}\frac{\partial u}{\partial r}-\frac{u}{r^2}+\frac{\partial^2 u}{\partial z^2}\right)+A_m\frac{(1-f)^2}{f^3+\varepsilon}u$$

Momentum conservation equation (axial direction):

$$\frac{\partial w}{\partial t}+u\frac{\partial w}{\partial r}+w\frac{\partial w}{\partial z}=-\frac{1}{\rho}\frac{\partial p}{\partial z}+\frac{\mu}{\rho}\left(\frac{\partial^2 w}{\partial r^2}+\frac{1}{r}\frac{\partial w}{\partial r}+\frac{\partial^2 w}{\partial z^2}\right)+g\beta(T-T_m)+A_m\frac{(1-f)^2}{f^3+\varepsilon}w \quad (4)$$

where μ, g, β, and T_m represent viscosity, gravitational acceleration, coefficient of thermal expansion, and the melting temperature, respectively. The last terms on the right hand side of the momentum equations (i.e., Eq. (3) and Eq. (4)) represent momentum sink, which is described further in Section 2.4.

2.2.3. Thermophysical Property Relationships

The differences in the amount of the nanoparticles will affect the thermophysical properties of the nano-PCM in different extents. There are several models reported and extensively utilized in the current literature for modeling and calculating thermophysical properties (i.e., conductivity, viscosity, etc.) of nano-fluids and nano-PCMs. The thermophysical property relationships as given in Eq. (5) to Eq. (13) below [45-48] are approximately suitable for the nano-PCM used in this paper, where, subscripts '*nl*', '*ns*', '*n*' , '*l*' , '*s*' refer to properties of liquid nano-PCM, solid nano-PCM, nanoparticles, liquid PCM, and solid PCM, respectively.

Density of nano-PCM, liquid phase: $$\rho_{nl}=(1-\phi)\rho_l+\phi\,\rho_n \quad (5)$$

Density of nano-PCM, solid phase: $$\rho_{ns}=(1-\phi)\rho_s+\phi\,\rho_n \quad (6)$$

Dynamic viscosity of nano-PCM, liquid phase: $$\mu_{nl}=\frac{\mu_l}{(1-\phi)^{2.5}} \quad (7)$$

Thermal conductivity of nano-PCM, liquid phase: $$k_{nl}=\frac{k_n+2k_l-2\phi(k_l-k_n)}{k_n+2k_l+\phi(k_l-k_n)}k_l \quad (8)$$

Thermal conductivity of nano-PCM, solid phase: $$k_{ns}=\frac{k_n+2k_s-2\phi(k_s-k_n)}{k_n+2k_s+\phi(k_s-k_n)}k_s \quad (9)$$

Expansion coefficient of nano-PCM, liquid phase: $$(\rho\,\beta)_{nl}=(1-\phi)\,(\rho\,\beta)_l+\phi\,(\rho\,\beta)_n \quad (10)$$

Expansion coefficient of nano-PCM, solid phase: $$(\rho\,\beta)_{ns}=(1-\phi)\,(\rho\,\beta)_s+\phi\,(\rho\,\beta)_n \quad (11)$$

Heat capacity of nano-PCM, liquid phase: $$(\rho\,C_p)_{nl}=(1-\phi)\,(\rho\,C_p)_l+\phi\,(\rho\,C_p)_n \quad (12)$$

Heat capacity of nano-PCM, solid phase: $$(\rho\,C_p)_{ns}=(1-\phi)\,(\rho\,C_p)_s+\phi\,(\rho\,C_p)_n \quad (13)$$

As mentioned earlier, thermophysical properties are measured for different values of ϕ (up to 3.5%) and compared to the values obtained from the Eq. (5), Eq. (7), Eq. (8), and Eq. (12), respectively. It is identified that the discrepancies between using the equations and the measured values are within the ±1% error limit for the density and the specific heat, within the ±2.5% error limit for the viscosity, and within the ±5% error limit for the thermal conductivity. Therefore, during the numerical simulations, thermophysical property relationships (i.e., Eq. (5) to Eq. (13)) are used. Additionally, several samples of nano-PCM with different volume fractions were stored in the lab for approximately 30 weeks and periodically tested them by melting and solidifying in a controlled temperature environment. A small amount of sedimentation is observed for the larger ϕ (over 2%).

2.2.4. Mushy Zone (or Transition Zone) Approximation

It should be noted that the change in phase (i.e., solid to liquid) of the nano-PCM occurs gradually within a transition stage. At this stage, the properties of nano-PCM are influenced by a transition temperature interval (i.e., ΔT_m) which is observed to be approximately 1°C for the PCM considered in the work. Table 3 presents the variation in the thermophysical properties of nano-PCM (i.e., density, heat capacity, viscosity, and thermal conductivity) within different temperature ranges with respect to T_m and ΔT_m.

Table 3: Properties of the nano-PCM at the transition stage [47-50]

	Range of Temperatures		
Properties	$T < T_m$	$T_m \le T \le T_m + \Delta T_m$	$T > T_m + \Delta T_m$
k	k_{ns}	$\frac{k_{ns} + k_{nl}}{2}$	k_{nl}
ρ	ρ_{ns}	$\frac{\rho_{ns} + \rho_{nl}}{2}$	ρ_{nl}
(ρC_p)	$(\rho C_p)_{ns}$	$\frac{(\rho C_p)_{ns} + (\rho C_p)_{nl}}{2} + \frac{\rho_{ns} + \rho_{nl}}{2}\left(\frac{h_{sl,n}}{\Delta T_m}\right)$	$(\rho C_p)_{nl}$
μ	10^6	——	$\frac{\mu_l}{(1-\phi)^{2.5}}$

where $h_{sl,n}$ is the latent heat of fusion of nano-PCM and can be calculated by the following equation:

$$h_{sl,n} = (1-\phi)\, h_{sl} \tag{14}$$

At the transition stage, the value of specific heat increases into a higher value compared to the solid and the liquid phase. The increment in the specific heat is caused by the high absorbance of heat in form of latent heat within small temperature range. In addition, in the transition stage, the viscosity drops from a high value in the solid phase to low value in the liquid phase. In order to handle these changes, mushy zone parameters [51, 52] are used. As it is indicated in Eq. (3) and Eq. (4), mushy zone is approximated using an additional source term (i.e., momentum sink) in the governing momentum equations. In the momentum sink terms, $A_m \frac{(1-f)^2}{f^3+\varepsilon} u$ and $A_m \frac{(1-f)^2}{f^3+\varepsilon} w$, A_m is the mushy zone parameter (=10^5), f is the melting region identifier, and ε (=10^{-8}) is a small number to avoid division by zero. The identifier f =0 in the solid region (i.e., $T < T_m$), f =1 in the liquid region (i.e., $T > T_m + \Delta T_m$), and 0< f <1 (i.e., $T_m \le T \le T_m + \Delta T_m$) [52].

2.2.5. Boundary and initial conditions

The following initial and boundary conditions have been considered:

$$\begin{aligned}
&\text{Initial condition } (t=0): && T(r,z,0) = T_0,\ u = w = 0,\\
&\text{Bottom part of the C-TES system } (t>0): && \frac{\partial T(r,0,t)}{\partial z} = 0, u = w = 0,\\
&\text{Lateral wall of the C-TES system } (t>0): && T(R,z,t) = T_h, u = w = 0,\\
&\text{Upper part of the C-TES system } (t>0): && T(r,H,t) = T_h, u = w = 0.
\end{aligned} \tag{15}$$

2.2.6. Energy Storage Rate

The amount of the stored energy during the melting process can be defined by calculating the energy transferred from hot lateral walls to the cold nano-PCM during the melting process. The transferred energy can be defined as the time integration of the instantaneous heat transfer rate during melting process, which is presented in equations below [53].

$$E = \int_0^t \dot{Q}(t)\, dt \tag{16}$$

where $\dot{Q}(t)$ is the instantaneous heat transferred during melting process defined as:

$$\dot{Q}(t) = (\pi \mathrm{d}) \int_0^H \left(-k \frac{\partial T}{\partial r}\right) dz + (2\pi) \int_0^R \left(-k \frac{\partial T}{\partial z}\right) r\, dr \tag{17}$$

where d ($=2R$) is the inner diameter of the C-TES system and k represents the thermal conductivity of the of the nano-PCM. Further, the heat transfer from the hot lateral wall to the cold nano-PCM can be evaluated by the average Nusselt number, which may be calculated based on either thermal conductivity of PCM, k_f, or thermal conductivity of the nano-PCM, k_{nf}. The following equations can be used for calculating the average Nusselt number:

$$\text{Nusselt number based on } k_{nf}: \; Nu_n = \frac{hH}{k_{nf}} = -\frac{1}{T_h - T_m} \int_0^H \left(\frac{\partial T}{\partial r}\right)_{r=R} dz \tag{18a}$$

$$\text{Nusselt number based on } k_f: Nu_f = \frac{hH}{k_f} = -\frac{1}{T_h - T_m} \left(\frac{k_{nf}}{k_f}\right) \int_0^H \left(\frac{\partial T}{\partial r}\right)_{r=R} dz \tag{18b}$$

where h represents the surface averaged convection heat transfer coefficient. Note however that the magnitudes of Nu_n and Nu_f may be different for a given condition, the value of h will remain same irrespective of these definitions.

2.2.7. Solution Technique, Grid and Time Interval Dependency Tests, and Validation

Equations (1) to (4) are numerically solved along with the initial and boundary conditions using the finite-element based COMSOL Multiphysics® software. Three different mesh sizes including 3471, 8071, and 19209 elements are used to examine the mesh dependency. The melting fraction (*MF*) for Ra_{nl} =10^6 and ϕ = 3% is numerically calculated by using three different described meshes above and the corresponding result is presented in Fig. 2(a) and Table 4. The percentage of melting fraction (*MF*) is calculated using the following equation:

$$MF = \frac{\text{Volume of the liquid nano-PCM}}{\text{Total (solid+ liquid) volume of the nano-PCM}} \times 100\%. \tag{19}$$

As it can be seen from Fig. 2(a) and Table 4, a slight difference among the melting fractions are observed towards the end of the melting process.

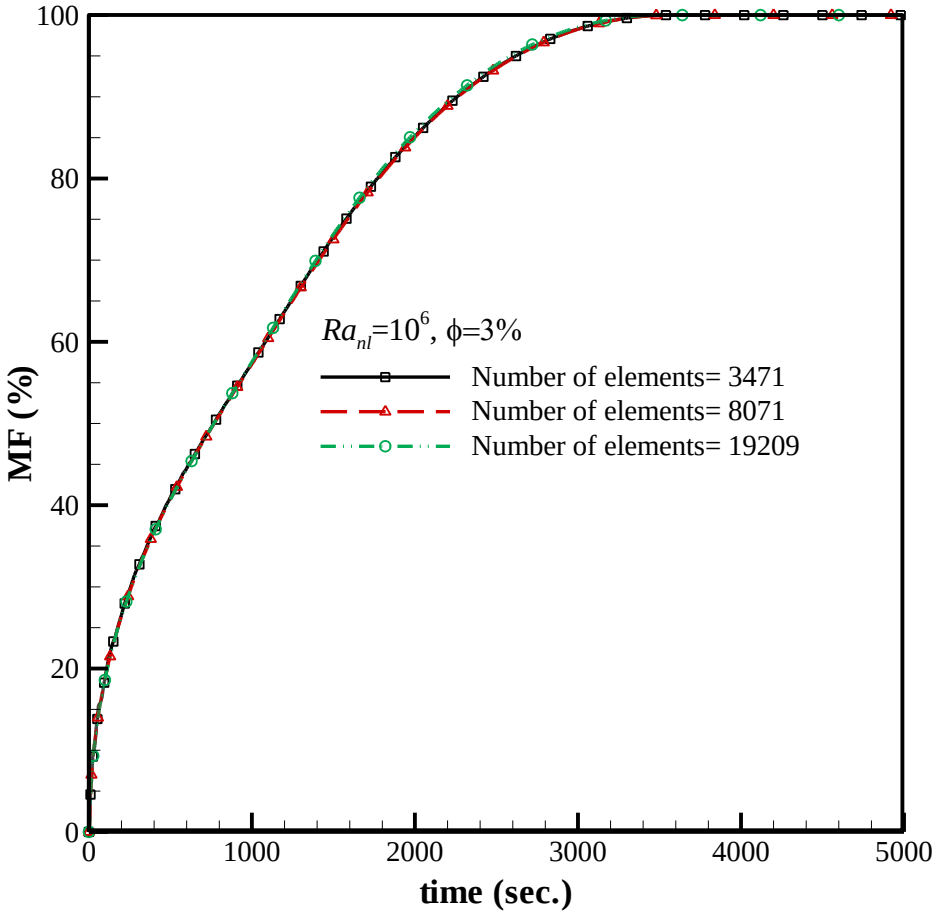

Fig. 2(a). Melting fraction for three different mesh qualities (Ra_{nl} = 10^6, ϕ = 3%).

Table 4: Melting fraction values for there different mesh qualities at three selected times, Ra_{nl} = 10^6, and ϕ = 3%.

No. of elements	MF at 1000 s	MF at 2000 s	MF at 3000 s
3471	57.29%	85.04%	98.26%
8255	57.38%	85.17%	98.30%
19209	57.54%	85.66%	98.52%

Therefore, to ensure the accuracy of the results and reduce the simulation time, the mesh size with 8071 is adopted for further calculations. A magnified view of the considered mesh is presented in Fig. 2(b). As it can be seen, a non-uniform distribution of mesh with higher concentration of

elements near the rigid walls of the C-TES system is considered. In addition, the detailed information regarding the elements used in this mesh is shown in Table. 5.

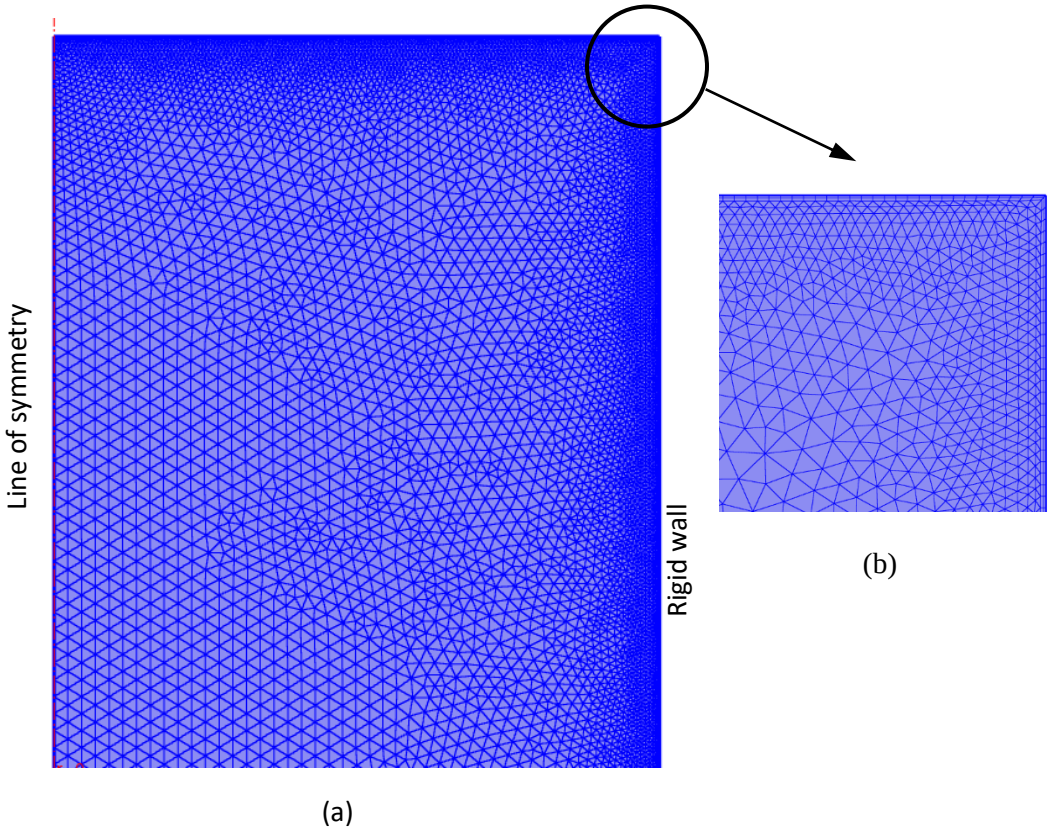

Figure 2(b): (a) A magnified view of the mesh distribution inside the C-TES system and (b) a magnified view of the mesh distribution at the upper left corner of the geometry.

Table 5: Details of the mesh elements for $Ra_{nl} = 10^6$

Name of the elements	Number of elements
Triangular	7348
Quadrilateral	556
Edge	342
Vertex	9

In the next step, the time dependency test is examined. To do so, the melting fraction for the similar case as the above are numerically calculated using three different time intervals as shown in Table 6. The results of this test are shown in Figure 2(c) and Table 7.

Table 6: Time intervals used to examine the time dependency

Starting time (s)	Ending time (s)	Time step (s)		
		Present simulation	Test 1	Test 2
0	10	0.01	0.1	0.005
10	100	0.1	1	0.05
100	10000	10	100	5

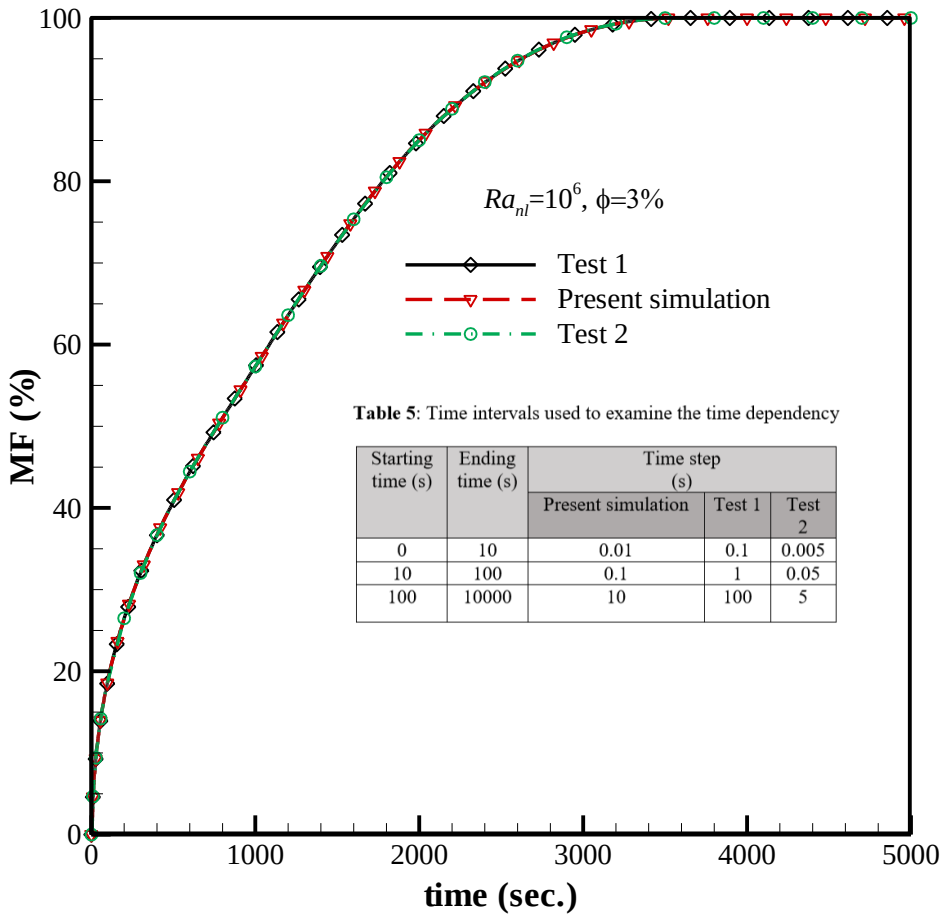

Fig. 2(c). Melting fraction calculated with three different time intervals different time intervals (Ra_{nl} = 10^6, ϕ = 3%).

Table 7: Melting fraction values for three different time intervals ($Ra_{nl} = 10^6$, $\phi = 3\%$)

Model	MF at 1000 s	MF at 2000 s	MF at 3000 s
Present simulation	57.29%	85.04%	98.26%
Test 1	57.31%	85.04%	98.3%
Test 2	57.32%	85.03%	98.26%

As it can be observed from Table 7 and Fig. 2(c), the melting fraction values at three different selected values are almost identical for the mentioned time intervals. As a result, the time independency of the numerical model is concluded. To validate the accuracy of the current numerical model, simulations are carried out to reproduce some results from Shmueli et al. [21]. Shmueli et al. [21] performed a numerical investigation to study the melting process of RT-27 filled in vertical cylindrical tubes. Shmueli et al. [21] considered two different cylindrical tubes with the diameters of 3 cm and 4 cm and height of 17 cm. These cylinders were insulated at the bottom and heated isothermally from their sides. The initial temperature of the RT-27 was set to 22°C and was heated 10°C and 30°C above the melting temperature of RT-27. To check the accuracy of the present work, similar conditions as described in Shmueli's [21] work were set. The thermophysical properties of RT-27 are shown in Table. 8.

Table 8: Thermophysical properties of RT-27 [54]

Thermo-physical properties	Rubitherm, RT-27	
	Liquid	Solid
β (1/K)- Coefficient of Thermal Expansion	0.0005	___
h (kJ/kg)- Latent heat of fusion	179	
k (W/m K)- Thermal conductivity	0.15	0.24
ν (m^2/s) – Kinematics Viscosity	3.42×10^{-3}	___
c_p (J/kg K)- Specific heat	1800	2400
ρ (kg/m^3)- Density	760	870
T_m (°C) - Melting Temperature	28-30	

A comparison is presented in Fig. 3(a) where numerically obtained images representing different melting stages are compared for four selected times (i.e., 8 min., 20 min., 32 min., and 36 min.). In each image, the solid PCM, liquid PCM, and solid-liquid interface are clearly visible.

Additionally, experimentally obtained images, reported in Shmueli et al. [21] are added in Fig. 3(a) and comparisons are explained below.

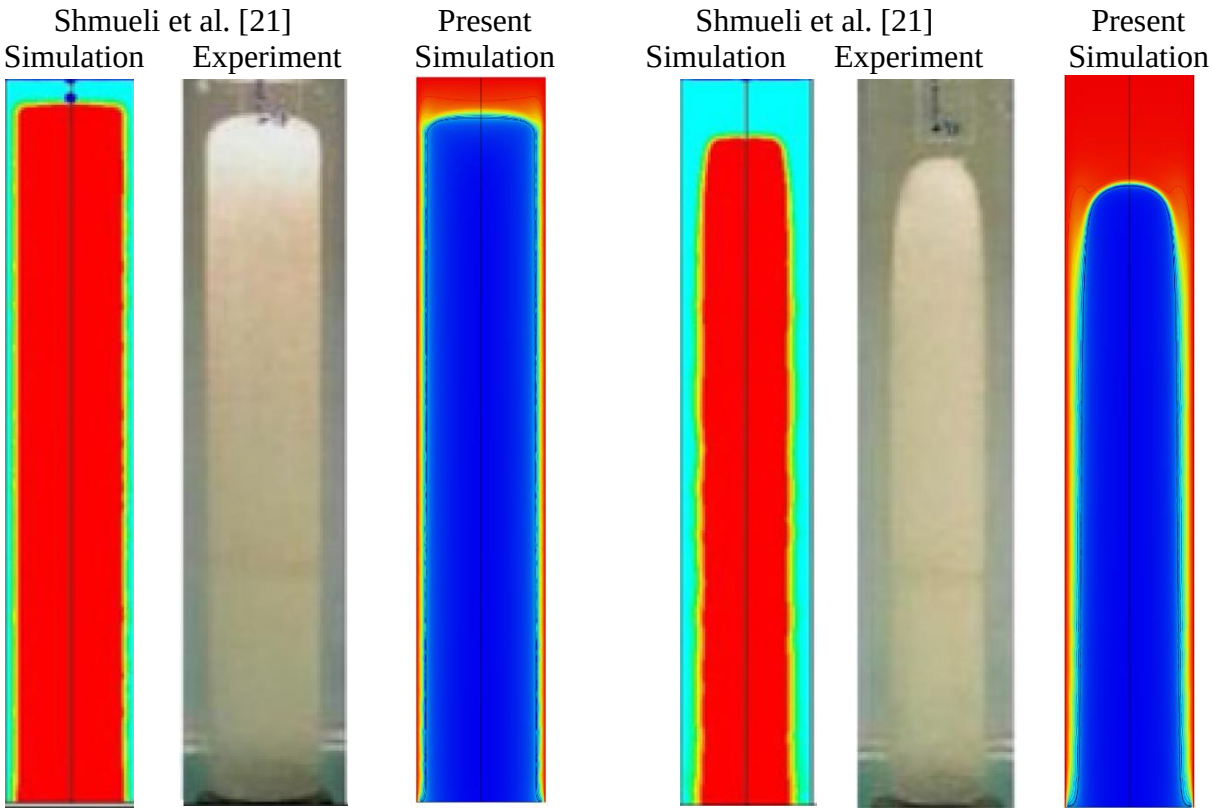

(i) 8 minutes (ii) 20 minutes

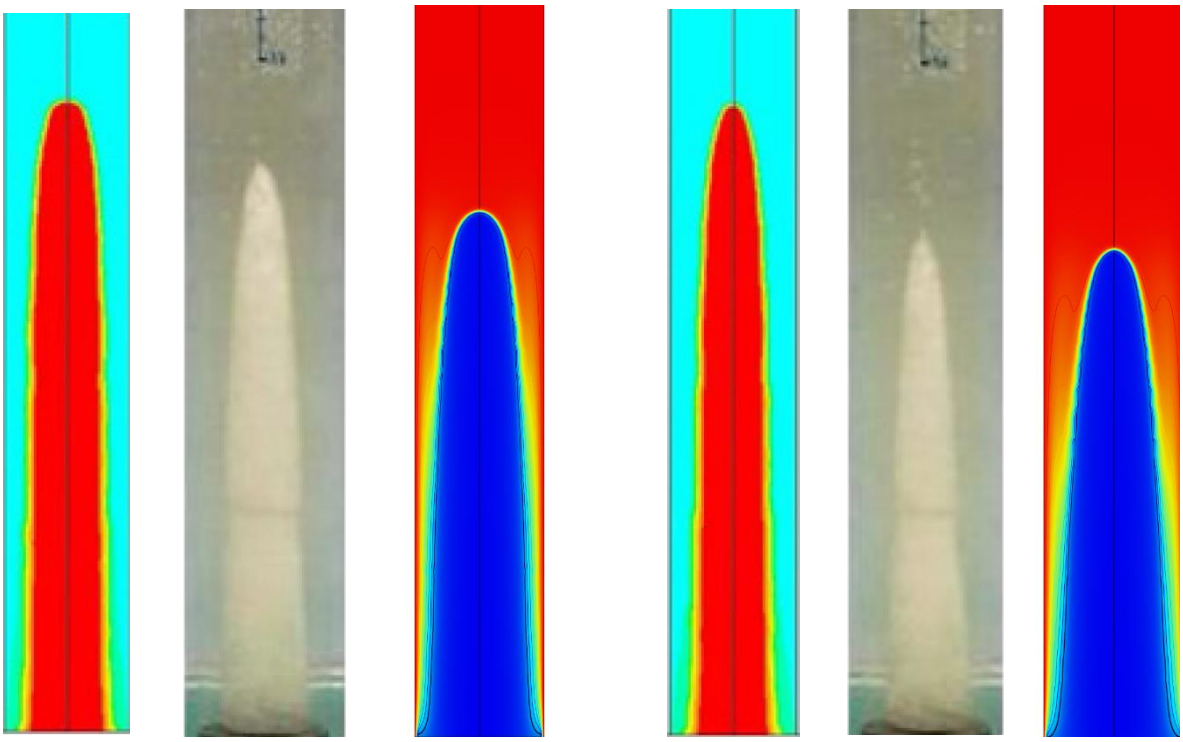

(iii) 32 minutes (iv) 36 minutes

Fig. 3(a). Validation of the numerical model with previously published work in the literature [21].

(i) Images at 8 min. (Fig. 3a(i)): Images from present and Shmueli et al.'s [21] numerical works are almost identical with a thin layer of liquid PCM close to the vertical wall. The thickness of the liquid layer in the experimental work seems slightly larger than both numerical works. The top part of the solid PCM is slightly curved for both numerical works, which is similar to the experimental image.

(ii) Images at 20 min. (Fig. 3a(ii)): Portion of the upper part of the enclosure occupied by the liquid PCM is bigger in size in the present numerical image than the Shmueli et al.'s [21] numerical image. However, the experimental image shows a size that lies in between two numerical works. The curvature of the top solid PCM from present simulation work is similar to that of Shmueli et al.'s [21] experimental work.

(iii) Images at 32 min. (Fig. 3a(iii)): Portion of the upper part of the enclosure occupied by the liquid PCM is bigger in size in the present numerical image than the Shmueli et al.'s [21] numerical image. However, the vertical liquid layer in Shmueli et al.'s [21] work is relatively thicker in size than the present numerical work. Shmueli et al.'s [21] experimental image shows a size that lies in between two numerical works. The curvature of the top solid PCM for all cases shows an inverted dome pattern.

(iv) Images at 36 min. (Fig. 3a(iv)): Most discrepancy between present numerical and Shmueli et al.'s [21] numerical works is observed here. However, the height of the solid PCM for present numerical work is close to the Shmueli et al.'s [21] experimental work.

In summary, it can be argued that a fair agreement is obtained between the present work and numerical/experimental works reported by Shmueli et al. [21]. Additional comparisons are reported in section 2.3.4. In addition to the qualitative comparison presented above, a quantitative comparison is presented in Fig. 3(b) where results obtained from current simulation using the case of Shmueli et al.'s [21] are compared with the experimental and numerical work reported in [21].

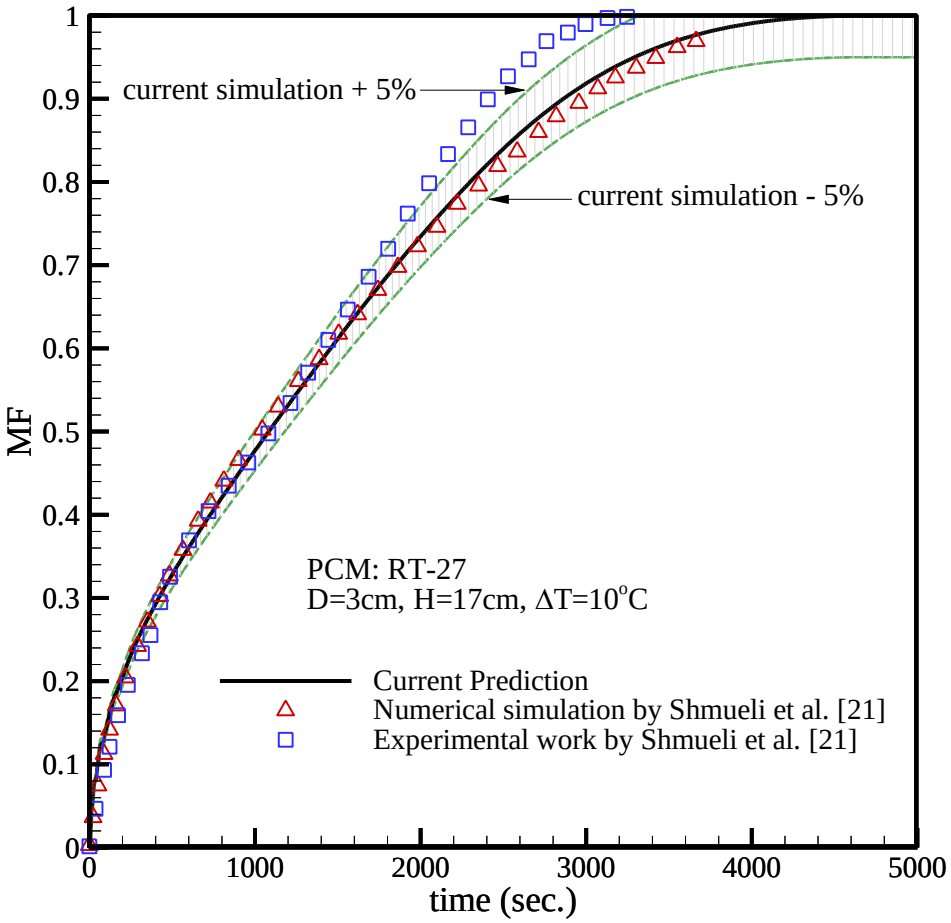

Fig. 3(b). Validation of the simulated result with result obtained in Shmueli et al. [21]

As it can be observed, the current simulation has a very good agreement with Shmueli et al.'s [21] numerical work. However, their experimental work shows more discrepancy beyond 2000 s. It can be further observed from Fig. 3(b) that the difference between the experimentally and numerically

obtained melt fractions obtained from Shmueli et al. [21] is beyond 5% error limit after 2000s (MF>78%). Therefore, our validation decision is based on the agreement between numerically obtained melt fraction values from current simulation and numerically obtained melt fraction values reported in Shmueli et al. [21].

2.3 Results and Discussion

Results obtained from numerical simulations are presented and discussed in this section. Results include images during the melting process, percentage of melting fraction, Nusselt number, and rate of energy storage. These parameters are presented for different values of nanoparticles volume fraction and Rayleigh number. Rayleigh number can be defined either based on the liquid nano-PCM properties (Ra_{nl}) or liquid base-PCM properties (Ra_l) as shown in Eq. 20(a) and Eq. 20(b) below:

Rayleigh number based on liquid nano-PCM properties: $$Ra_{nl} = \frac{g\ \beta_{nl}\ H^3(T_h - T_m)}{\nu_{nl}\alpha_{nl}} \qquad (20a)$$

Rayleigh number based on liquid base-PCM properties: $$Ra_l = \frac{g\ \beta_l\ H^3(T_h - T_m)}{\nu_l\alpha_l} \qquad (20b)$$

It should be noted that the magnitude of Ra_{nl} changes with changing ϕ as thermophysical properties of liquid nano-PCM (i.e., μ_{nl}, α_{nl}, β_{nl}, etc.) depend strictly on ϕ. Therefore, to keep Ra_{nl} constant with changing ϕ the magnitude of H should be adjusted for a given reference temperature difference (i.e, $T_h - T_m$). However, Ra_l does not change with any changes in ϕ as the thermophysical properties of base-PCM (i.e., μ_l, α_l, β_l, etc.) are independent of ϕ. Both Ra_{nl} and Ra_l are extensively used in the literature related to nanofluids and nano-PCMs. In this paper, Ra_{nl} is used to include the effect of adding nanoparticles with different ϕ. Ra_{nl} gives some advantages over Ra_l while establishing correlation with other dimensionless parameters, such as, Nusselt number.

2.3.1. Evolution of solid-liquid interface and trend of melting fraction

Figure 4 shows the evolution of solid-liquid interface of nano-PCM inside the C-TES system at $Ra_{nl} = 10^6$ for three selected volume fractions of nanoparticles (i.e. ϕ=0%, 3%, and 5%).

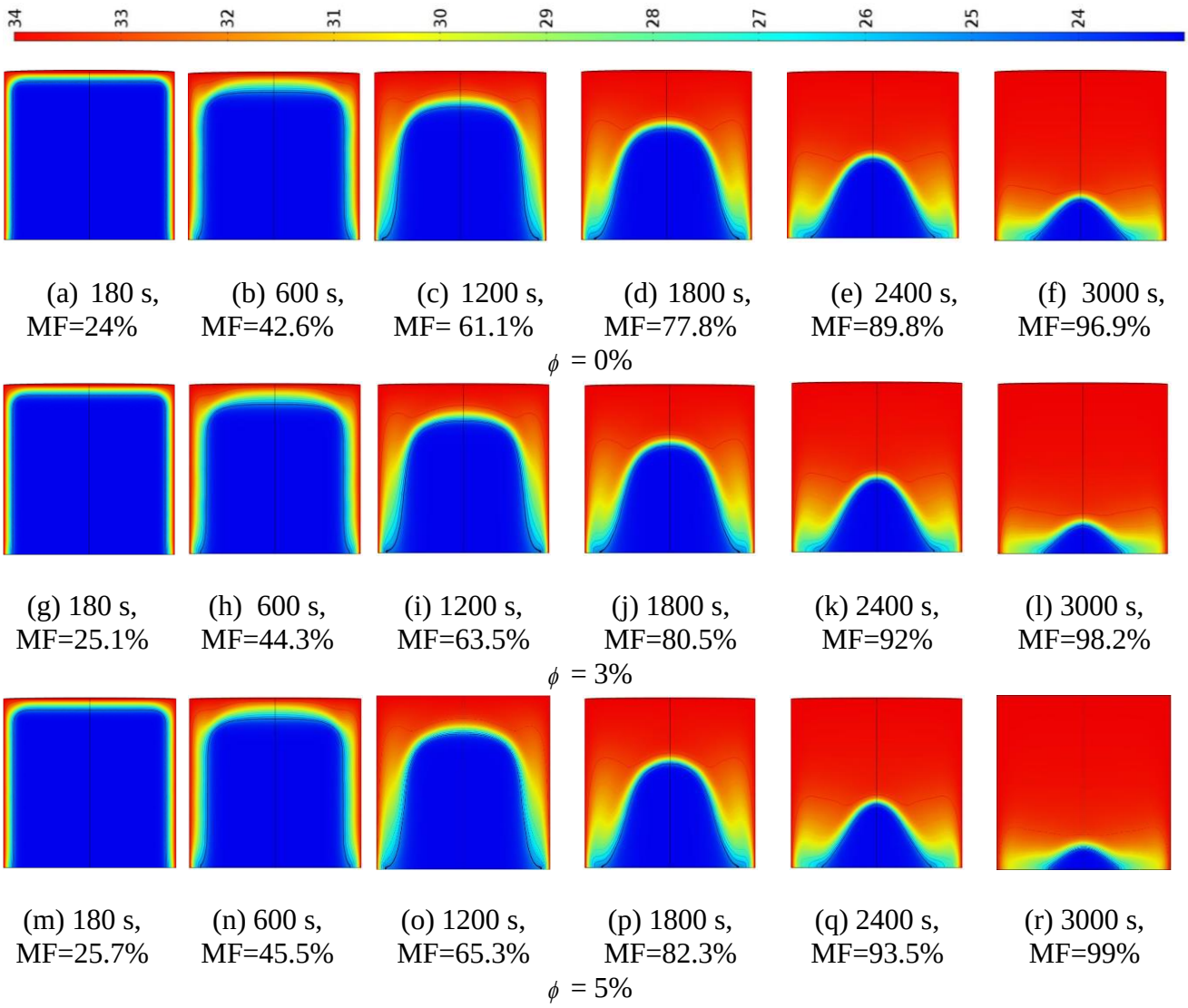

Fig. 4. Effect of different volume fractions of nanoparticle on the melting progression at different time for $Ra_{nl}=10^6$.

For each ϕ, numerically obtained thermal images are presented at six selected times to cover a range of characteristic melting regimes. Corresponding values of melting fractions are presented in the individual figure title as well. Note that the height of the enclosure has to be adjusted slightly

to keep $Ra_{nl}=10^6$ at ϕ=3% (5.1% increase in height compared to ϕ=0% case) and 5% (8.7% increase in height compared to ϕ=0% case). Each row in Fig. 4 implies the effect of melting time, while each column implies the effect of ϕ. At the beginning of the melting process, the entire nano-PCM is in the solid form at the initial temperature (T_0). Just after initiation of the higher wall temperature (T_h), the solid nano-PCM adjacent to heated walls of the C-TES system absorbs the thermal energy from the walls, which increases the solid nano-PCM's temperature sensibly, until it reaches the melting temperature (T_m). At this stage (e.g., see Fig. 4(a)) vertical thin layers of liquid nano-PCM adjacent to lateral walls and at the top are appeared which lead to having a solid-liquid interface. Conduction is the dominant heat transfer mode at early stages of melting process, as the narrowness of the liquid nano-PCM layers allow the dominance of the viscous force over the buoyancy or inertial forces, resulting in a motionless (or nearly motionless) liquid nano-PCM. These layers will grow as heating continues. With ongoing heating, buoyancy or inertial forces overcome the viscous force, which will initiate the upward motion of warm liquid nano-PCM. This motion is pronounced initially at the top corners of the enclosure. Specifically, a relatively wider region of liquid nano-PCM is observed at the upper edges of the enclosure which grows as time advances further. However, at the lower part of the vertical liquid layers of the nano-PCM, conduction is still the dominant mode of heat transfer (see Fig. 4(b)). This combined natural convection and conduction dominated melting zone can be termed as the mixed or transition regime of melting. At later times, natural convection becomes more dominant, thus widening up more space filled with liquid nano-PCM. Thermal stratification and convective motion simultaneously assist accumulation of more thermal energy at the upper part, resulting in a curved interface at the top. As time advances further, intensified convection motion melts down remaining solid nano-PCM gradually. At some stage, conduction dominated melting is completely diminished and this can be attributed from the change in the shape of the remaining solid nano-PCM from a nearly flat pattern to a dome shape pattern (see Fig. 4(c) to Fig. 4(f))). Adding nanoparticle does not show a significant improvement on the melting rate at the early stage of the melting process where conduction heat transfer dominates. Although adding nanoparticles improved the thermal conductivity of the nano-PCM and reduce slightly the thermal resistant in the liquid layers, due to the motionless molten nano-PCM, there is not a significant improvement in the melting rate at these stages. Note however that the size of the enclosure is slightly bigger for

ϕ=3% and ϕ=5%. However, as it can be seen from Fig. 4(f), Fig. 4(l), and Fig. 4(r), adding nanoparticles improved the melting rate at the later stages of the melting process. At these stages, natural convection is the dominant form of heat transfer. By adding nanoparticles with different ϕ, the dominance of natural convection occurs earlier, which results in higher melting fraction rates. Therefore, increasing the ϕ from 3% to 5% showed more improvement on the melting rate.

Figures 5(a) and 5(b) show the effect of Ra_{nl} on the progression of melting process at ϕ = 3%. Note that 115.45% and 364.16% increases in the *H* are required to achieve $Ra_{nl}=10^7$ and $Ra_{nl}=10^8$, respectively, from $Ra_{nl}=10^6$. In Fig. 5(a) thermal images are selected in a way to match the percentage melting fractions closely at all three Ra_{nl}s. The corresponding times of melting are presented in the figure as well. An increase in Ra_{nl} implies an increase in the height of the nano-PCM, which results in larger time of melting to achieve same level of melting fractions at higher Ra_{nl}. An increase in Ra_{nl} further implies stronger buoyancy force and this can be attributed to the shape of the remaining solid nano-PCM at higher Ra_{nl}. For the case of Ra_{nl} = 10^6, the shape resembles a dome, while at Ra_{nl} =10^8, it is like a slender inverted parabola. The distance between domination of the natural convection regime close to the top of the enclosure and the remaining solid nano-PCM increases as well at higher Ra_{nl} (see images Fig. 5a(j)and Fig 5a(p)). Similar behaviour is shown in Fig. 5(b) where melting progression at the same time intervals is presented.

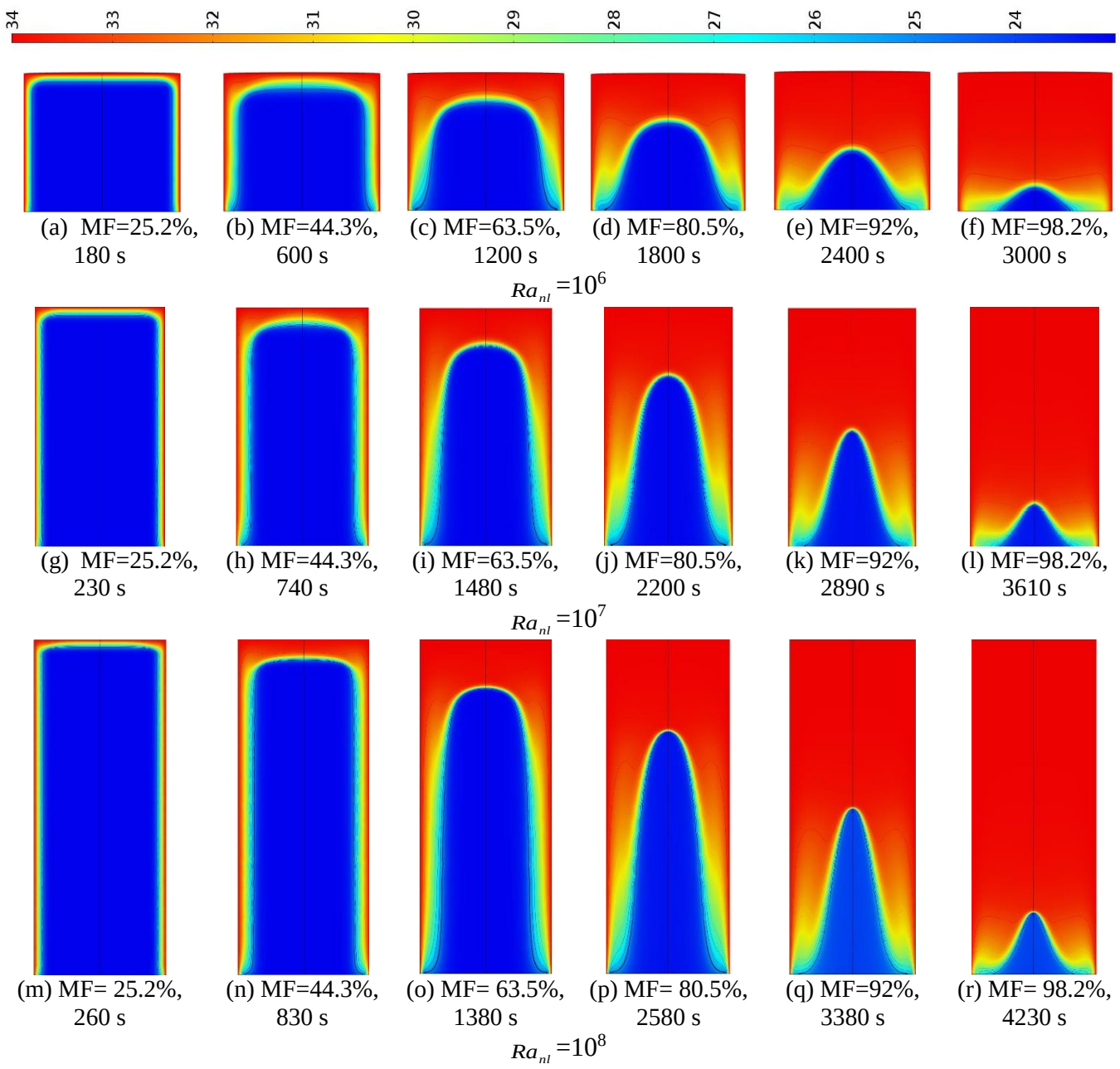

(a) MF=25.2%, 180 s (b) MF=44.3%, 600 s (c) MF=63.5%, 1200 s (d) MF=80.5%, 1800 s (e) MF=92%, 2400 s (f) MF=98.2%, 3000 s

$Ra_{nl}=10^6$

(g) MF=25.2%, 230 s (h) MF=44.3%, 740 s (i) MF=63.5%, 1480 s (j) MF=80.5%, 2200 s (k) MF=92%, 2890 s (l) MF=98.2%, 3610 s

$Ra_{nl}=10^7$

(m) MF= 25.2%, 260 s (n) MF=44.3%, 830 s (o) MF= 63.5%, 1380 s (p) MF= 80.5%, 2580 s (q) MF=92%, 3380 s (r) MF= 98.2%, 4230 s

$Ra_{nl}=10^8$

Fig. 5(a). Effect of different Ra_{nl} on the melting progression at different time for a given ϕ = 3% and the same MF.

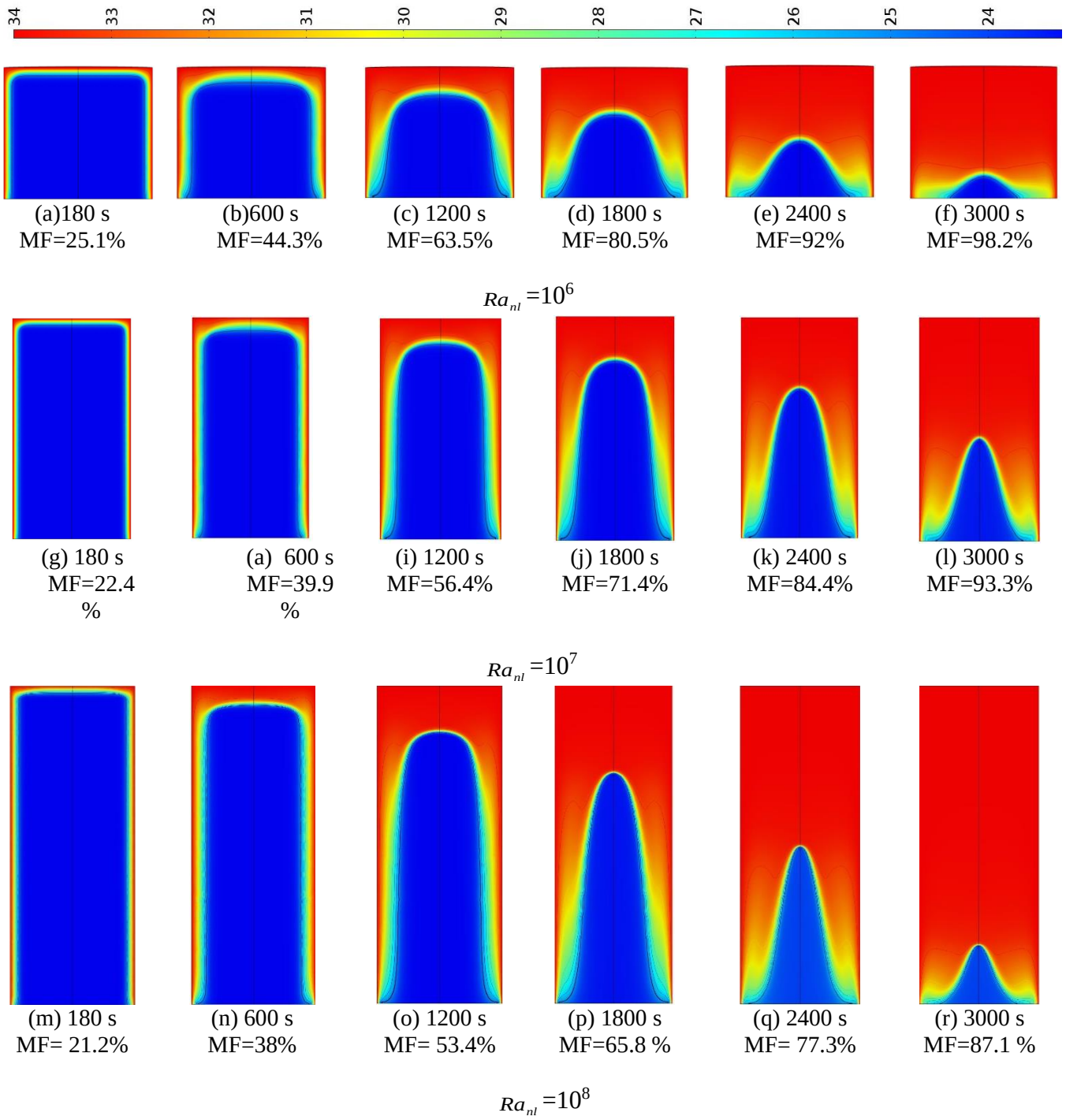

Fig. 5(b). Effect of different Ra_{nl} on the melting progression at the same time for a given ϕ = 3%.

Figure 6 presents the trend of melting fraction at different ϕ and Ra_{nl}. Due to the high temperature difference between hot wall and cold solid nano-PCM at the beginning of the melting process, the melting rate is high. Therefore, the slope of the melting fraction curvature at the beginning (e.g., 200 s) is higher than subsequent time intervals. As discussed earlier, dispersing nanoparticles into the PCM at the early stages showed an insignificant impact on the melting rate which can be clearly observed from MF-time plot for all ϕ. For better understanding, a quantitative comparison is presented in Table. 7 for time t= 300s.

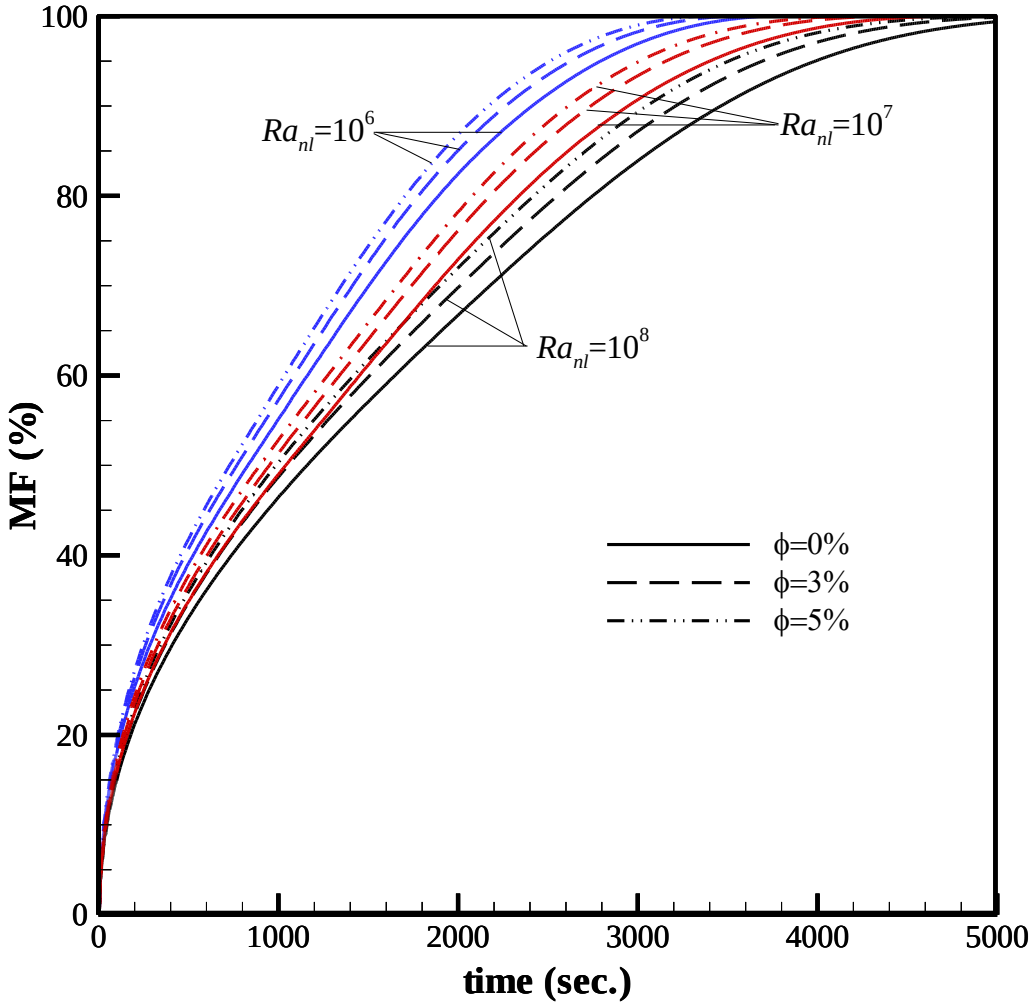

Fig. 6. Comparison of melting fraction between different volume fractions of nanoparticles (ϕ = 0, 3, and 5 %) and Ra_{nl} = 10^6, 10^7, and 10^8, H/D= 0.8, 1.73, and 3.74.

Table 9: MF and its increment by dispersing of nanoparticles at 300 s

	$Ra_{nl} = 10^6$	$Ra_{nl} = 10^7$	$Ra_{nl} = 10^8$
ϕ = 0%	30.7% (0.0%)	27.3% (0.0%)	25.8% (0.0%)
ϕ = 3%	32% (+4.2%)	28.7% (+5.1%)	27.1% (+5%)
ϕ = 5%	32.9% (+7.1%)	29.6% (+8.4%)	28% (+8.5%)

Temperature increased faster in the nano-PCM than the pure PCM due to higher thermal conductivity, resulted in a higher melting rate in nano-PCM than pure PCM. Adding nanoparticles to the PCM reduces the latent heat of fusion of the nano-PCM, which implies that less amount of energy is required for melting as long as the difference between the hot lateral wall temperature and the melting temperature of the nano-PCM remains constant. As a result, higher melting rate is expected after adding nanoparticles. It is clear from Fig. 6 that the nano-PCM having ϕ = 5% shows a higher melting rate than nano-PCM with ϕ = 3%. However, adding higher volume fractions of nanoparticles does not always lead to a proportional increase in the melting rate. The reason behind this statement is that, in general cases (except heavy oils used as the PCM) adding nanoparticles to a PCM, increases the viscosity of the PCM, which will suppress the natural convection during the melting process [9, 35]. Although increasing the height of the filled nano-PCM in the C-TES system will increase the heat transfer area, it increases the quantity of the nano-PCM as well, which requires more time to melt. At the last stages of the melting process, the enclosure is occupied by the liquid nano-PCM followed by a small amount of solid nano-PCM at the bottom of the enclosure. The interface area between the solid and liquid nano-PCM is relatively small. Therefore, melting process slows down towards the end resulting in a change in the slope of the MF-time curve.

2.3.2. Trend of the surface-averaged *Nu* number

In this section, attention is given to characterize and discuss the surface average heat flux, which is presented as dimensionless Nusselt number (Nu_n). The transient variation of the surface-averaged Nu_n throughout the melting process is presented in Fig. 7.

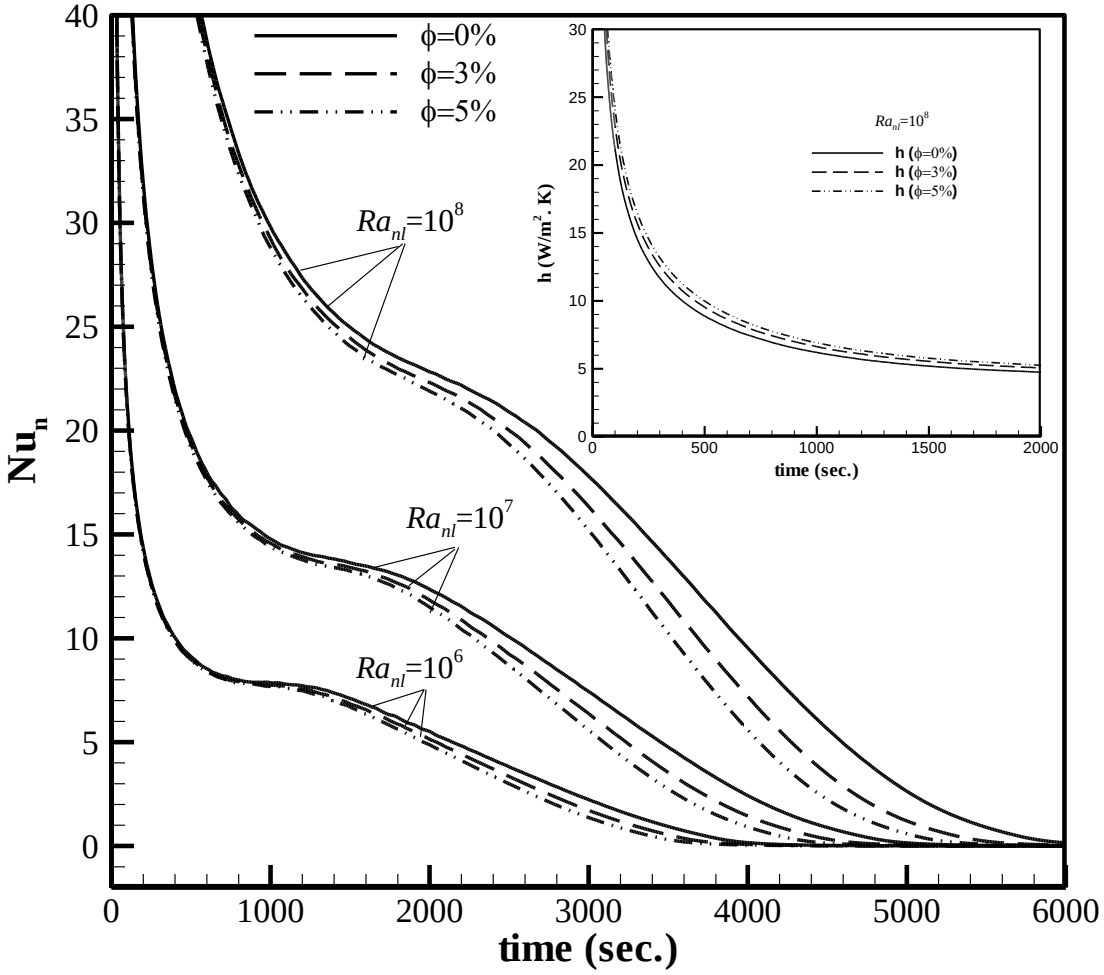

Fig. 7. Comparison of average Nusselt number based on k_{nf} for ϕ = 0, 3, and 5 %, Ra_{nl} = 10^6, 10^7, and 10^8 , H/D= 0.8, 1.73, and 3.74.

The Nu_n-time profiles in Fig. 7 exhibit a unique pattern variation at different time ranges during melting as opposed to the MF-time profile (see Fig. 6) where MF grows monotonically as time advances. As discussed earlier, the conduction dominates the melting process and creates a thin layer of liquid nano-PCM initially. The thermal resistance inside this thin liquid layer is relatively low, resulting in a relatively high temperature gradient and a high heat flux. Therefore, the magnitude of the Nu_n is higher at the initial stages of the melting process. This thin liquid layer

grows in the conduction dominated regime as time advances. As a result of that a sharp drop in the magnitude of the Nu_n is observed and this sharp drop is ceased at a particular time (depending on Ra_{nl}) with a clear change in the slope of Nu_n-time profile. The change in slope is an early indication of the formation of thermal boundary layer and the initiation of the convective motion at the upper part of the liquid layer. Heat transfer rate is relatively high inside this growing boundary layer region, while it is still the opposite inside the diminishing conduction dominated regime. Therefore, the two opposing trends in heat transfer inside the mixed convection and conduction regime (i.e., the transition regime) causes the slope change in Nu_n-time profile. As discussed in Bejan [26], Nusselt number remains constant (i.e., independent of time variation, but function of Rayleigh number) inside a fully convection dominated melting regime where height of the remaining solid PCM remains equal to the enclosure height until a particular time. A true fully convection dominated regime does not exist in the current study; instead convection dominated melting occurs in parallel with the shrinking solid nano-PCM. Therefore, just after the conduction regime diminishes completely, another change in the slope is observed in the Nu_n-time profile. Throughout the combined convection dominated and shrinking solid nano-PCM regime, Nu_n drops as time advances. At the end of the melting process, where nano-PCM is melted completely, the liquid nano-PCM reaches to a thermal equilibrium with the wall temperature while ceasing any heat transfer through the wall, Nu_n drops to a minimum value with final change in the slope of Nu_n-time profile. In the conduction dominated regime, Nu_n variations with time is nearly unaffected by any change in ϕ. Note that, in the pure conduction dominated melting zone, Nu_n is proportional to the ratio of wall heat flux to the thermal conductivity of the nano-PCM. As discussed earlier, both wall heat flux and thermal conductivity increase with increasing ϕ in the conduction regime, Nu_n remains nearly unchanged with changing ϕ in this regime. Gradual variation in the magnitude of Nu_n with changing ϕ is observed in the transition and subsequent regimes of melting. It is observed that adding nanoparticles into the PCM decrease the magnitude of the Nu_n where a larger reduction in the magnitude is observed for greater ϕ, specifically, toward later stages of combined convection and shrinking solid regimes. Note however that a reduction in Nu_n does always imply a reduction in the heat transfer rate. To assist this concern further, the behavior of the convective heat transfer coefficient (h) at different ϕ is plotted within Fig. 7. A

higher value of h is observed at larger ϕ. As Nu_n is proportional to h/k_{nf}, a reduction in Nu_n in this case refers to a smaller h/k_{nf} at higher ϕ. Additionally, at a given time, the magnitude of Nu_n is higher at higher Ra_{nl} as expected. Nu_n-time profile requires more time to reach its last asymptote (i.e., $Nu_n \to 0$; the thermal equilibrium point) when Ra_{nl} is higher.

2.3.3. Energy Stored

Figure 8 presents energy stored inside the C-TES system with time for selected values of volume fraction of nanoparticles and Rayleigh number. For ϕ=0, 3%, and 5%, the transient variation in the energy stored is presented at $Ra_l = 10^6$. Two additional profiles, representing $Ra_{nl} = 10^6$ at ϕ =3% and 5%, are presented as well for comparison purpose. Focusing on a single profile of transient variation in the energy stored given in Fig. 8 (e.g., Ra_l =10^6 and $\phi = 0\%$), it is observed that stored energy increases from zero to a maximum value as time advances during the melting process. However, the rate of energy stored is initially high which can be confirmed from the high slope of the profile at the beginning of the melting process. The relatively higher magnitude of the temperature gradient at the early stage of melting (i.e., in the conduction regime) assists transfer of larger amounts of energy and subsequently storing it. A change in the slope of the profile is observed near the time where transition melting regime (i.e., the conduction + convection melting regime) is evolved. From this point onward, energy is stored with an almost linearly increasing trend as time passes through the remaining transition regime and most part of convection with shrinking solid regime. Towards the end of melting, the rate of the stored energy decreases to its minimum where the maximum degradation of the temperature gradient occurs as the thermal equilibrium is achieved inside the enclosure.

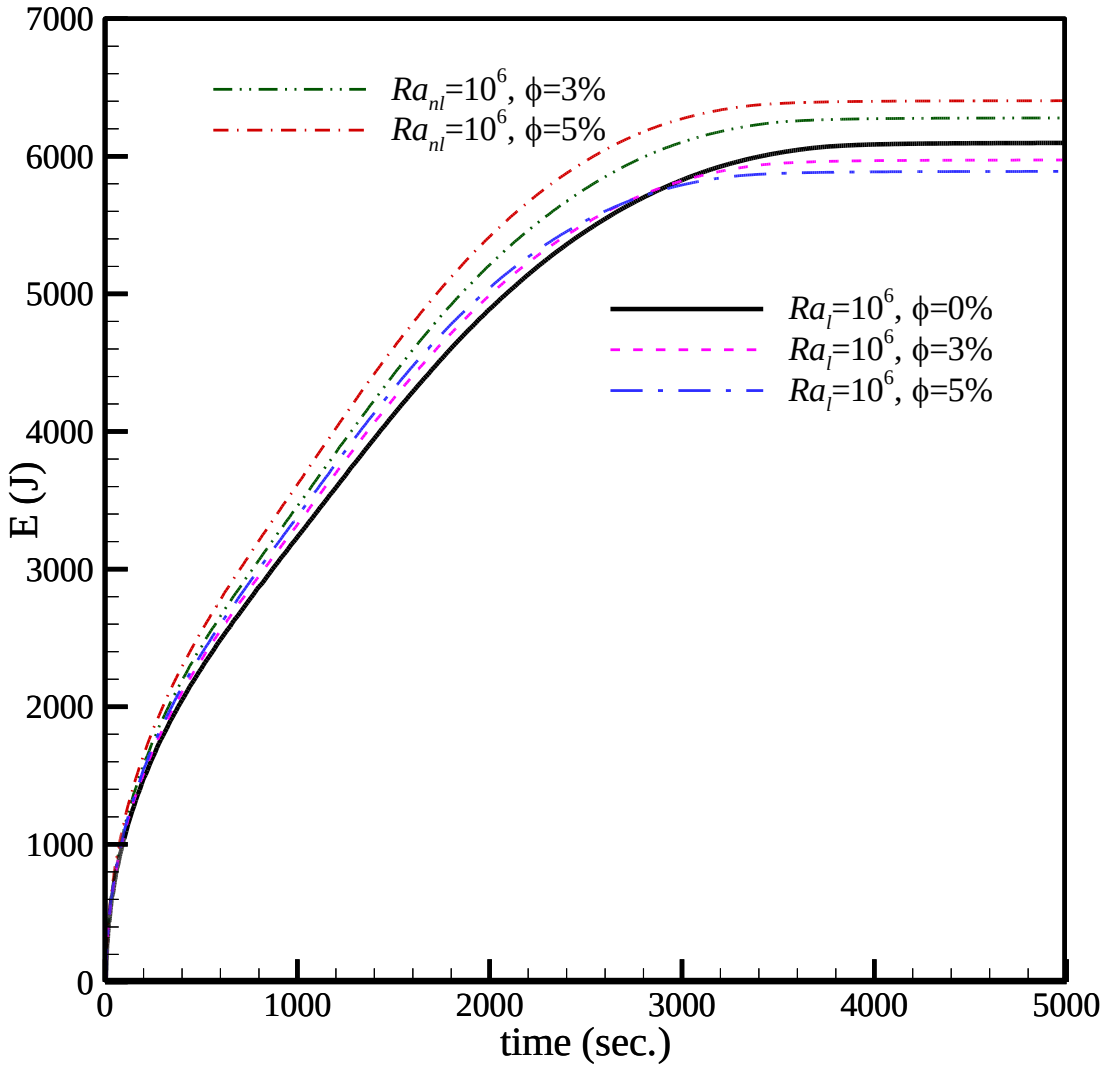

Fig. 8. Comparison of total energy stored inside the C-TES system for different volume fractions of nanoparticles (ϕ = 0, 3, and 5 %) and Ra_{nl}, Ra_l =10^6, H/D= 0.8, 1.73, and 3.74.

At the beginning of the melting process, where a large portion of the enclosure is filled with solid nano-PCM, energy storing mainly depends on the specific heat capacity of solid nano-PCM, i,e., $(\rho C_p)_{ns}$. The improvement of this specific heat capacity with increasing ϕ is nearly insignificant; for example, a 0.06% increase of $(\rho C_p)_{ns}$ is calculated when ϕ is changed from 0% to 5%. Therefore, almost no variation is observed in the energy stored profiles at different ϕ in the conduction regime of melting. From the thermophysical property values, it can be shown that the

specific heat capacity of liquid nano-PCM $(\rho C_p)_{nl}$ increases with increasing ϕ, while the latent heat capacity (ρh_{nl}) of nano-PCM decreases with increasing ϕ. Therefore, beyond the conduction regime of melting, storing energy inside the enclosure largely depends on specific heat capacities of solid and liquid nano-PCMs, latent heat capacity, and the relative magnitudes of these heat capacity values, respectively. Overall, increasing ϕ slightly decreases total energy stored inside the enclosure given that the size of the enclosure is unchanged (i.e., Rayleigh number is defined at base properties). Note that the size of the C-TES system should be increased to keep the Ra_{nl} constant with increasing ϕ. Therefore, due to the enlarged size, total energy stored in the C-TES system at $Ra_{nl}=10^6$ is higher than at $Ra_l=10^6$ when ϕ is constant.

Figure 9 illustrates energy stored inside the C-TES system with time for a given of ϕ at Ra_{nl} of $10^6, 10^7,$ and 10^8, respectively.

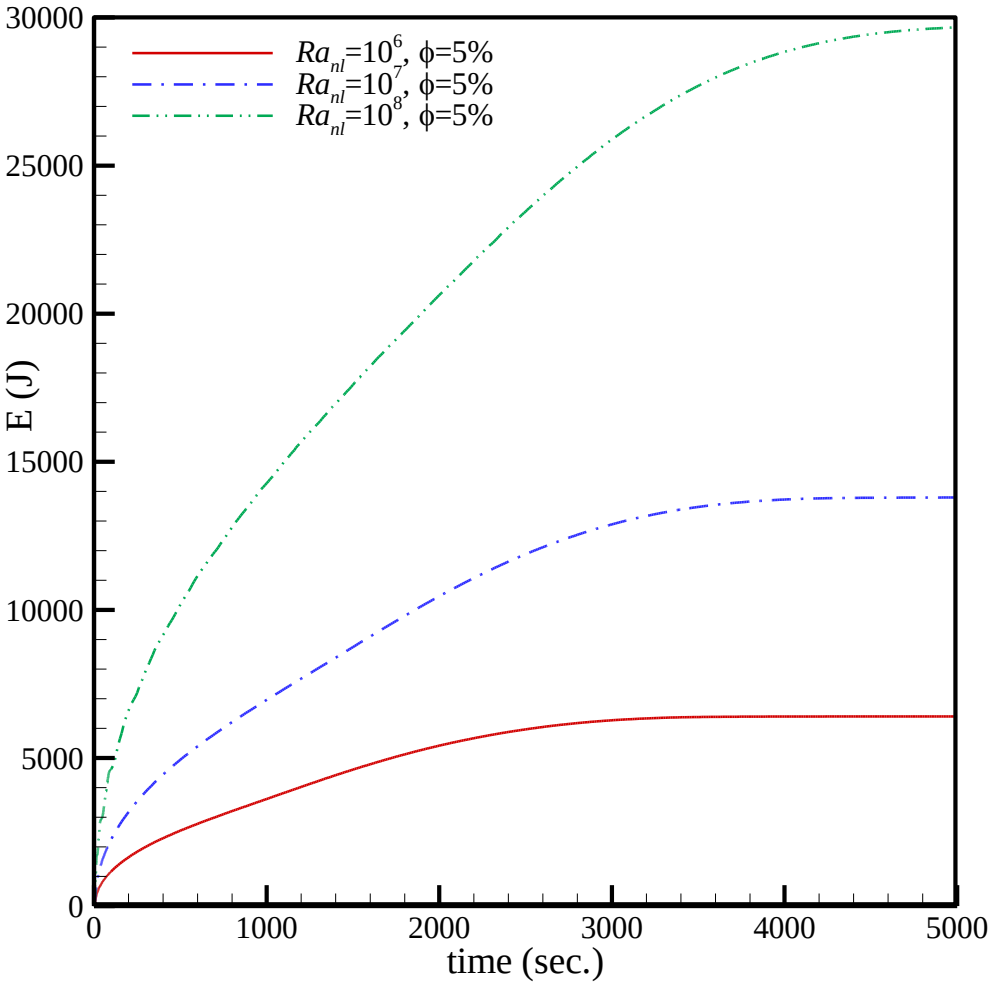

Fig. 9. Comparison of total energy stored inside the C-TES system for different Ra_{nl} (=10^6, 10^7, and 10^8 , H/D= 0.8, 1.73, and 3.74) and ϕ = 5 %.

A general trend of increased energy stored at larger Rayleigh number is observed. A higher slope is observed at larger Rayleigh number which is expected due to the larger amount of heat transfer through the wall. Very high energy storage is observed initially which approaches an almost steady value later when melting process is dominated by natural convection for all the three selected values of Rayleigh number. The difference in energy stored with Rayleigh number is less during the beginning of the melting; as melting reaches in the convection dominated regime, a larger difference is observed due to increased melting with Rayleigh number in convection regime.

2.3.4. Comparison with Experiments

In this section, some selected results obtained from current numerical simulation are compared to the results obtained from subsequent experimental analysis. For this purpose, an experimental setup is constructed to perform the melting experiment and images are captured during the melting process of the nano-PCM inside the C-TES system. A schematic diagram of the complete experimental setup is presented in Fig. 10.

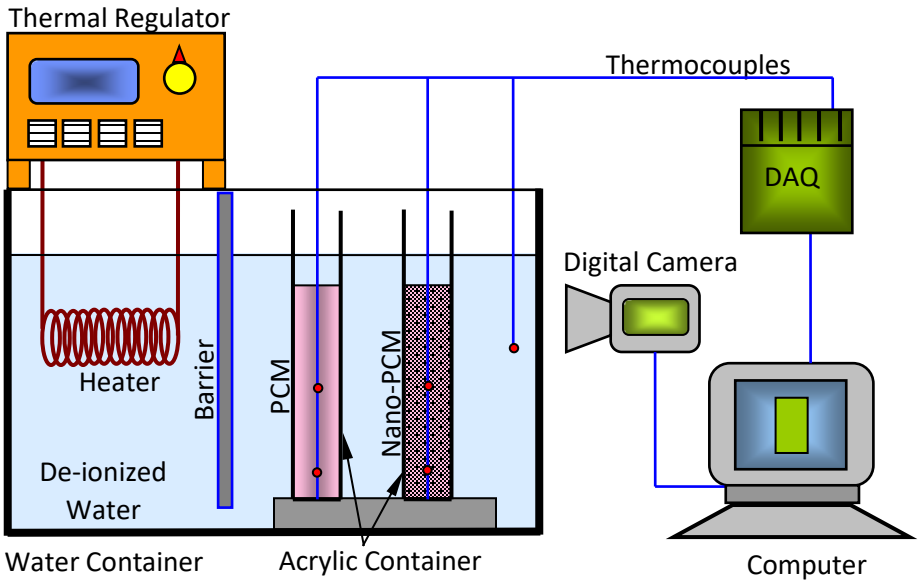

Fig. 10(a). Schematic diagram of the experimental setup used for visualization

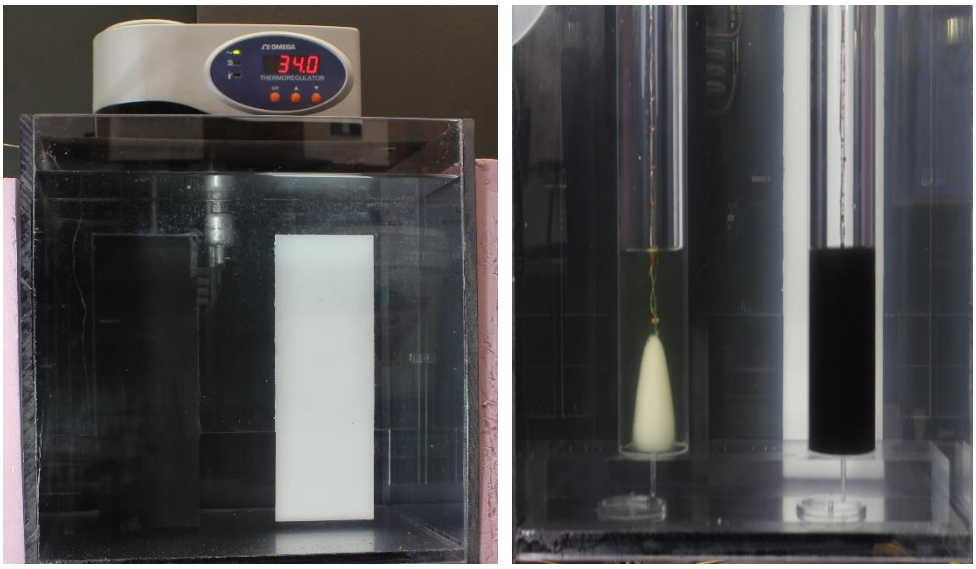

(i) (ii)

Fig. 10(b). Experimental setup: (i) Constant temperature bath (ii) C-TES system inside the constant temperature bath during the melting process

The setup consists of an acrylic water tank, which is insulated from all of its sides except one for visualization, a water heater equipped with a circulatory pump, a digitally controlled thermal regulator, T-type thermocouples, and a 16-channel DAQ system. The acrylic tank is divided into two parts by using a barrier to avoid the intensity of the water circulation caused by the circulatory pump. A 5cm clearance is maintained between the bottom of the acrylic water tank and lower part of the barrier. Melting experiments are performed on both PCM and nano-PCM simultaneously in order to ensure exactly same experimental environment and to avoid any discrepancy due to the change in minor environmental condition. To ensure this, two vertical C-TES systems are constructed by using acrylic pipes with inner diameter of 4.44 cm and thickness of 0.3 cm. These two enclosures are insulated from the bottom and firmly attached to a 2.5 cm thick acrylic plate by using transparent acrylic cement. The center-to-center distance between the two enclosures is 14 cm. To prepare the nano-PCM, 50 mg of copper oxide nanoparticles are dispersed into 350 ml of molten coconut oil at the temperature of 60°C. To ensure the homogeneity of the mixture, it is stirred by a magnetic stirrer (model: SP88854100, manufacturer: Thermo Scientific) initially for 12 hours. Then an ultrasound sonicator (model: Q500, manufacturer: Qsonica) is used to improve

the homogeneity of the mixture further, to minimize the sedimentation, and to release the trapped air inside the nano-PCM. Subsequently, one enclosure is filled with H=8.5 cm of nano-PCM (Ra_{nl} =1.3×10^7), while the remaining is filled with H=8.6 cm of pure PCM (Ra_{nl} =1.35×10^7). It is worth mentioning that visualization process becomes increasingly difficult for the nano-PCM, specifically at higher values of ϕ, due to its dark black color. Therefore, a relatively lower value of ϕ is selected as our intention is to make a comparison of melting images obtained from numerical simulation and experimental visualization. The PCM and nano-PCM-filled enclosures are put inside a constant temperature bath where water is maintained at 21˚C using a low temperature thermal regulator. Subsequently, multiple melting and solidification processes are conducted to ensure the stability of the mixture and to release the trapped air inside the PCM and nano-PCM. Next, the enclosures are placed inside the acrylic water tank where the temperature of the water is elevated and maintained at 34˚C (10˚C above the T_m) to initiate the melting process. A digital camera is used to capture images periodically to track the liquid-solid interface during the melting. For eight selected times, images obtained from numerical simulation and experimental visualization are presented and compared in Fig. 11 for pure PCM and Fig. 12 for nano-PCM, respectively. Corresponding melting fractions are presented as well.

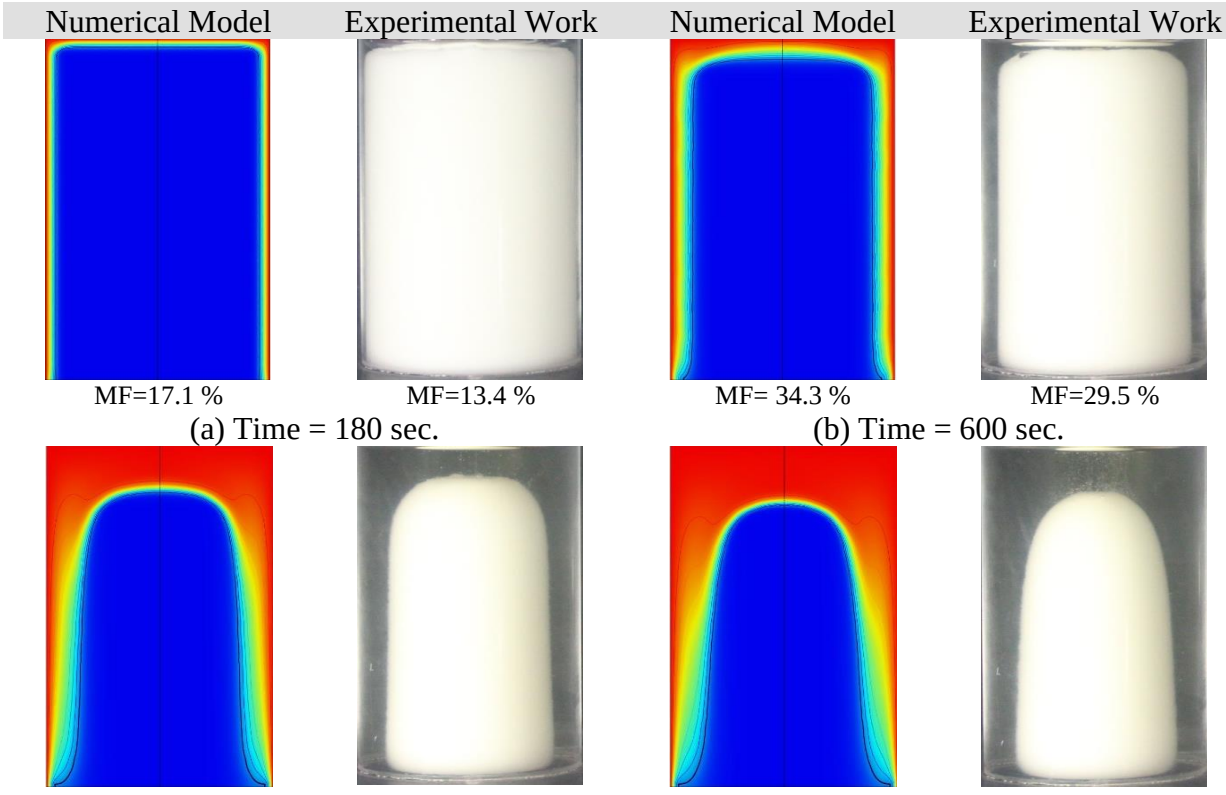

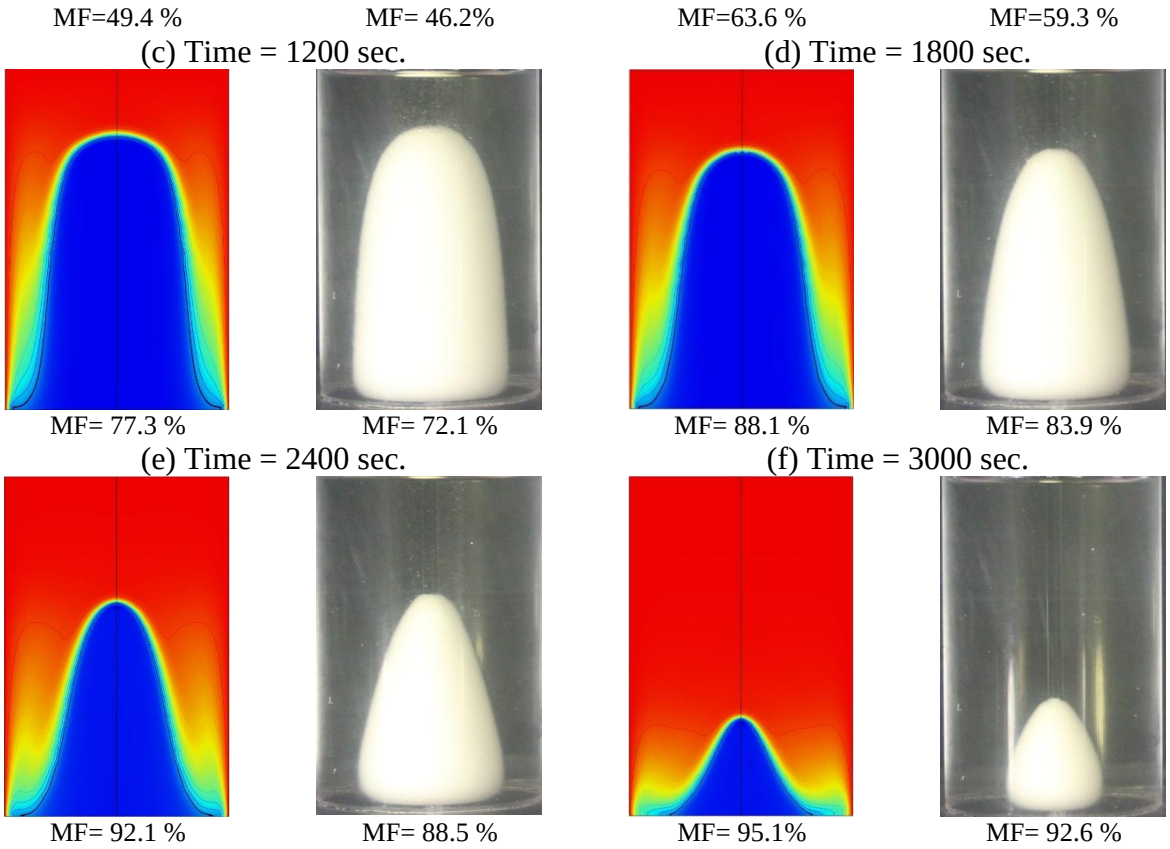

Fig. 11. Melting visualization comparison between numerical and experimental works for pure PCM, $Ra_{nl} = 1.35 \times 10^7$, and H= 8.6 cm.

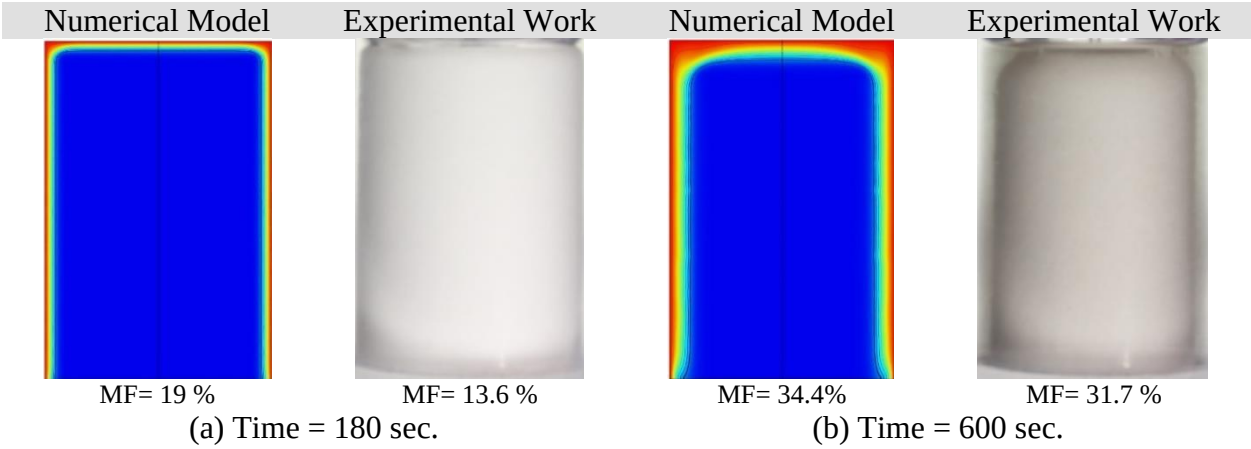

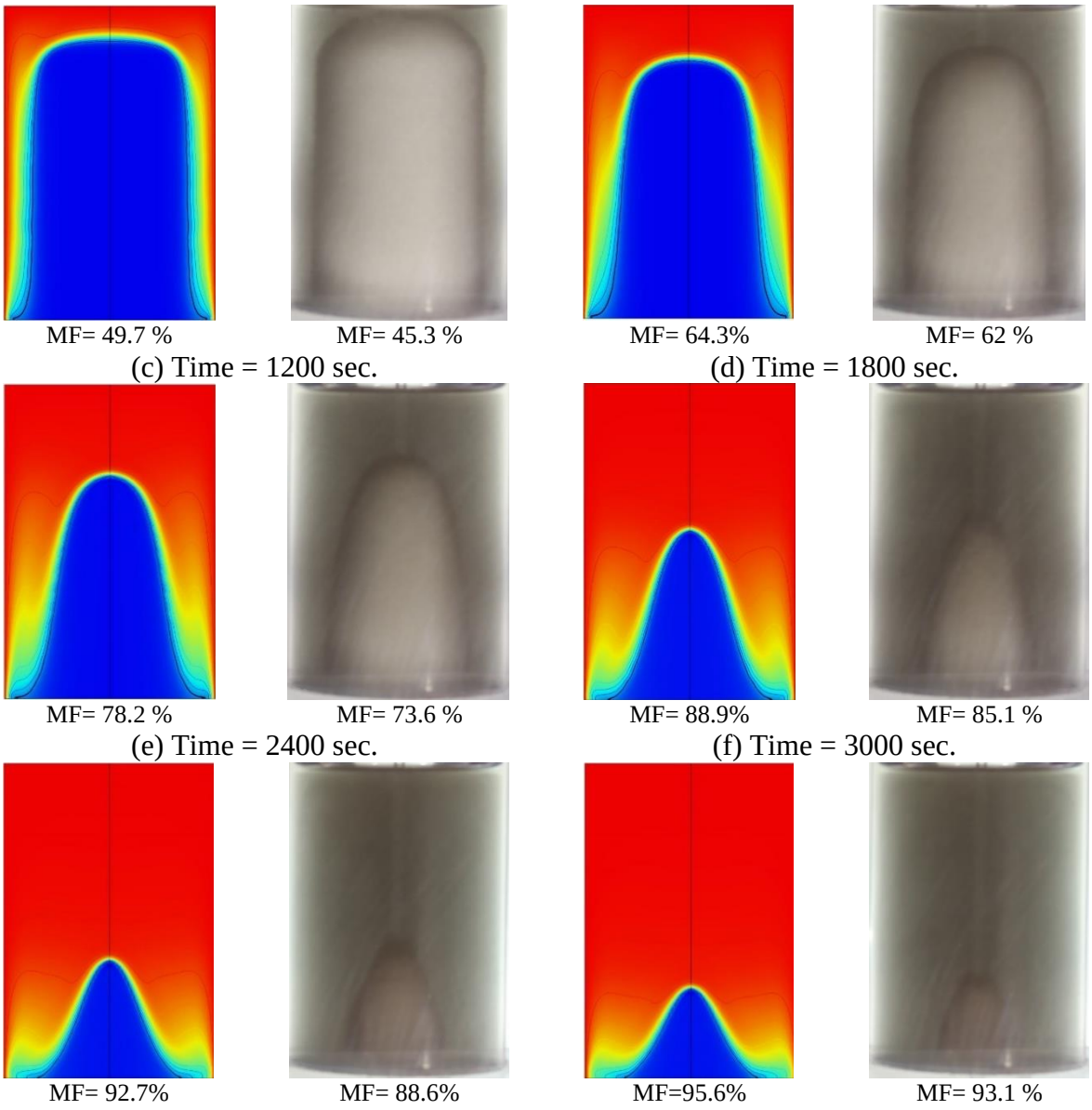

Fig. 12. Melting visualization comparison between present numerical and experimental works for nano-PCM (0.05 gr CuO+ 350 ml coconut oil), $Ra_{nl} = 1.3 \times 10^7$, and H=8.5 cm.

The selected images cover almost the entire range of melting regimes, which exhibit the different characteristic features of the melting process as given below:

(a) Images at t=180 and 600 s: At these time intervals, the solid-liquid interface is parallel to the walls, a pattern resembles the conduction dominated melting process as discussed earlier. By comparing the numerical model and experimental images, an almost identical pattern can be

observed. However, the thickness of the liquid PCM or nano-PCM layer close to the lateral walls in numerical simulation seems to be slightly larger than the experimental images. The top part of the remaining solid PCM/nano-PCM is slightly more curved for the numerical work. The numerical model showed a higher melting fraction for both pure PCM and nano-PCM.

(b) Images at t=1200 and 1800 s: At these time intervals, the warm liquid PCM/nano-PCM starts to move upward as the buoyancy forces overcome the viscous forces. Higher temperature liquid PCM/nano-PCM are accumulated at the top due to the thermal stratification effect. As a result, the remaining solid PCM/nano-PCM resembles a dome shape. A slightly flatter curvature at the top can be observed in the numerical work for both PCM/nano-PCM. As it can be seen from the melting fraction values under each image, the magnitude of the numerically obtained melting fractions are higher than the experimentally obtained values.

(c) Images at t=2400 and 3000 s: As natural convection develops, the remaining solid part tends to have an inverted paraboloid shape. For the pure PCM, the experimental images show a sharper curvature at the top than numerical work. However, an opposite behavior exists at the same time for nano-PCM. At these time intervals, the discrepancy of the melting fraction between numerical models and experimental work increases.

(d) Images at t=3300 and 3600 s: Most discrepancy in the melting pattern between numerical models and experimental works is seen here. A sharper curvature at the top of the remaining solid PCM/nano-PCM is observed.

In general, a good agreement between numerical model and experimental work is achieved. However, there are some discrepancies observed in melting pattern and melting fraction. Several factors can possibly be the reasons for such discrepancies. One of the possible major factors is the conduction resistance due to finite thickness of the acrylic pipe, which is ignored during numerical simulation. This resistance may reduce heat transfer rate slightly in the experimental work even though the outer surface temperature is kept constant in both the numerical simulation and the experiment work. In addition to that, in the experimental work an expansion of the nano-PCM is seen in the enclosure during melting process. However, this phenomenon is ignored in the numerical model. Other minor factors may include the difference between the thermophysical properties based on property models and exact property values, heat loss through the bottom of the enclosure, and minor water temperature fluctuations in the acrylic tank. Table 9 shows the

difference between melting fraction calculated by the numerical model and experimental work for pure PCM and nano-PCM as it is discussed earlier in this section (i.e. Figure 11 and Figure 12).

Table 10: A comparison between melting fraction (%) calculation by numerical model and experimental work

Time(s)	pure PCM			nano-PCM		
	Numerical	Experimental	Difference (%)	Numerical	Experimental	Difference (%)
180	17.1	13.4	21.6	19	13.6	28.4
600	34.3	29.5	13.9	34.4	31.7	7.8
1200	49.4	46.2	6.4	49.7	45.3	8.8
1800	63.6	59.3	6.7	64.3	62	3.5
2400	77.3	72.1	6.7	78.2	73.6	5.8
3000	88.1	83.9	4.7	88.9	85.1	4.2
3300	92.1	88.5	3.9	92.7	88.6	4.4
3600	95.1	92.6	2.6	95.6	93.1	2.6

2.4 Conclusion

The melting process, heat transfer and energy storage characteristics of a bio-based nano-PCM in a C-TES system are numerically investigated and verified with experimental work. The C-TES system is assumed to be filled with copper oxide nanoparticles dispersed in coconut oil at different ϕ and different Ra_{nl}. The modeling results are compared with previously published numerical and experimental works and a good agreement is achieved. The following conclusion can be drawn from the obtained results:

- Initially, the melting process is dominated by conduction. As time advances, the buoyancy force is able to overcome the viscous force, resulting in a gradual increase in the domination of natural convection melting. For a certain period of time, mixed conduction and convection remain dominant mode of melting, while the influence of the conduction diminishes with time. Subsequently, the melting process is dominated by convection while the height of the solid nano-PCM shrinks as time advances. The shape of the remaining solid nano-PCM is controlled by these regimes at each stage.

- Adding copper oxide nanoparticles to coconut oil does not show a significant effect on the melting rate at the early stages of melting process. However, as time advanced, dispersion of copper oxide nanoparticles to coconut oil improves the melting rate in the PCM.
- The magnitude of the Nusselt number is higher at the initial stages of the melting process due to the relatively high temperature gradient and a high heat flux at this stage. Nusselt number drops sharply from a large value in the conduction regime as time advances. A change in slope in the Nusselt number profile is an indication of the formation of thermal boundary layer and the initiation of the convection. This slope change strongly depends on the Rayleigh number. A fully convection dominated regime does not exist, instead convection dominated melting occurs in parallel with the shrinking solid nano-PCM. Nano-PCMs with higher volume fractions of nanoparticles exhibit larger convection heat transfer coefficients.
- Increasing volume fractions of nanoparticles decreases total energy stored inside the C-TES system given that the size of the enclosure is unchanged (i.e., Rayleigh number is defined at base properties). However, opposite nature in the energy storage rate is observed if the Rayleigh number is defined based on nano-PCM properties.
- Finally, numerically obtained solid-liquid interface locations and melt fractions for base PCM and nano-PCM are compared with experimental analysis and a very good agreement is obtained which gives confidence in the obtained numerical results.

2.5 Nomenclature

c_p	specific heat at constant pressure [kJ/kg K]
g	gravitational acceleration [m/s^2]
H	height of the filled nano-PCM [cm]
h_{nl}	latent heat of fusion [kJ/kg]
k	thermal conductivity [W/m.K]
R	inner radius of the C-TES system [cm]
T	temperature [$^\circ$C]

Greek symbols

α	coefficient of thermal diffusivity [m^2/s]
β	coefficient of thermal expansion [1/K]
μ	dynamic viscosity [Pa.s]
ϕ	density [kg/m^3]
ϕ	volume fraction of nanoparticles

Subscripts

h	hot
l	liquid PCM
m	melt
n	nanoparticles
nl	liquid nano-PCM
ns	solid nano-PCM
s	solid PCM
0	initial

Abbreviation

C-TES	Cylindrical thermal energy storage system
TES	thermal energy storage
LHTES	latent heat thermal energy storage system
MF	melting fraction
PCM	phase change material
RT	Rubitherm (www.rubitherm.eu)
Ra_{nl}	Rayleigh number based on liquid nano-PCM properties, $Ra_{nl} = \frac{g\ \beta_{nl}\ H^3 (T_h - T_m)}{\nu_{nl}\alpha_{nl}}$

Chapter 3

Detailed Experimental Investigation of the Melting Process of a Bio-based Nano-PCM (copper oxide nanoparticles dispersed into coconut oil) filled Vertical Cylindrical Thermal Energy Storage System

"A version of this chapter has been submitted: Soroush Ebadi, Syeda Tasnim, Amir A. Aliabadi , Shohel Mahmud, "Geometry and nanoparticle loading effects on the Bio-based Nano-PCM filled Cylindrical Thermal Energy Storage System**",** Applied Thermal Engineering (Elsevier), 2017 (ATE_2017_5407)."

3.1 Introduction

Nowadays, one of the main environmental concerns is the increase in the amount of greenhouse gas emissions due to the widespread use of fossil fuels. Such greenhouse emissions have a significant impact on the global warming. The global warming concern leads to efforts for developing systems that utilize energy sources more effectively. One of the major solutions to this concern is storing energy efficiently, which can be transformed to the required form necessary for subsequent operations. Storing energy can play a significant role to balance the amount of demand and supply, reduce the level of carbon dioxide (CO_2) emissions from burning fossil fuels, and play a vital role in conserving energy [1]. Thermal Energy Storage (TES) systems have been developed for storing thermal energy by heating or cooling a specific medium. TES systems have been used in many different applications including heating and cooling purposes or generating power. TES systems are divided into three major groups: (i) Sensible Heat Thermal Energy Storage (SHTES), (ii) Latent Heat Thermal Energy Storage (LHTES) and (iii) Thermo-Chemical Energy Storage (TCES) systems. The SHTES system is based on raising (or lowering) the temperature by heating (or cooling) of a liquid or solid storage medium, while LHTES uses Phase Change Materials (PCMs) to store (or release) thermal energy during the PCM's melting (or solidification) process. In other words, thermal energy will be absorbed (i.e., the charging process) by a PCM during its melting stage if a thermal source with the temperature higher than the melting point of PCM is exposed to the LHTES system. Similarly, thermal energy will be released (i.e., the discharging process) by a PCM during its solidification stage if a thermal sink with a temperature lower than

the melting point of PCM is exposed to the LHTES system. The LHTES system has two main advantages over SHTES systems: (i) higher energy storage density and (ii) smoother temperature fluctuations [2]. It is already shown that a LHTES system has the potential of storing thermal energy 5-14 times higher than SHTES systems [1]. The TCES system benefits from a specific chemical reaction in order to release or store heat and the amount of heat stored relies on the quantity of storage medium, endothermic heat of reaction, and the bound of conversion [1]. The most common PCMs are paraffin waxes, hydrated salts, and organic/non-organic compounds, which have been used in a wide variety of applications based on their melting temperatures and heat capacities. For instance, PCM with melting temperature below 15°C can be used in air conditioning systems for generating cooling, while a PCM with the melting temperature in a range 15°C - 90°C can be used for heating applications. However, traditional PCMs have several practical limitations including low thermal conductivity, which leads to low heat transfer rate during charging and discharging, weak thermal stability, and immature sub-cooling effect [3]. In order to enhance the thermal conductivity of a PCM, various methods can be used including dispersing highly conductive nanoparticles in PCM (nano-PCM), inserting metal fins, using porous materials, and use of foams [4]. Due to adding nanoparticles at different weight/volume fractions to a PCM, sedimentation can occur with time (more likely at high weight/volume fractions). As a result of sedimentation, the ability of enhancing thermal conductivity will be degraded as time furthers [5, 6] which may pose a challenge to nano-PCM TES systems. To decrease the amount of sedimentation, different methods, such as, application of intensive ultrasonic vibration to nano-PCM using an ultrasonic vibrator [6] and use of different surfactants [6, 7] have been utilized.

Convection and conduction are the major modes of heat transfer encountered during charging and discharging processes, which are greatly influenced by the geometric and compositional properties of a LHTES system. Different types of geometries including rectangular, cylindrical, and spherical have been used for a TES system. For required specific applications, cylindrical enclosures can be used both vertically and horizontally [8]. This is the reason why cylindrical enclosure geometry is chosen for the present study. By surveying the literature, it can be found that a considerable number of published works are available regarding the use of cylindrical enclosures for a TES system.

Starting with horizontal cylindrical TES systems, Jourabian et al. [9] applied Lattice Boltzmann method to observe the effect of adding copper nanoparticles to water during a melting process. It

is reported that increasing the amount of nanoparticles enhanced the melting rate but decreased the latent heat of fusion. The effect of adding copper oxide nanoparticles to n-octadecane PCM is studied both numerically and experimentally by Dhaidan et al. [10]. Authors reported an improvement in charging process at a lower amount of nanoparticles due to the effect of increasing viscosity and sedimentation. The volumetric heat generation effect during the phase change process of Rubitherm-27 (RT-27) and copper nanoparticles was performed by Bechiri and Mansouri [11]. The heat generation effect is identified less significant for high volume fractions of nanoparticles.

Regarding the use of vertical cylindrical enclosures, various research works are reported in the literature, mainly with pure PCM. For example, Jourabian and Farhadi [12] studied the convection melting of ice with copper nanoparticles in a vertical semi-circular enclosure and concluded that adding nanoparticles increased the thermal conductivity and reduced the latent heat of fusion. Zheng et al. [13] observed reduction in the natural convection due to adding carbon nanotubes inside a PCM filled vertical cylindrical enclosure heated from the bottom. Sciacovelli et al. [14] studied the effect of adding copper nanoparticles on the melting process inside a vertical single shell and tube heat exchanger. It was concluded that by using nano-PCM with the volume fraction of 4% the melting time is reduced up to 15 %. A numerical study on the melting process of RT-27 in a vertical circular tube was performed by Shamueli et al. [15] and later verified with previous experiments. The authors investigated the effect of a mushy zone parameter on the melting process. It was observed that experimental melting patterns were predicted closely by the numerical simulation when the mushy zone parameter was set equal to 10^8. An experimental investigation of the melting process of n-eicosane using a vertical cylindrical enclosure was performed by Sparrow and Broadbent [16]. It was reported that sub-cooling had a significant delaying impact on the melting process and reduced the rate of energy transfer required for melting. An analytical study of contact melting of a PCM in a vertical cylindrical capsule was conducted by Wenzhen et al. [17]. In this research, capsules were filled by eicosanoid as a PCM and heated isothermally from the bottom and sides. To investigate the rate of heat transfer through the contact liquid layer, the liquid film theory was used. The authors found that reducing aspect ratio was beneficial to increase the melting rate. Jones et al. [18] performed experimental and numerical studies of melting of n-eicosane as a PCM in a vertical cylindrical container. The authors reported that four melting regimes could occur during the melting process including (i) pure conduction, (ii) mixed

convection and conduction, (iii) convection dominant, and (iv) shrinking solid. In an extensive numerical analysis, Ebadi et al. [19] concluded that nano-PCM with higher volume fractions of nanoparticles improve the melt fraction and convection heat transfer coefficient but reduce both sensible and latent heat capacities of nano-PCM inside a cylindrical thermal energy storage system. Current literature indicates that a noticeable number of technical articles deal with the phase change processes of PCM inside enclosures with various shapes (e.g., [8]), while the study with regard to nano-PCM in enclosed space is limited (e.g., [4]), specifically, inside an open top vertical cylindrical enclosures with adiabatic bottom and isothermal side wall boundary conditions. This limitation in the current literature is the primary motivation behind the present study. Authors used a bio-based edible coconut oil PCM (T_m=24^{o}C) instead of paraffin- and petro-based PCMs (e.g., n-octadecane, n-eicosane), widely used in TES researches and reported extensively in the literature (e.g., [20, 21]). Paraffin- and petro-based PCMs exhibit excellent time transition characteristics (can be observed from their T-history curve) and ideal for many TES researches, but stability and sedimentation are widely reported limitations for such PCMs. In contrast, edible coconut oil PCM exhibits greater stability and less sedimentation with CuO nanoparticles, although the time transition characteristic feature for this PCM is not as ideal as paraffin- and petro-based PCMs. Furthermore, the coconut oil is less expensive, widely available, and having a melting temperature close to the typical room/lab temperature. A comprehensive experimental study is performed to study the melting process of bio-based nano-PCM inside vertical cylindrical enclosure which is a representative geometry of a thermal energy storage system. Effect of nanoparticle loading, boundary wall temperature, and height of the PCM/nano-PCM inside C-TES system on the melting process and temperature distribution is reported. An extensive analysis is reported as well to show how to calculate the uncertainty associated with image based melt fraction calculation.

3.2 Experimental work

In this section, a detailed description of the prototype cylindrical thermal energy storage (C-TES) system, preparation of nano-PCM, and experimental procedure are presented.

3.2.1 C-TES prototype system

To visualize the melting process of pure PCM and nano-PCM and to measure the temperature distribution at selected locations, an experimental setup and multiple prototype C-TES systems were constructed. Each C-TES prototype consisted of two transparent acrylic pipes with the height (H_0) of 33 cm, inner diameter (D) of 4.44 cm, and thickness of 0.3 cm (see Figs. 1(a) and (b)). Both pipes were attached to a 2.5 cm thick acrylic plate vertically with transparent acrylic cement (manufacturer: Scigrip). The center-to-center distance between the pipes is 14 cm. In the center of each pipe, a thin transparent acrylic rod of 3.23 mm diameter was installed vertically, where T-type thermocouples (manufacturer: Omega) at different heights (i.e., 15 mm and 35 mm from bottom) were installed firmly.

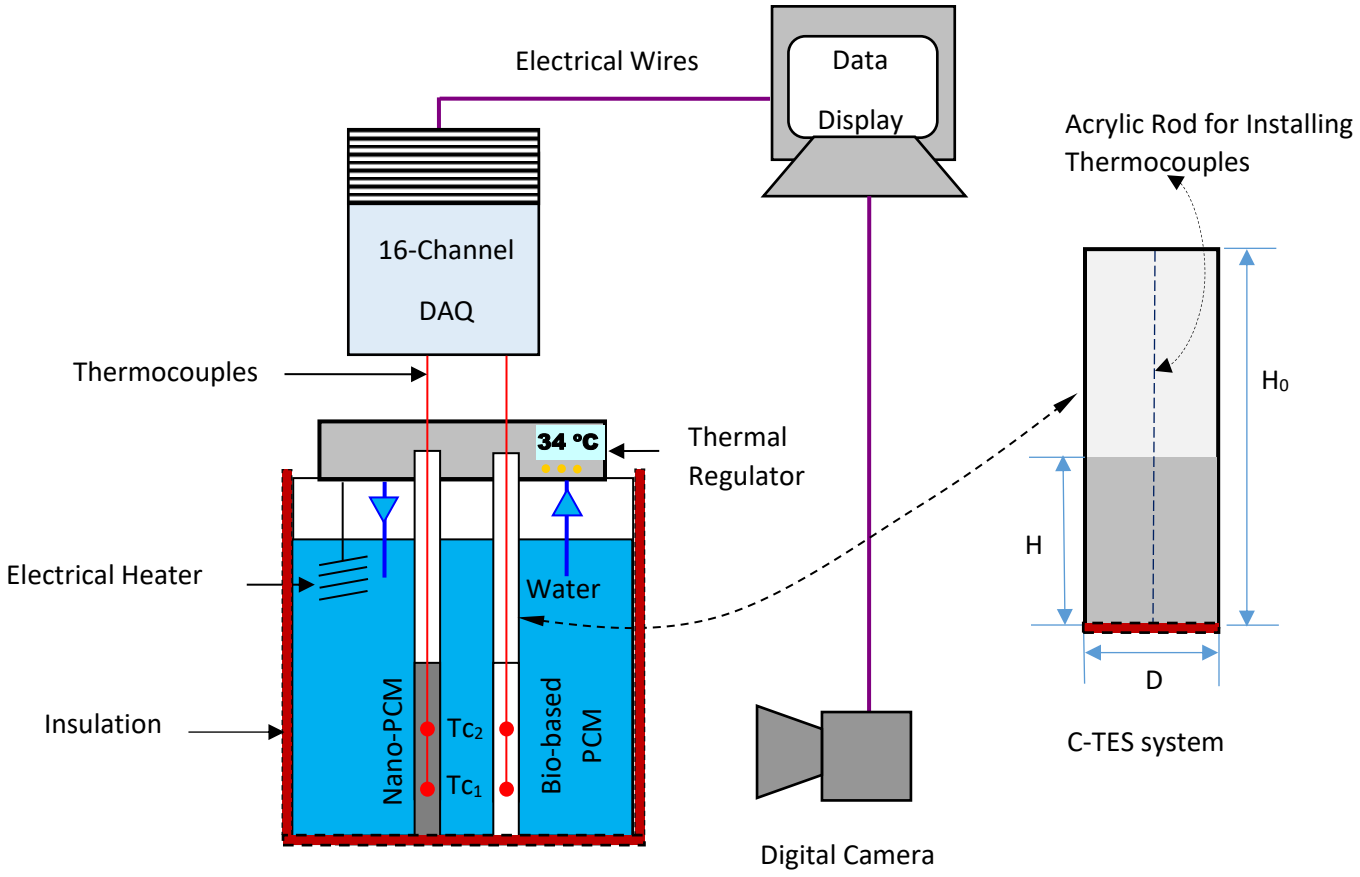

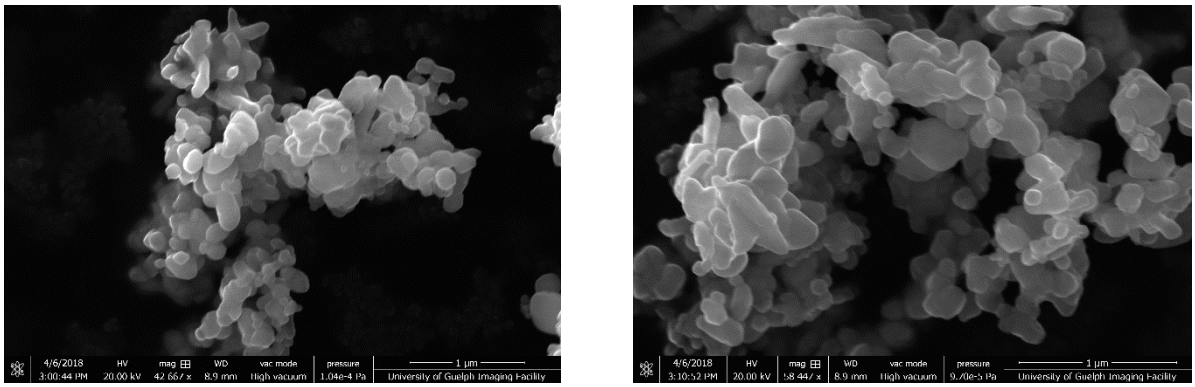

(c)

Fig.1. Schematic diagram of (a) experimental setup (b) C-TES system, and (c) SEM images of CuO nanoparticles

These pipes were kept open from the top to avoid having any pressure build up on the bio-based PCM and nano-PCM during melting experiments. The bottom part of the C-TES prototype was properly insulated. During each experiment, one of the C-TES system was filled with a bio-based PCM (coconut oil) and the second one was filled with a nano-PCM (copper oxide nanoparticles dispersed in coconut oil PCM).

3.2.2 Description of experimental setup

The main parts of the experimental setup consist of : (i) a 30cm × 30cm × 30cm acrylic water tank (with the thickness of 8mm), which is filled with deionized water, (ii) an immersion water heater with precision temperature controller (model: HCTB-3020, manufacturer : Omega) to create an isothermal environment, (iii) a recirculation pump to circulate water for maintaining uniform temperature, (iv) T-type thermocouples, (v) a 16-channel DAQ system (model : NI9213, manufacturer: National Instruments), and (vi) a digital camera (model: EOS rebel T5, manufacturer: Canon) to capture images periodically. The immersion heater was installed at one end of the water tank while the prototype C-TES system was placed on the other end. A barrier, made of an acrylic sheet (30 cm × 20 cm), was placed between the immersion heater and the C-TES prototype to avoid convection and turbulent effects associated with direct water movement. A 5cm gap was maintained between the barrier and the bottom surface of the water tank to allow hot water circulated around the C-TES system to have a uniform temperature for the experiment. The temperature inside the water tank was regularly monitored at different locations to ensure that the appropriate isothermal boundary condition was achieved before collecting the data. In addition,

to have clear images during the melting process, a part of the barrier was painted white (for nano-PCM) and another part was black (for pure PCM). A schematic of the experimental setup is shown in Fig.1 (a), while the schematic of the C-TES system is shown in Fig. 1(b).

3.2.3 Nano-PCM preparation

For the current experimental work, the Copper (II) Oxide (CuO) nanoparticles were purchased from Sigma-Aldrich in nanopowder form. Based on the information obtained from TEM analysis (provided by the manufacturer), the particle size is <50 nm. Thermophysical properties of the CuO nanoparticles are provided in Table 1. Images obtained from SEM analysis (Physics Department, University of Guelph) are given in Fig.1(c), which provide further information on the nanoparticles shape.

Table 1: Thermophysical properties of nanoparticles, PCM, and nano-PCM

Properties (units)	CuO nanoparticles [10]	Coconut Oil (Measured)			
		Solid (15°C)	Liquid (32°C) (wt.%=0.0)	Liquid (32°C) (wt.%=0.1)	Liquid (32°C) (wt.%=1.0)
ρ (kg/m^3)	6510.0	920	914	916	922
μ (Pa.s)	-	-	0.0326	0.0332	0.362
c_p (J/kg K)	540	3750	2010	2001	1995
k (W/m K)	18.0	0.228	0.166	0.174	0.290
h_f (kJ/kg)	-	-	103	101	94.5
T_m (ΔT_m)	-	24°C (±1°C)			

The refined form of the bio-based coconut oil was obtained from a local vegetable oil supplier. Thermophysical properties of pure coconut oil and nanoparticle enhanced coconut oil were measured in different labs at the University of Guelph. Following equipment/methods were used for property calculation:

- KD2 Pro and TPS-500 system (for thermal conductivity),
- Rotational Viscometer and Vibration Viscometer (for dynamic viscosity),
- DMA 35 Density meter (for liquid density),
- Differential Scanning Calorimeter (DSC) (for specific heat and heat of fusion), and
- Melting Point Apparatus MPS10 (for melting temperature).

Thermo-physical properties of CuO nanoparticles, pure PCM, and nano-PCM and are presented in Table 1.

Nano-PCM with different weight fractions of nanoparticles were prepared before experiments. Initially, a selected amount of coconut oil was melted and filled in a graduated beaker. At the next step, the required amount of nanoparticles to achieve a desired weight fraction was weighed by a precise balance (model: XP6, manufacturer: Mettler Toledo) and added to the PCM filled beaker. The mixture temperature was raised to 60°C and then stirred by a magnetic stirrer (model: SP88854100, manufacturer: Thermo Scientific) for 12 hours. Subsequently, to improve the quality of the mixture and release the trapped air inside it, the mixing process was enhanced by using a sonicator (model: Q500, manufacturer: Qsonica) for 30 minutes. The prepared mixture of the nano-PCM was solidified by lowering its temperature below the melting temperature in a second constant temperature bath. Subsequently, multiple cycles of melting and solidification process were executed and it was observed that the nano-PCM was stable and the amount of sedimentation was minimum. Then, the nano-PCM was poured into one of the enclosures at a specific height to represent a predetermined Rayleigh number.

3.2.4 Experimental procedure

The experimental work was carried out in several steps. At the beginning, for a given temperature difference (i.e., T_h-T_m), the vertical height of the PCM (H) required to achieve a pre-selected Rayleigh number was calculated by using the following equations.

$$Ra = \frac{g(\rho\beta)H^3(T_h - T_m)}{\mu\alpha} \tag{1}$$

where, ρ, β, μ, and α represent density, coefficient of thermal expansion, dynamic viscosity, and coefficient of thermal diffusivity of bio-based PCM/nano-PCM, respectively. In addition, g is the gravitational acceleration, H is the height of filled bio-based PCM/nano-PCM, T_h is the temperature of the hot bath, and T_m is the melting temperature.

Next, one of the prototype C-TES systems was filled with the liquid bio-based PCM and the second one with liquid nano-PCM at the calculated height. The bio-based PCM and nano-PCM filled prototype C-TES systems were solidified gradually and sub-cooled to 21°C using a constant

temperature bath. The temperature of the main water tank was set to T_h ($T_h > T_m$) using the temperature controller. The sub-cooled C-TES prototype was placed inside the water tank once the temperature reached to T_h . To reduce the heat loss to the surrounding, the water tank was properly insulated. During the melting process, the temperature inside the bio-based PCM and nano-PCM were monitored at 10s intervals and images were captured by the digital camera periodically to observe the melting pattern inside the C-TES systems.

3.3 Results and Discussion

In this section, selected results from the visualization experiments of pure PCM and nano-PCM are presented. For the nano-PCM, the selected weight fractions of nanoparticles ranges from 0 to 0.0311 wt. %, while the height of the PCM filled in C-TES systems is varied from 4 to 10 cm. Additionally, temperature distribution and melt fraction of the bio-based PCM and nano-PCM are presented.

3.3.1 Visualization Experiments: H =7.2 cm and wt.%=0.0156, 0.0218 and 0.0311

Figure 2 shows the time evolution of the melting process of bio-based PCM and nano-PCM inside the C-TES system when the height of the bio-based PCM and nano-PCMs is 7.2 cm representing a Rayleigh number of 8.12×10^6. Three different weight fractions of nanoparticles were considered, i.e., 0.0156 wt.%, 0.0218 wt.%, and 0.0311 wt.%, respectively. It is worth mentioning that low weight fractions are selected to ensure clear visualization of the melting pattern inside the C-TES system using nano-PCM as dispersion of CuO nanoparticles into the coconut oil makes it darker which poses difficulties during visualization, specifically, at higher weight fractions. By conducting several initial experiments using different weight fractions of CuO nanoparticles, it was identified that, tracking the melting pattern inside the C-TES system was difficult when the weight fraction was equal to or more than 0.0311 wt.%. Before each experiment, each C-TES system was kept in a water bath at constant temperature of 21°C for a prolonged period. Subsequently, this C-TES system was placed quickly inside the second bath where temperature of the water inside the second bath was previously set and maintained at pre-selected wall temperatures (i.e., 34°C for Fig. 2). The melting process was tracked from the beginning until the bio-based PCM or nano-PCM was fully melted. The solid-liquid interface appeared few minutes after placing the C-TES system inside the water bath (e.g., with the temperature of 34°C). Figure 2 shows the captured images at eight selected time intervals. At the beginning of the melting

process (180 s), conduction heat transfer dominated. Thermal energy transferred uniformly to the solid PCM and nano-PCM. A vertical thin layer of liquid PCM and nano-PCM was observed. The liquid layer took a shape of a concentric cylinder around the solid nano-PCM. However, it was difficult to differentiate the amount of melting from the visual observation at this stage. As time advanced, the thickness of the liquid layer increased in size. Motion in the liquid bio-based PCM (and nano-PCM) was established due to the onset of natural convection at the upper part of the C-TES system where the liquid layer was relatively wider than the lower part. However, at the lower part of the liquid layer conduction was still dominating as can be observed from the images at 600s. With the advancement of time, the heated liquid layer of bio-based PCM close to the walls of the C-TES system raised due to its lower density. Due to the ongoing heating, the warm liquid PCM (both bio-based PCM and nano-PCM) accumulated at the top of the C-TES systems and exhibited high temperature due to the thermal stratification effect. As a result, more deformation was observed along the interface line near the top resulting in a dome shape solid PCM (see images at 1200s). The combined domination of conduction and convection was continued as time advanced further. However, convection dominated more at the upper part with shrinking conduction dominating zone at the lower part as time advanced (see images at 1800s). Strong convection current opens a large liquid PCM (and nano-PCM) region at the top of the C-TES system as can be seen from the images at 2400 s. Additionally, the thickness of the liquid layer close to the walls of C-TES system grew from the bottom to the top due the strong convection current. Concurrently, the shrinking solid PCM region at the center of the C-TES system took a shape similar to an inverted paraboloid, which reduced to a shape similar to a cone as time advanced further (see images at 3000 s and 3300 s). At the early stages of the melting process (up to 1200 seconds), adding nanoparticles did not show significant enhancement in the melting rate. After 1200 s, comparing with bio-based PCM, nano-PCMs melted faster. Additionally, it was observed that higher nanoparticle weight fractions led to faster melting rate.

Calculating melt fraction requires accurate information on the amounts of liquid and solid forms of PCM at particular time during the melting process. Determining these amounts experimentally is a very challenging task due to the shape of the enclosure, color of the liquid and solid PCM, increasing turbidity in the liquid region due to the presence of nanoparticles, and non-uniformity in the interface region. Nevertheless, researchers have proposed different elegant methods for calculating melt fraction experimentally, these are namely volume based, surface based, and line

based calculation methods ([20], [22-24]). Each of these method has certain advantages and disadvantages. For example, Ho and Gao [20] used a volume based method to determine the amount of liquid nano-PCM. The authors quickly drained out the liquid nano-PCM at a particular time to record the liquid-solid interface. This method is extremely time consuming to have a complete melting picture, but accurate. In contrast, Fan et al. [22] used the volume expansion of the liquid PCM inside a narrow tube attached to their enclosure to calculate melt fraction during melting experiments. This indirect method has novelty when interfaces are hard to track due to the darkness of the nano-PCM. Shokouhmand and Kamkari [23] utilized the functionality of MATLAB image processing toolbox to calculate the melt fraction using the digital images from their experiments. Authors converted the color images to binary images (i.e., black pixels refer to 0 and white pixels refer to 1) after improving the contrast of the picture by filtering. This is an excellent method once one has quality 2-D images. However, pixels along the mushy zone may be a source of small error for this method. Al-Jethelah et al. [24] used a line method to track the solid-fluid interface using the magnified view of the experimentally obtained high quality 2-D images and then digitized the tracked line along the interface to coordinate data points (i.e., x, y). A numerical integration is subsequently performed on the coordinated data points to calculate the solid and liquid areas of the digital images and, subsequently, the melt fraction. This method is extended further to calculate the volume of solid nano-PCM by revolving the digitally obtained surface as authors used an axi-symmetric geometry.

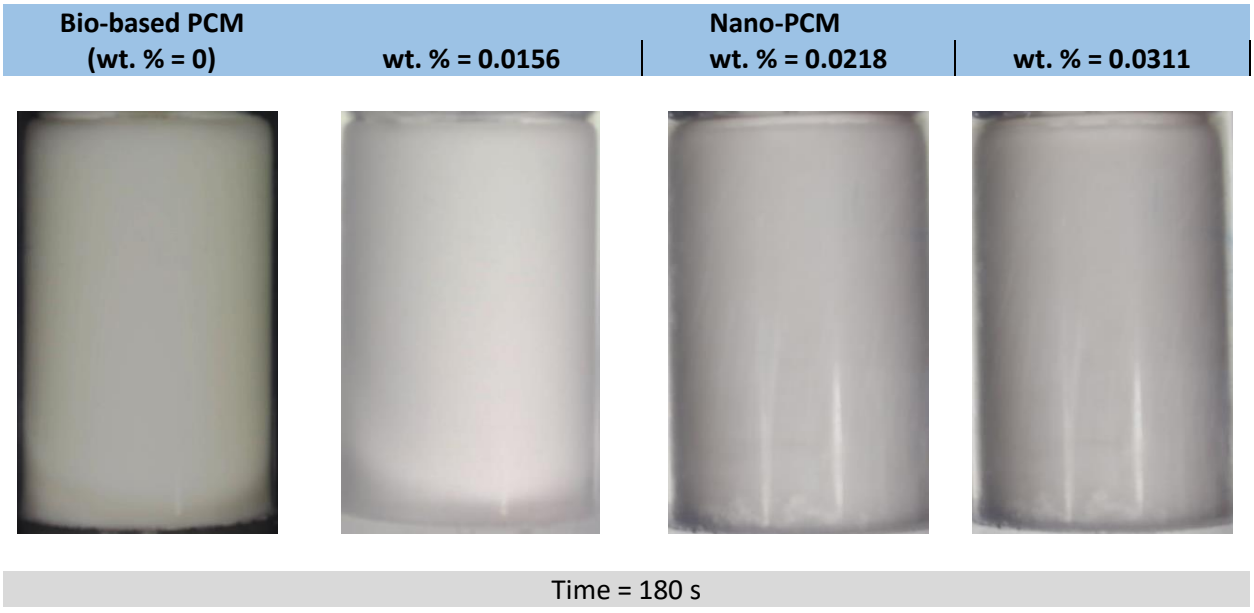

Time= 600 s

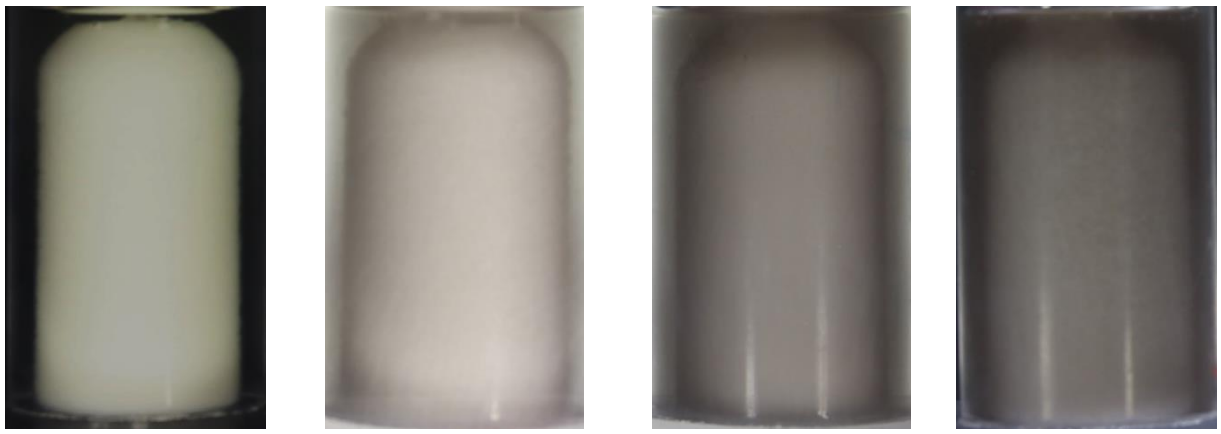

Time= 1200 s

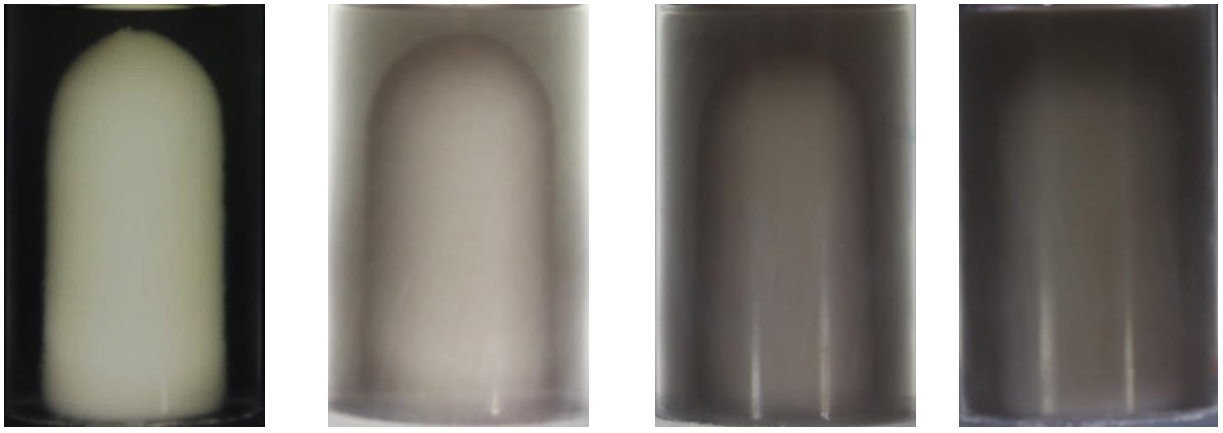

Time = 1800 s

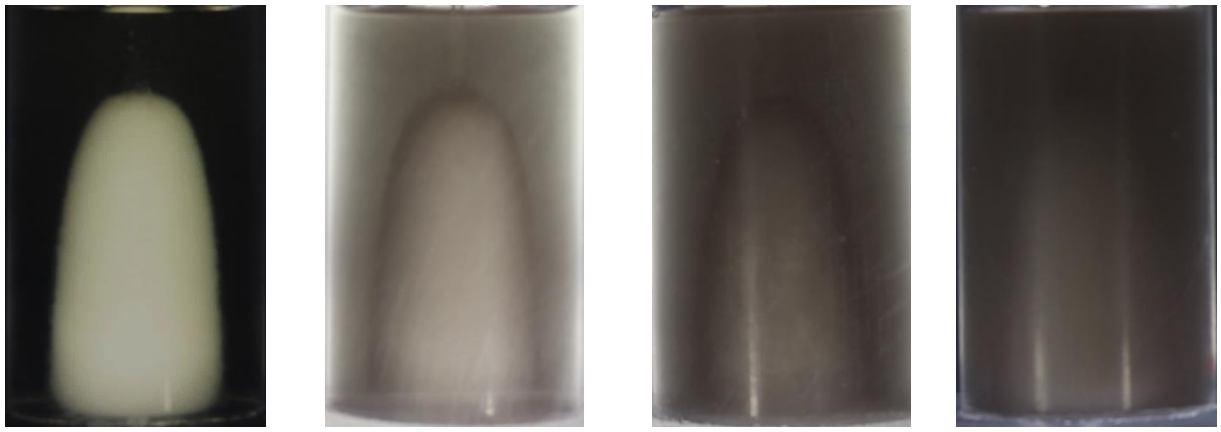

Time = 2400 s

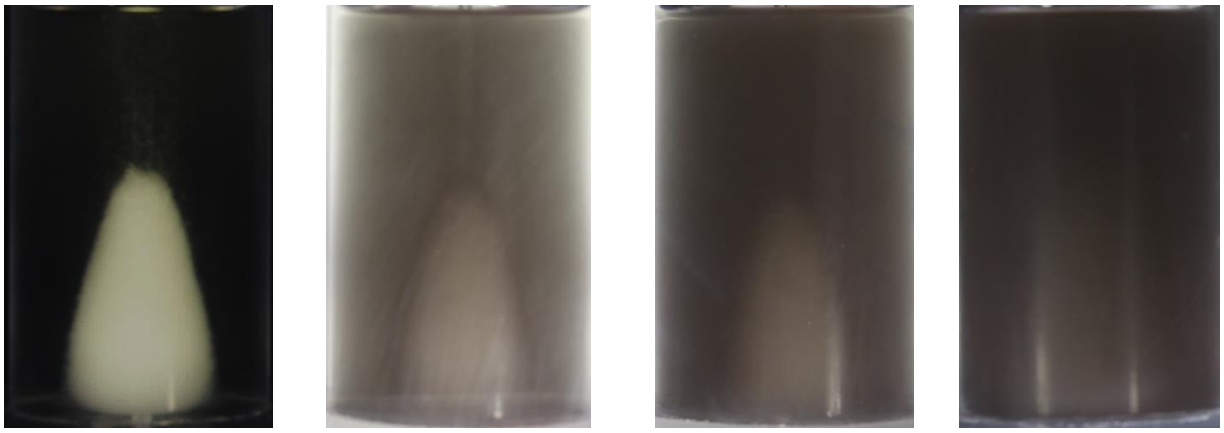

Time = 3000 s

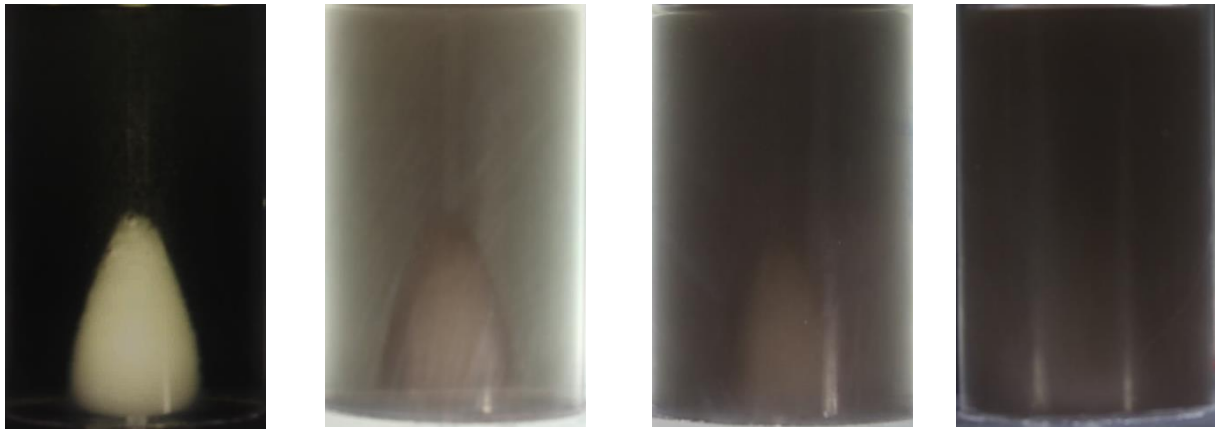

Time = 3300 s

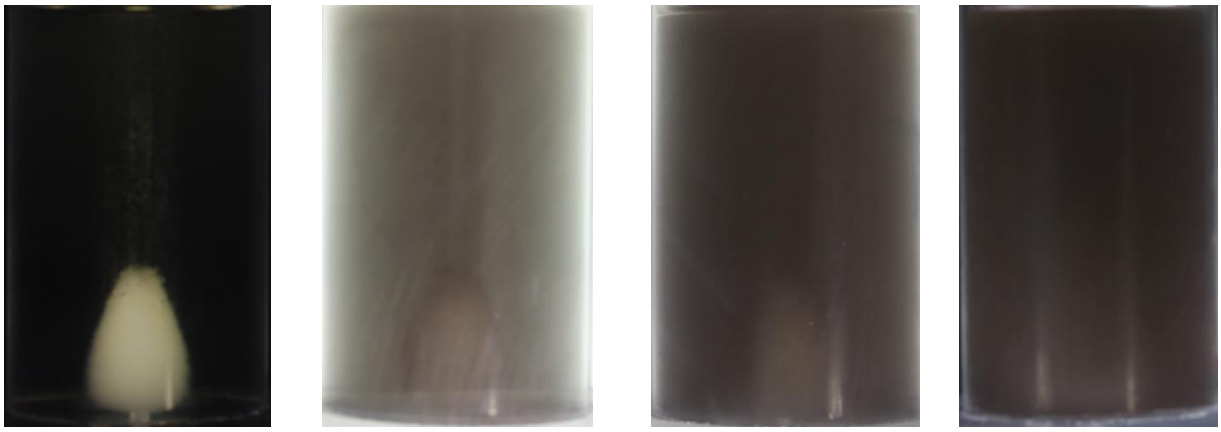

Fig.2. Visualization comparison of bio-based PCM (wt. % = 0) and different nanoparticles weight fractions (wt. % = 0.0156, 0.0218, and 0.0311), H= 7.2 cm.

Figure 3(a) presents a comparison of melt fraction between pure PCM and nano-PCMs for two different weight fractions (i.e., wt.% 0.0156 and wt.% 0.0218). To obtain the liquid melt fraction from the digital photos at different times, Grafula software was used. The melting images extracted by the digital camera were exported to the software interface. Next, the proper dimension of the C-TES system was defined in the software environment. At the next step, a curvature was fitted along the solid-liquid interface of the PCM and nano-PCM from which co-ordinates data were extracted using Grafula's digital data extraction feature. This resulted in the coordinates of each point on the curvature. Subsequently, the coordinates of each point were exported to Microsoft Excel spreadsheet for analysis and integration. From the interface coordinate data points a large number of area slices are considered and their areas and area-centers are determined. For all slices, the volumes generated due the 360^{o} revolution are calculated and integrated to achieve the volume of the solid nano-PCM and subsequently the melt fraction. See section 3.3 for discussion on the accuracy and uncertainty associated with this method.

Image processing method for calculating melt fraction was also used by other researchers in literature, for example, Tan [25] calculated melt fraction inside a spherical container using the image processing method. The melt fraction proportionally increases with time for bio-based PCM and nano-PCMs. As it can be seen at the beginning of the melting process, pure PCM and nano-PCMs behaved almost the same. However, with an ongoing heating process, nano-PCMs melt faster than pure PCM.

In order to have a better comparison of melting pattern between bio-based PCM and nano-PCM, solid-liquid interface is presented further on the x-y plots. For a given height of the PCM/nano-PCM inside the C-TES system (H=7.2cm), transient evolution of the melting interface is presented in Fig. 3(b) for wt.%=0.0218. The interface pattern associated with different regimes of melting (i.e, pure conduction, mixed convection and conduction, convection dominant and shrinking solid) is clearly visible in Fig. 3(b). Figure 3(c) shows the effect of nanoparticle loading on the interface location at a selected time of melting (i.e., t=2400sec.) and PCM/nano-PCM height (i.e., H=7.2cm) inside the C-TES system.

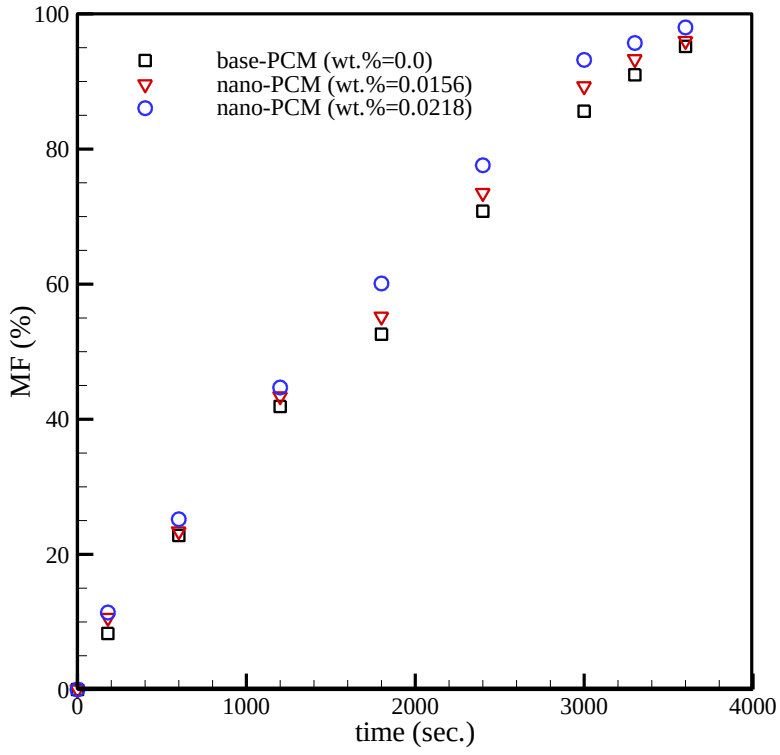

(a)

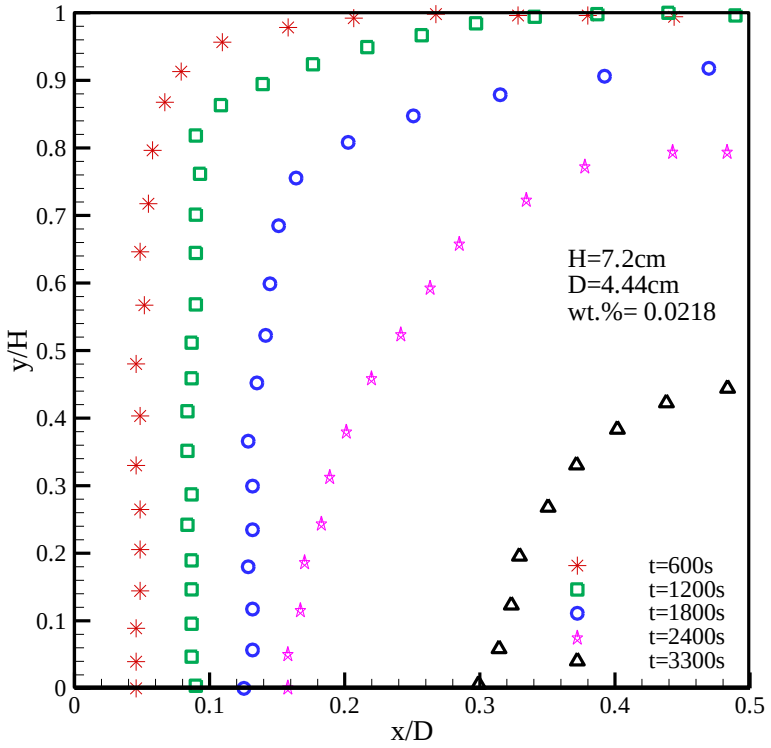
H=7.2cm
D=4.44cm
wt.%= 0.0218
t=600s
t=1200s
t=1800s
t=2400s
t=3300s
y/H
x/D

(b)

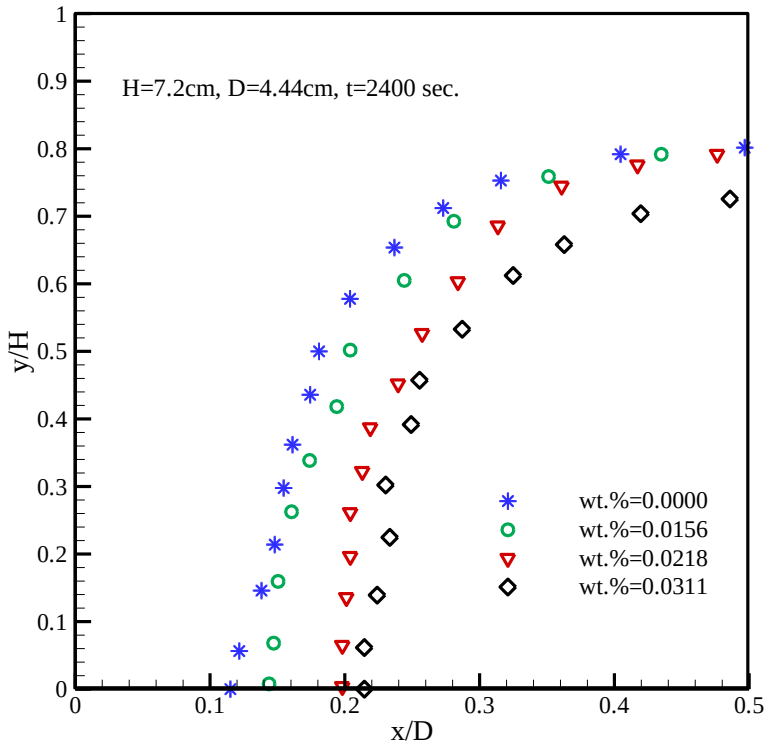
H=7.2cm, D=4.44cm, t=2400 sec.
wt.%=0.0000
wt.%=0.0156
wt.%=0.0218
wt.%=0.0311
y/H
x/D

(c)

Fig. 3: (a) Transient variation of melt fraction for base-based PCM (wt.% = 0) and nano-PCM (wt.% = 0.0156 and 0.0218) when H= 7.2 cm and T_h=34^{o}C, **(b)** solid-liquid interface profiles as a function of time for wt.%=0.0128 and H=7.2cm, and **(c)** solid-liquid interface profiles as a function of wt.% and t=2400 sec.

3.3.2 Visualization Experiments: wt.%=0.0156 and H=4 cm, 6 cm, 8 cm, and 10 cm

In another set of experiment, the effects of different heights (i.e. 4 cm, 6 cm, 8 cm, and 10 cm) of the filled nano-PCM representing the Rayleigh numbers of 1.38×10^6, 4.7×10^6, 1.11×10^7, and 2.2×10^7 inside the C-TES system were examined for 34°C wall temperature. To do so, the same procedure, as described in the previous section, was followed. As it can be seen from Fig. 4 to Fig. 7, there is a significant difference in the melting pattern occurring for different heights. For the lowest height of filled nano-PCM (i.e. H= 4 cm), the melting pattern tends to look like a dome shape. However, as the height increases, the solid part of the PCM tends to take the shape of an inverted paraboloid. Based on the shape of the solid PCM for different heights it can be concluded that the shape of the solid PCM depends on the distance between the domination of natural convection area, close to the upper part of the C-TES system, and the surface of the remaining solid PCM. Natural convection dominated at the upper part of the liquid PCM. At a height of 4 cm, the height of the liquid PCM was lower than those of higher heights (i.e. H = 6 cm to 10 cm) which made the strong convection currents closer to the solid PCM which affected the melting pattern. In addition, it was observed that increasing the height of the filled PCM, increased the melting time since more amount of PCM was used in the C-TES system. Besides, for the case of 4 cm, the difference between the remaining solid part of the bio-based PCM and nano-PCM was more significant. This can be a result of higher concentration of copper oxide nanoparticles at lower heights due to the sedimentation.

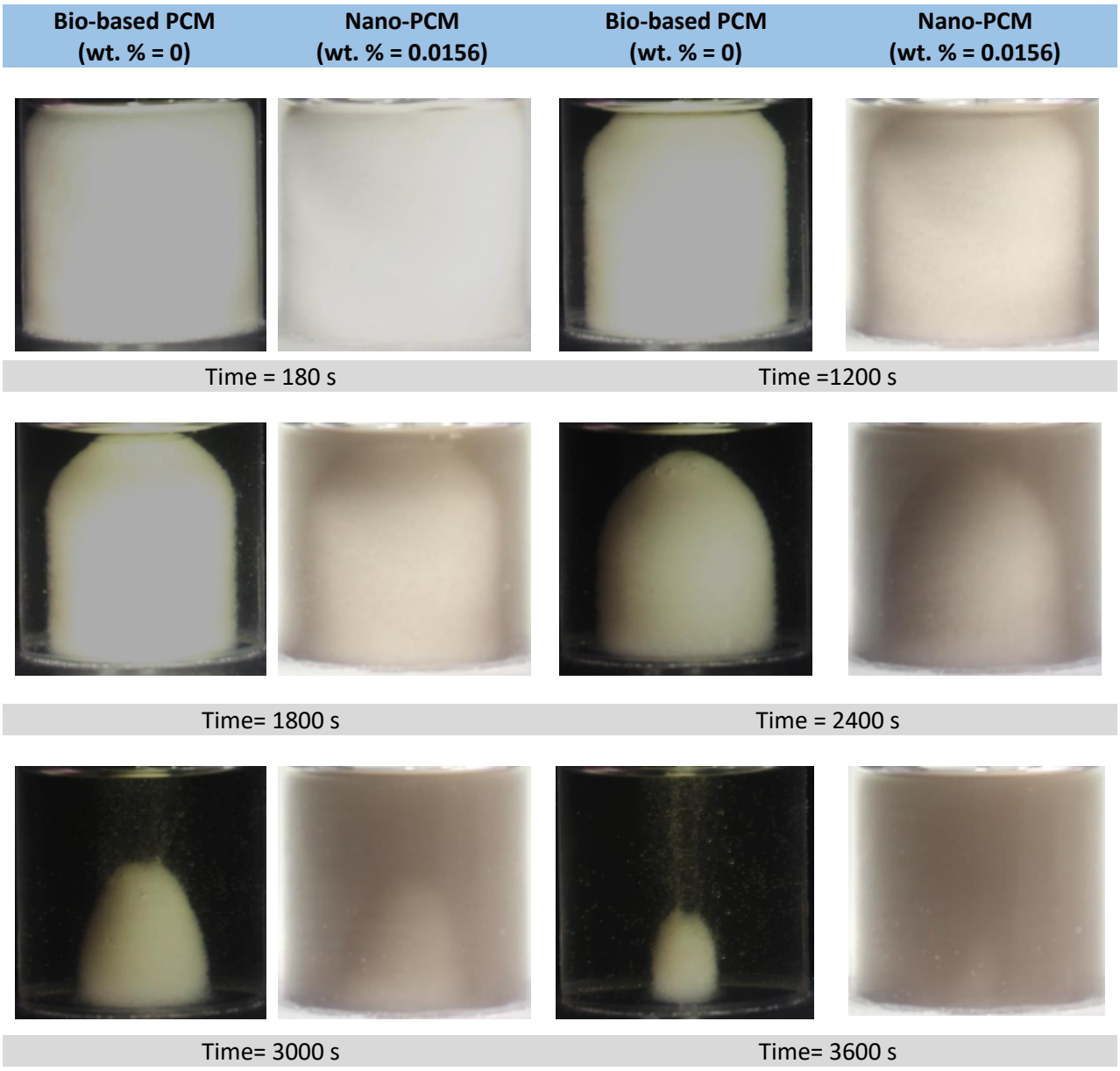

Fig.4. Visualization comparison between bio-based PCM (wt. %= 0) and 0.0156 wt. % nano-PCM, H= 4 cm.

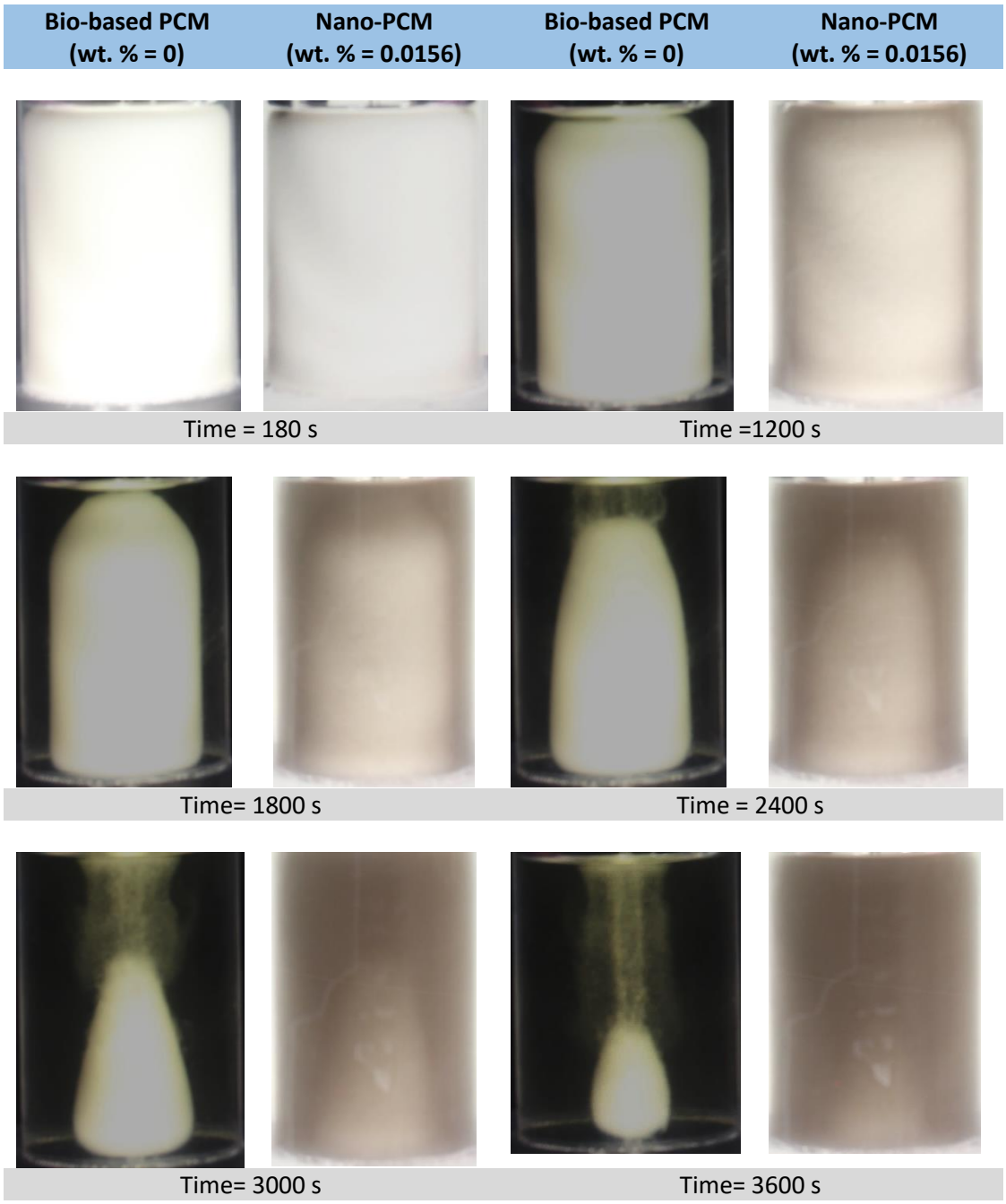

Fig.5. Visualization comparison between bio-based PCM (wt.%=0) and 0.0156 wt.% nano-PCM, H= 6 cm.

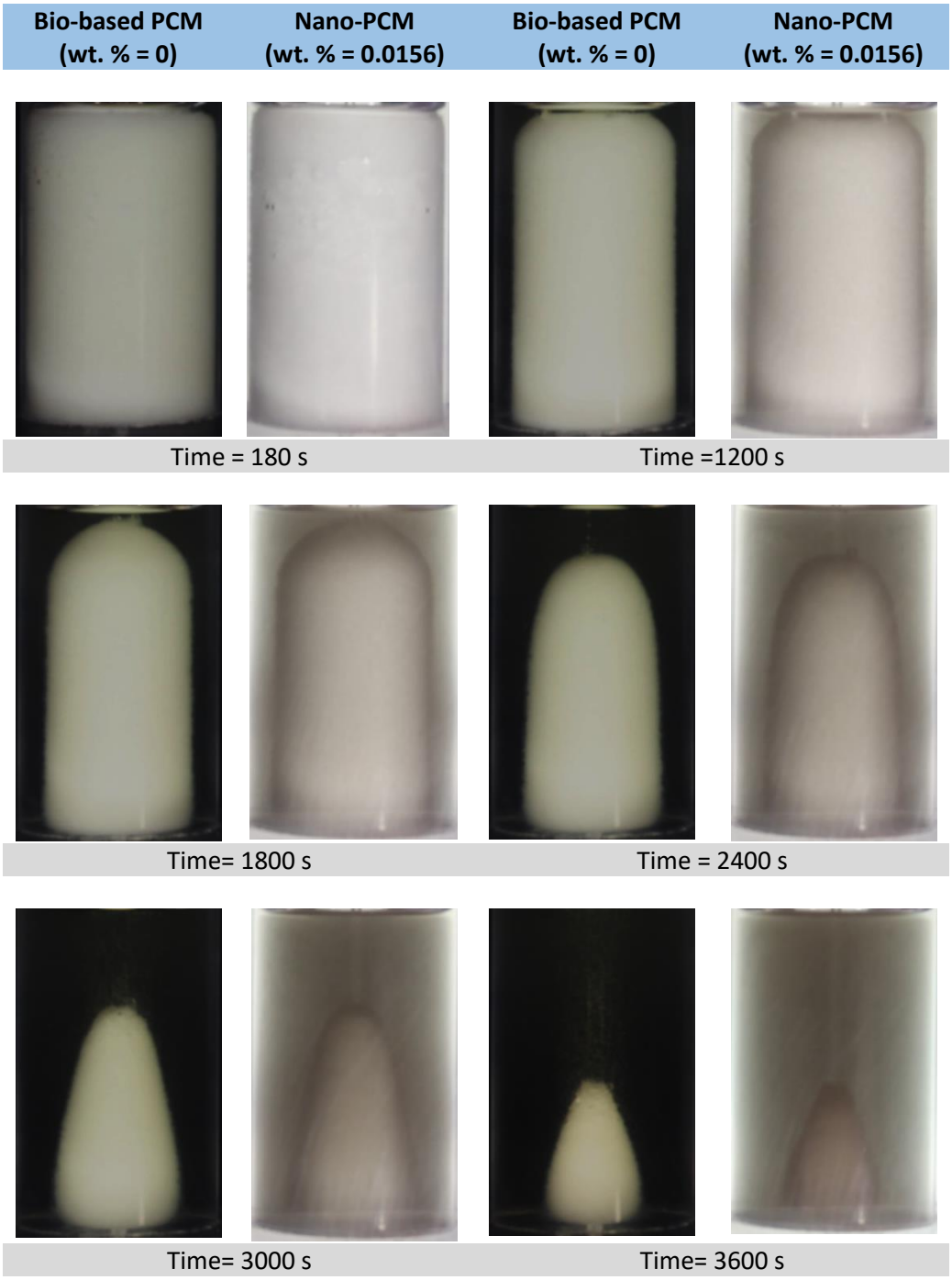

Fig.6. Visualization comparison between bio-based PCM (wt.%=0) and 0.0156 wt.% nano-PCM, H= 8 cm.

Fig.7. Visualization comparison between bio-based PCM (wt.%=0) and 0.0156 wt.% nano- PCM, H=10 cm.

Figure 8 shows the effect of the PCM height on the melt fraction (MF) of pure and nano-PCM (0.0156 wt.%). The comparison is between the PCM heights of 4 cm and 10 cm. As expected, increasing the PCM height increases its quantity, which requires more time to melt. Maximum increase in melt fraction is 15% for a wt.% =0.0218 compared to the base case (wt.% = 0).

The experiment is conducted further considering two additional hot wall temperatures (i.e., 44^{o}C and 54^{o}C). Melting images are captured at different times and some selected results are presented in Figs. 9(a) to 9(c). Rate of heat transfer increases at higher wall temperature which accelerates the melting process as can be observed from the images provided in Figs. 9(a) to 9(c).

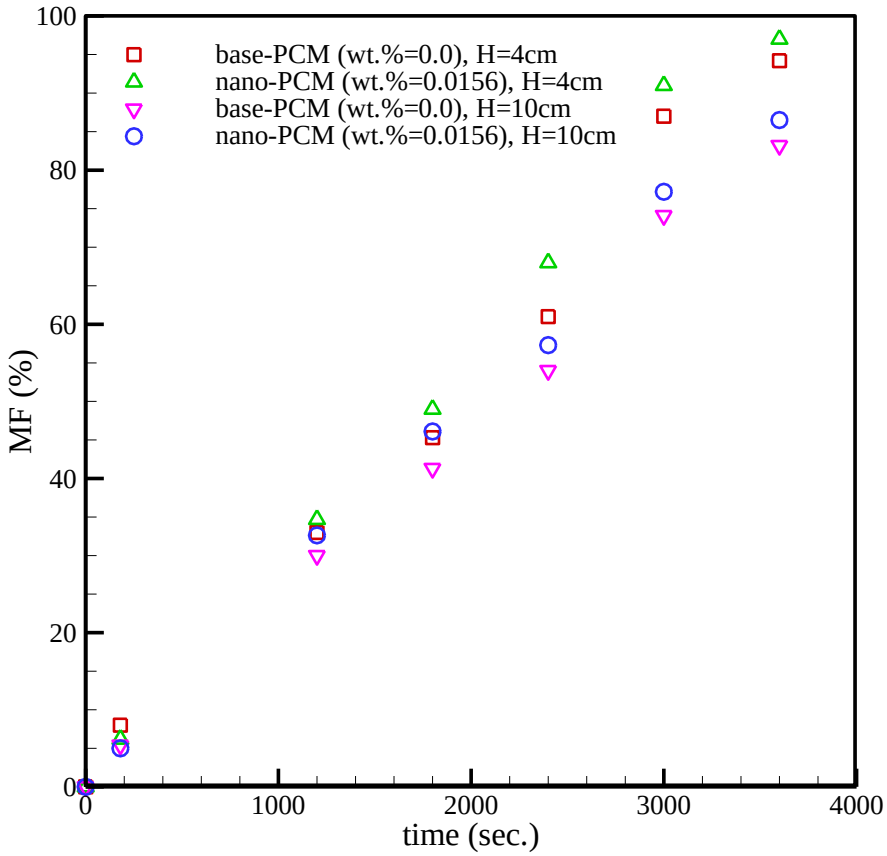

Fig. 8: Comparison of melt fraction between base-based PCM (wt.% = 0) and nano-PCM (wt.% =0.0156) for different enclosure heights (H= 4 cm and H=10 cm) and T_h=34^{o}C.

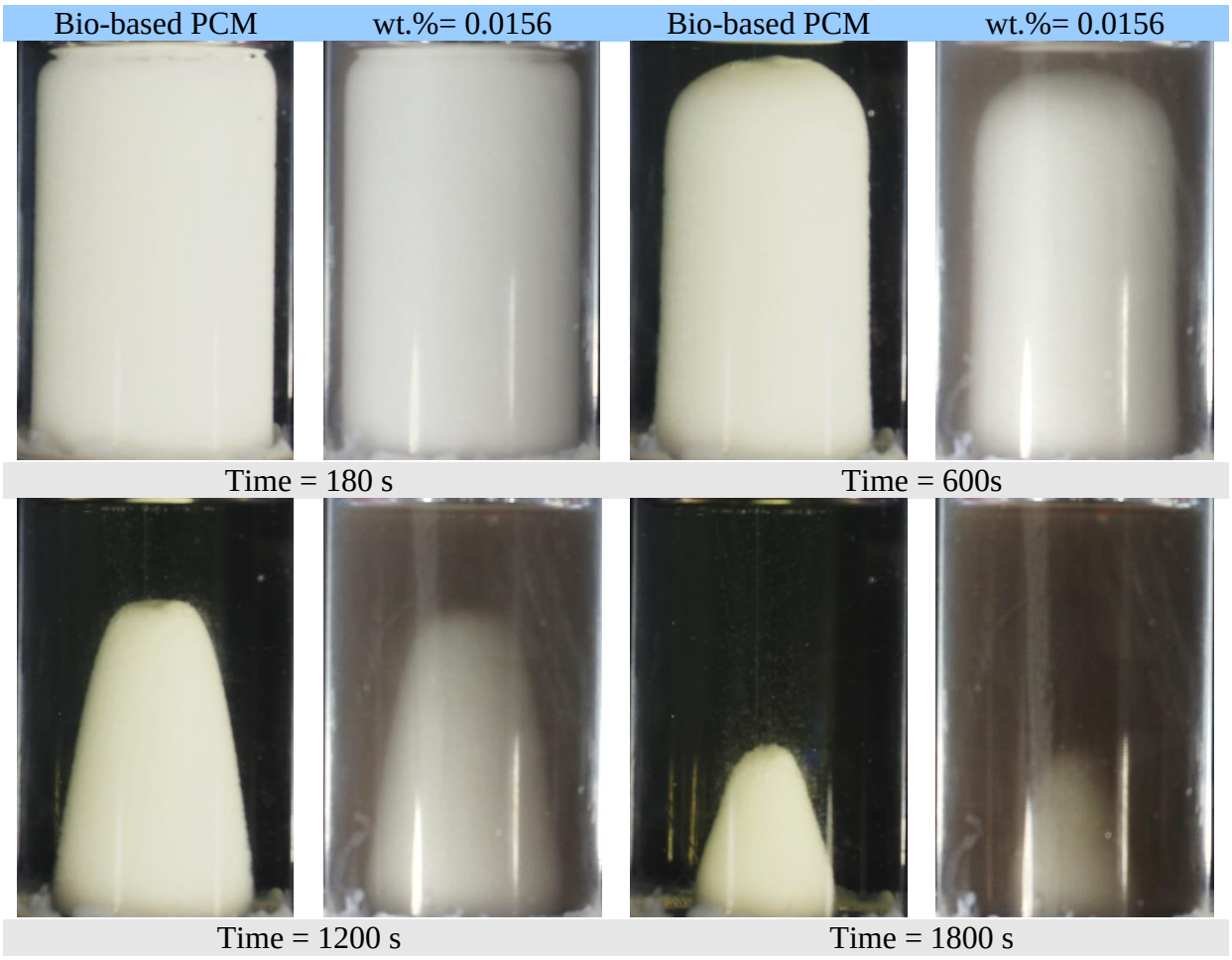

Fig. 9(a): Visualization comparison of pure bio-based PCM (wt. % = 0) and nano-PCM (wt. %= 0.0156), T_h = 44˚C and H= 7.2 cm

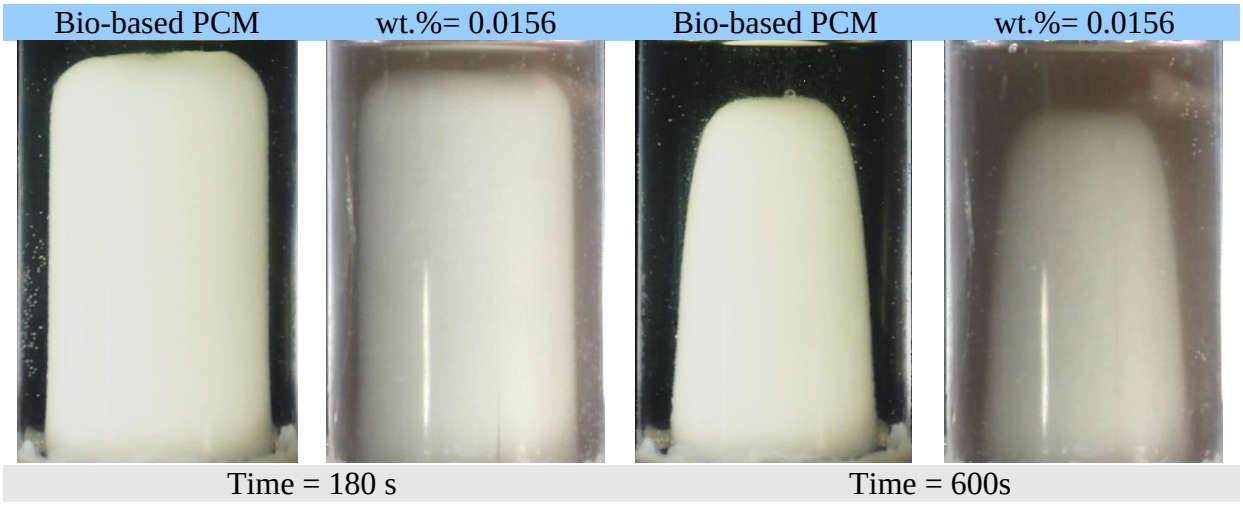

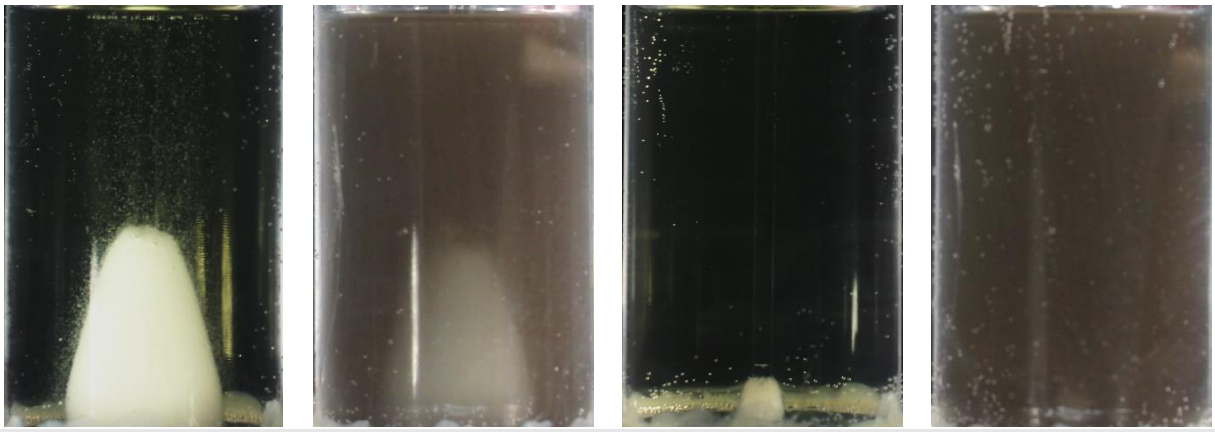

Time = 1200 s Time = 1800 s

Fig. 9(b): Visualization comparison of pure bio-based PCM (wt. % = 0) and nano-PCM (wt. %= 0.0156), T_h = 54˚C and H= 7.2 cm

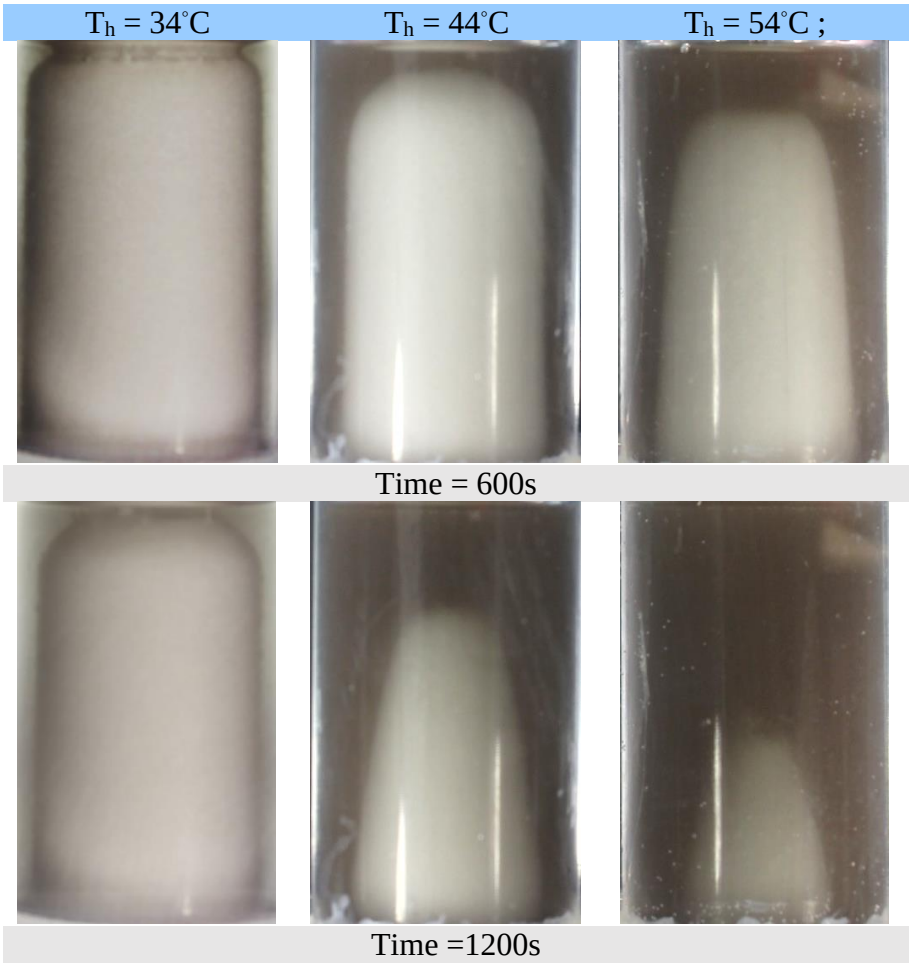

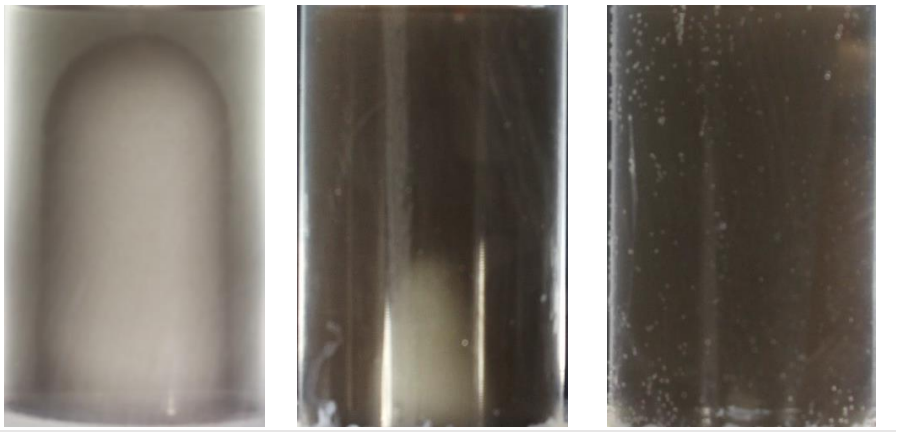

Fig. 9(c): Visualization comparison of nano-PCM(wt. % = 0.0156) at Th= 34˚C, 44˚C, and 54˚C, H= 7.2 cm.

3.3.3 Temperature measurement experiments

The transient temperature variations inside the bio-based PCM and nano-PCM are shown in Fig. 10(a) for a shorter C-TES system (i.e., H=6 cm), while the variations for the taller C-TES system (i.e., H=10 cm) are presented in Fig. 10(b). Effect of three different hot wall temperatures (i.e., 34^{o}C, 44^{o}C, and 54^{o}C) is presented as well. To obtain the temperature profiles two C-TES systems were used simultaneously during the experiment as before; one system with bio-based PCM and the second one with nano-PCM of wt.%=1.0. For each system, two T-type thermocouples were located in the center of each C-TES system at heights of 1.5 cm (T_{C1}) and 3.5 cm (T_{C2}) from the bottom of the C-TES system.

For all cases considered in Fig. 10, the initial temperature of the PCM and nano-PCM is 21˚C. Once the wall temperature is raised to a specified value (i.e., 34^{o}C), the solid phase of subcooled PCM and nano-PCM is heated up gradually through heat conduction process until the melting temperature is achieved. A lower slope in the temperature-time curve is an indication of the dominance of conduction heat transfer and the difference between the temperatures at two probe points remains fractionally small. As it can be observed, adding nanoparticles did not show significant effect on temperature variation at the conduction dominated phase. After the temperature of the PCM and nano-PCM reached to T_m, there is a significant change in the slope of curves, which is due to the onset of natural convection. Temperature increases rapidly at each probe point when the melting front as well as the natural convection thermal boundary layer moves over the probe points. Rapid slope change occurs earlier for T_{C2} as this probe point is exposed to

the melting front earlier. Effect of inclusion of nanoparticles is clearly visible at this convection dominated melting where the rapid rise in temperature at each probe points occurs at earlier time for nano-PCM than pure PCM. Adding nanoparticles to a PCM decreases the specific heat (c_p) and the latent heat of fusion (h) which reduces the sensible and latent heat capacity in the liquid PCM/nano-PCM. This results in higher temperature for the nano-PCM than that for bio-based PCM at the same time. However, according to a previous published work [25], this behavior also depends on the type of the PCM and nanoparticles. Towards the end of the melting process a second rapid slope change is observed in the temperature profiles. Each probe point temperature approaches to the wall temperature. An insignificant difference in the probe point temperatures is observed as the liquid PCM and nano-PCM nearly reach to the thermal equilibrium condition. Similar transient temperature-time profiles are observed for higher wall temperatures (i.e., 44^{o}C and 54^{o}C). The first and second drastic changes in the slope occur at earlier time when wall temperature is higher as melting front and thermal boundary layer pass earlier over the probe points at high wall temperature.

The impact of PCM height on the probe point temperature profiles are further clarified in Fig. 10(c), where transient temperature profiles are presented for H=6 cm and H=10 cm when wt.%=0.0 and 1.0. As it can be observed from Fig. 10(c), the temperature of the PCM is higher as the height of the PCM is lower for both pure PCM and nano-PCM. As the height of the PCM is lower, the quantity of the PCM is less, which requires less heat for melting. Therefore, for a given wall temperature, first and second drastic changes in the slope in the temperature profiles occur at earlier time when H=6cm. The time it takes to raise the temperature above melting point increases by approximately 113% when the temperature of constant temperature bath is 54 ^{o}C compared to 34 ^{o}C and the height of the PCM is 6 cm for wt.% =1. The time it takes to raise the temperature above melting point increases by 20% for a nano-PCM height of 10 cm compared to that of 6 cm for wt.% = 1. Higher wt. % of nanoparticles enhanced the rate of melting.

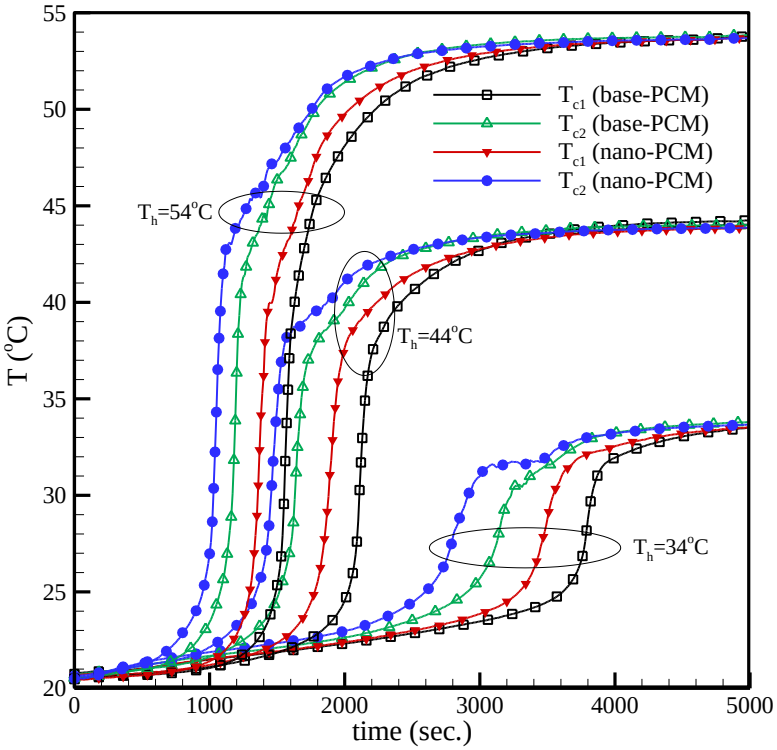
T (°C)
time (sec.)
T_c1 (base-PCM)
T_c2 (base-PCM)
T_c1 (nano-PCM)
T_c2 (nano-PCM)
T_h=54°C
T_h=44°C
T_h=34°C

(a)

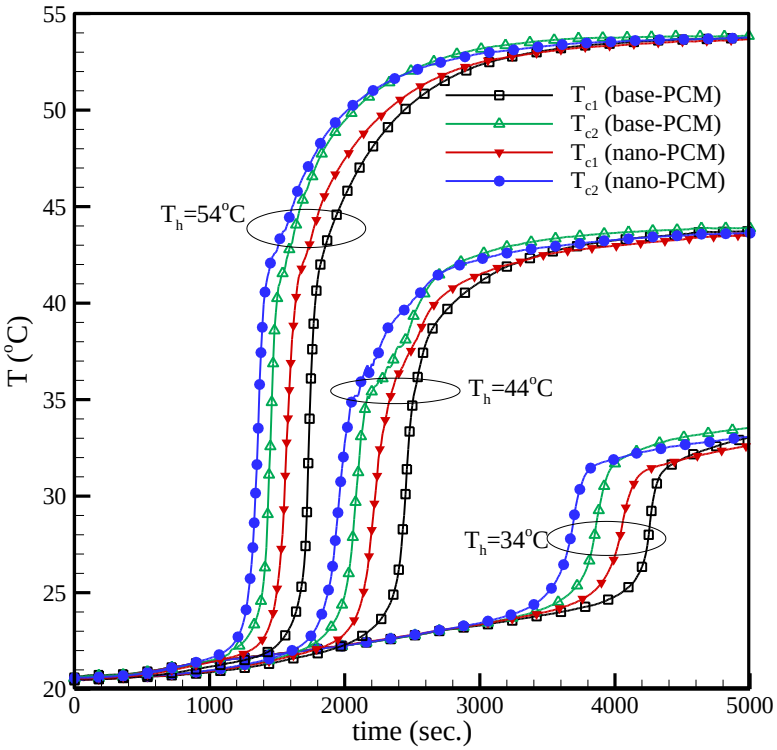
T (°C)
time (sec.)
T_c1 (base-PCM)
T_c2 (base-PCM)
T_c1 (nano-PCM)
T_c2 (nano-PCM)
T_h=54°C
T_h=44°C
T_h=34°C

(b)

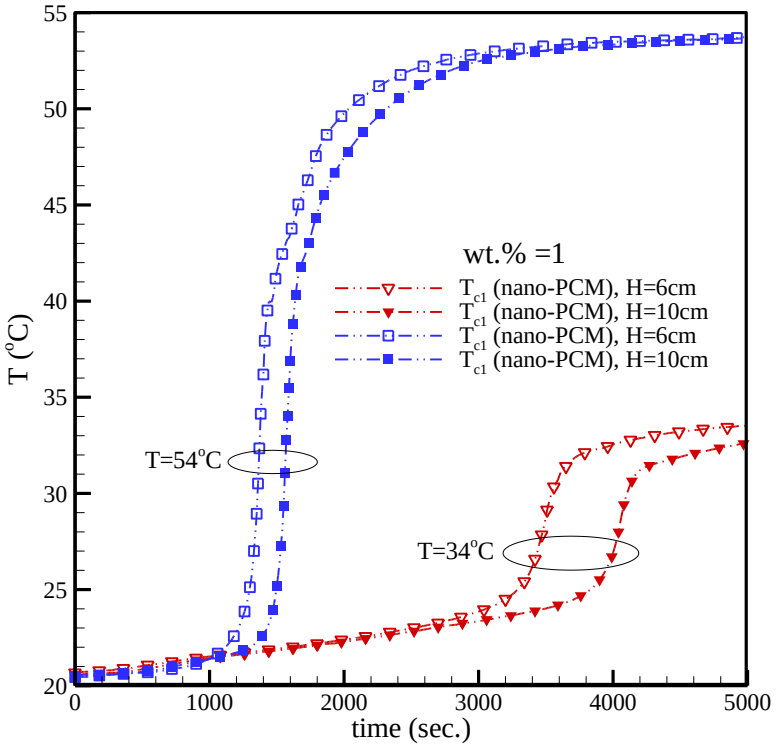

(c)

Fig. 10: Comparison of temperature profiles between bio-based PCM (wt.% =0) and nano-PCM (wt.% =1) at three different hot wall temperatures (T_h=34°C, 44°C, and 54°C) and two heights (H= 6 cm and10 cm) of the enclosure (the thermocouple locations, T_{c1} and T_{c2}, are 1.5cm and 3.5cm from the bottom)

3.3.4 Uncertainty analysis of experimental results

In this section, an uncertainty analysis is performed to evaluate the accuracy of the results. This uncertainty is consisted of accuracy of the temperature measurement devices (i.e. thermocouples and DAQ system) and accuracy of the method used for calculating melting fraction from the digital photos.

The absolute measurement uncertainty (i.e., the accuracy) values for T-type thermocouples, DAQ system, and thermal regulator are ±1°C ($=\delta T_{TC}$), ±0.02°C ($=\delta T_{DQ}$), and ±0.01°C ($=\delta T_{RG}$), respectively, where any quantity with the symbol δ represents the absolute measurement uncertainty. These values are provided by the manufacturers/suppliers of the equipment/sensors. The relative uncertainty of a measured quantity is estimated based on the propagation of

uncertainty [22]. For example, the relative uncertainty associated with the nano-PCM temperature measurement inside the enclosure can be given by

$$\frac{\delta T_c}{T_c} = \sqrt{\left(\frac{\delta T_{TC}}{T_{TC}}\right)^2 + \left(\frac{\delta T_{DQ}}{T_{DQ}}\right)^2} \quad . \tag{2}$$

For measured values of nano-PCM temperature of 21ºC and 54ºC, the corresponding relative uncertainties are ±4.76% and ±1.85%, respectively. Similarly, the relative uncertainty associated with the hot wall temperature measurement can be given by

$$\frac{\delta T_h}{T_h} = \sqrt{\left(\frac{\delta T_{RG}}{T_{RG}}\right)^2} \quad . \tag{3}$$

For measured values of hot wall temperatures of 34ºC and 54ºC, the corresponding relative uncertainties are ±0.03% and ±0.02%, respectively. Similarly, following equation can be used to determine the relative uncertainty for total volume of the nano-PCM

$$\frac{\delta V}{V} = \sqrt{\left(\frac{\delta H}{H}\right)^2 + \left(2\frac{\delta D}{D}\right)^2} \tag{4}$$

where $\delta H = \delta D = \pm 0.1$mm. For H=7.2cm and D=4.44cm the corresponding relative uncertainty for measuring total volume is ±0.47%.

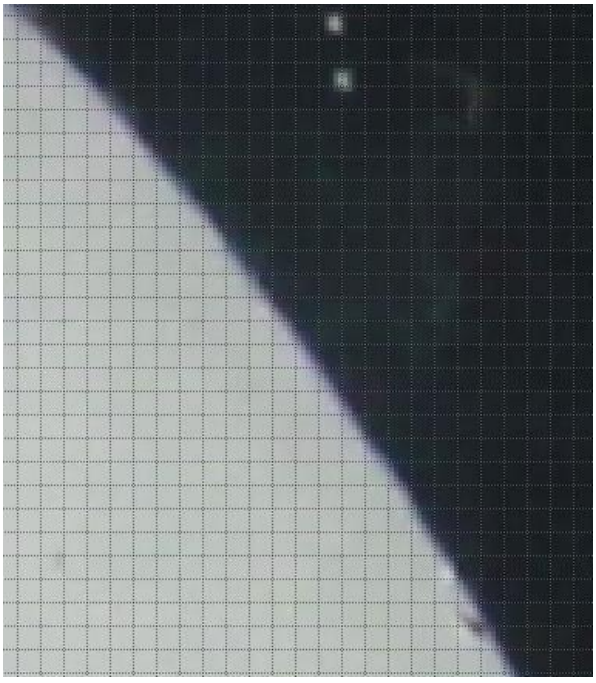

Figure 11: Magnified view of a portion of the solid and liquid nano-PCM inside a pixel grid system

As discussed earlier a line based method [24] is used in this paper to calculate the melt fraction. High resolution images (i.e. 5187×3456 pixels) are taken by digital camera and processed them further for melt fraction calculation. A line based method is used to track the solid-fluid interface of the digital images to get the coordinate data points (i.e., x, y). From the interface coordinate data points a large number of area slices, extended vertically upward, are calculated and their area centers are determined. For all slices, the volumes generated due the 360^o revolution are calculated and added to achieve the volume of the solid nano-PCM. For this method, identifying the exact interface location is a very important step which is a source error for the co-ordinate data points. To elaborate the discussion further, a magnified view of a portion of the image taken during the experiment is shown in Fig. 11 where areas covered by both solid and liquid nano-PCM are captured inside a pixel grid system. A MATLAB image processing [23] can capture solid areas (brighter pixels) and liquid areas (darker pixels). However, the main uncertainty of image processing based calculation comes from the pixels representing the solid/liquid interface due to their partial darkness and partial brightness. This uncertainty will be more for the case of higher volume fraction of nanoparticles. A closer look at the interface reveals that the mushy zone does not extend more than 1 to 2 pixels and it remains within the 5-pixel grid block. Therefore, tracking interface with at least 1-pixel accuracy will give relatively accurate information on the interface location and subsequently the coordinate data points. For calculating the uncertainty associated with this method, the entire domain is initially divided into multiple sub-domains. In each domain, the average distance (in pixel) is calculated from the symmetry line to the interface. A line integration is performed to identify the area occupied by solid nano-PCM and then the average interface distance in pixel unit. Subsequently, following equation is used to calculate the relative uncertainty associated with the calculation of interface distance and co-ordinates:

$$\left(\frac{\delta x}{x},\frac{\delta y}{y}\right)=\sqrt{\left(\frac{\delta N_{PX}}{N_{PX}}\right)^2}\ . \tag{5}$$

where δN_{PX} represents absolute measurement uncertainty at the interface in pixels. For example, when the average distances (in pixels), calculated from the symmetry line to the interface, is N_{PX}=92 for the case shown in the Fig. 11, the corresponding value of $\delta x/x$ (or $\delta y/y$) is ±1.08% for δN_{PX}=1, ±2.17% for δN_{PX}=2, and ±3.25% for δN_{PX}=3. Now, the relative uncertainty associated with the melt fraction calculation can be obtained from:

$$\frac{\delta MF}{MF} = \sqrt{\left(\frac{\delta x}{x}\right)^2 + \left(\frac{\delta y}{y}\right)^2 + \left(\frac{\delta \bar{x}}{\bar{x}}\right)^2 + \left(\frac{\delta V}{V}\right)^2}\,. \quad (6)$$

The corresponding value of $\delta MF / MF$ is ±1.93% for δN_{PX} =1, ±3.78% for δN_{PX} =2, and ±5.64% for δN_{PX} =3. The relative uncertainty associated with the melt fraction calculation is higher towards the end of the melting process and the maximum value reaches to ±6.7%.

3.4 Conclusion

The present study experimentally investigated the melting of a bio-based nano-PCM (i.e., copper oxide nanoparticles dispersed into coconut oil) in a vertical C-TES system with an aim to examine the effects of height of PCM, hot wall temperature, and loading of nanoparticles. The C-TES system was insulated from the bottom and isothermally heated from its sides. From the obtained results, the following conclusions can be drawn:

- The bio-based nano-PCM was prepared using magnetic stirring and sonication methods and its thermophysical properties were measured. Specific heat values of nano-PCM are decreased by 0.45% and 0.75%, compared to the base case for wt.%=0.1 and 1, respectively. Thermal conductivity values of nano-PCM are increased by 4.8% and 7.5% compared to the base PCM for wt.%=0.1 and 1, respectively. Latent heat of fusion values of nano-PCM are decreased by 1.94% and 8.25% compared to the base PCM for wt.%=0.1 and 1, respectively.
- The mode of heat transfer significantly affects the shape of remaining solid PCM during melting. At the early stages, due to the dominance of conduction, the remaining solid PCM looked like a concentric cylinder. However, as the melting process evolved, the remaining PCM looked like the shape of a dome and inverted paraboloid. Moreover, the melting pattern was greatly depended on the height of filled PCM, which for lower heights tended to be dome-shaped and for higher heights to be inverted paraboloid-shape.
- The time requires to raise the temperature above melting point increases by 20% for a nano-PCM height of 10 cm compared to that of 6 cm for wt.% = 1.
- Higher wt. % of nanoparticles enhanced the rate of melting. Maximum increase in melt fraction is 15% for a wt.% =0.0218 compared to the base case (wt.% = 0).

- The time requires to raise the temperature above melting point increases by approximately 113% when the temperature of constant temperature bath is 54 ^{o}C compared to 34 ^{o}C and the height of the nano-PCM is 6 cm for wt.% =1.
- Image processing of photographs along with numerical integration is used to calculate melt fraction. To facilitate a better comparison of melting pattern between bio-based PCM and nano-PCM, solid-liquid interface is presented on the XY plots. An extensive analysis was reported as well to show how to calculate the uncertainty associated with image based melt fraction calculation. The relative uncertainty associated with the melt fraction calculation is higher towards the end of the melting process and the maximum value reaches to ±6.7%.

3.5 Nomenclature

c_p specific heat at constant pressure [kJ/kg K]

D inner diameter of C-TES system [cm]

g gravitational acceleration [m/s^2]

h latent heat of fusion [kJ/kg]

H_0 height of the C-TES system [cm]

H height of the filled PCM in C-TES system [cm]

k thermal conductivity [W/m.K]

N_{PX} number of pixel in a particular direction

T temperature [˚C]

T_{C1} final temperature measurement at thermocouple location #1 [˚C]

Tc_2 final temperature measurement at thermocouple location #2 [˚C]

T_{DQ} temperature measured by DAQ system [˚C]

T_h hot wall temperature [˚C]

T_m melting temperature of PCM [˚C]

T_{TC} temperature measured by thermocouple [˚C]

T_{RG} temperature measured by thermal regulator [˚C]

V volume of the PCM/nano-PCM [m^3]

wt.% percentage of nanoparticles volume fraction

Greek symbols

α coefficient of thermal diffusivity [m^2/s]

β coefficient of thermal expansion [1/K]

δT_{TC} accuracy of thermocouple [°C]

δT_{DQ} accuracy of DAQ system [°C]

δT_{RG} accuracy of thermal regulator [°C]

δH accuracy of height gage [mm]

δD accuracy of digital caliper [mm]

δx accuracy of the interface location in the x-direction [pixel]

δy accuracy of the interface location in the y-direction [pixel]

$\delta \bar{x}$ accuracy of the area center in the x-direction [pixel]

μ dynamic viscosity [Pa.s]

ρ density [kg/m^3]

Subscripts

h hot

m melt

Abbreviation

C-TES cylindrical thermal energy storage

DAQ data acquisition

LHTES latent heat thermal energy storage system

MF melt fraction

PCM phase change material

Ra Rayleigh number

RSS Root sum squared

RT Rubitherm

SHTES sensible heat thermal energy storage system

TCES thermo-chemical thermal energy storage system

TES thermal energy storage

Chapter 4-I

Part I: An Experimental and Numerical Investigation On Vertical Cylindrical Thermal Energy Storage System : Pure RT-35 as the PCM

"A version of this part has been submitted to the Journal of Openphysics: Soroush Ebadi, Manar Al-Jethelah, Syeda Tasnim, Shohel Mahmud, "An Experimental and Numerical Investigation On Vertical Cylindrical Thermal Energy Storage System ," Journal of Openphysics (Degruyter) 2017 OPENPHYS-D-17-00113."

4-I.1 Introduction

Nowadays, increase in energy consumption due to growth of population and development of industries, environmental concerns due to global warming and depletion of fossil fuel sources and gradual increase of the price of fossil fuels are the main dilemmas regarding energy supply. These economic and technical concerns have enforced energy providers and researchers to look for an affordable solution for this issue. Storing energy in an efficient way can play a significant role to reduce the level of greenhouse gas emissions by burning fossil fuels. Thermal energy storage (TES) systems are developed with the aim of storing thermal energy by heating or cooling a medium. TES systems can be used in many different applications for heating/ cooling purposes including HVAC systems, solar power plants for storing thermal energy during the day and release it during the night and residential buildings for waste heat recovery and use of thermal energy for heating purposes. In terms of storing thermal energy, TES systems are divided into three groups including (i) sensible heat thermal energy storage system (SHTES) system (ii) latent heat thermal energy storage system (LHTES) system and (iii) thermo-chemical heat storage system. However, LHTES system is more attractive due to the higher density of thermal energy storage and low variation in operating temperature (i.e. isothermal condition) [1]. LHTES system is based on heating or cooling a PCM where the thermal energy is absorbed as a latent heat due to the melting process and is released due to solidification process. According to the operation temperature of TES system, a PCM with proper melting temperature should be used. However, thermal conductivity, stability and the amount of latent heat (h) are the other characteristics of selecting a proper PCM [2]. In addition, according to the application of a TES system and the available space for installing this system, different types of geometries such as rectangular, cylindrical and

spherical have been used. However, the present work deals with cylindrical TES system which can be installed both horizontally and vertically. By surveying the literature, it can be found that many researchers have investigated on cylindrical TES system both numerically and experimentally. Starting with vertical cylindrical TES system configuration, a numerical investigation on natural convection through a cylindrical capsule filled with a PCM is conducted by Wu and Lacroix [3] In their investigation, the capsule is isothermally heated from the bottom, top, and sides. The stream function, vorticity, and temperature are considered in the governing equations and a method called Body-fitted coordinates is used to track the irregular shape of solid-liquid phase front. It is reported that conduction is the dominant form of the heat transfer when it is heated from the top. In addition, as the melting process progresses, Nusselt number at the top surface decreases to zero which shows that conduction is dominated during the melting process. Moreover, the bottom surface had the highest rate of heat transfer where the Benard convective cells are dominated. Also, in comparison to the case where only it was heated from the bottom, the onset of the Benard convection developed at an earlier time. Jones et al. [4] experimentally and numerically studied the melting process of a subcooled paraffin wax. The vertical cylindrical enclosure was isothermally heated from its sides using a hot constant temperature bath, insulated at the top and a constant temperature condition was applied to the bottom. During the experiments, measurement of temperatures in different radial locations and capturing the melt front locations are performed. By using digital image processing technique, a method for estimating the location of the solid-liquid interface is developed. The numerical model used enthalpy method and had a good agreement with experimental results for a specific range of Stefan numbers (i.e. Ste up to 0.1807). It is shown that during the melting process pure conduction, mixed convection and conduction, convection and shrinking solid are the main regimes. A numerical investigation of the melting process of RT-27 was conducted by Shmueli et al. [5]. In their investigation, the cylindrical model is heated isothermally from its sides, insulated from the bottom and kept open from the top. The model was based on the enthalpy-porosity formulation and the effects of a parameter representing mushy zone and pressure-velocity are considered. Moreover, quantitative information representing the rate of heat transfer and melt fractions was achieved by using image processing of previous experimental work and results are compared. It is concluded that conduction is the main form of heat transfer at the starting of melting process. As time progresses, natural convection becomes the dominant form of heat transfer which changes the solid shape to a conical one. Wang et al. [6]

conducted a numerical investigation on the melting process of a PCM with the aim of developing heat transfer correlations. In this study, inward and outward melting process inside a vertical cylindrical enclosure was considered and the model was compared to the previous works. A general agreement is achieved; however, there is some discrepancy due to the influence of heat losses. Transient heat transfer correlations and total stored energy for a variety of Rayleigh numbers and based on the outward case are proposed.

Regarding horizontal cylindrical TES system, many published works are also available in the literature. Regin et al. [7] performed a numerical and experimental study of the melting of a PCM inside a solar TES system. In their work, horizontal pipes were filled with paraffin wax and subjected to hot water from the surrounding. A numerical model based on enthalpy method is developed and results are compared to experimental investigation. It is reported that Stefan number, radius of the pipe, and range of the phase change temperature are the main dominant parameters, which control the melting process. In addition, by considering the phase change temperature and natural convection in the liquid phase the discrepancy between numerical and experimental work is improved. A numerical investigation on solid-liquid phase change for a horizontal cylindrical enclosure was carried out by Mahdaoui et al. [8]. In their work, constant wall temperature and constant heat flux were two main boundary conditions that are investigated. In order to solve the natural convection coupled to change in phase, a numerical code based on finite element and enthalpy porosity method are used and the results are validated by comparing with previous works. It is reported that at the beginning of melting, conduction is the dominant form of heat transfer and the local Nusselt number is degraded with the time. However, as melting process progresses, natural convection develops and effects the shape of the solid and the liquid parts and the Nusselt number becomes non-uniform. Hosseini et al. [9] conducted an experimental and numerical investigation to study the heat transfer and thermal behaviour of a PCM during constrained condition filled in a shell and tube heat exchanger. In this work, Paraffin RT-50 is used as a PCM and several experiments are performed to consider the influence of the inlet temperature of working fluid on melting/solidification process. A numerical part based on an iteration and finite-volume method is developed to study the variation of the molten front with time. Their results showed that rate of heat transfer and charging (melting) time depend on the inlet temperature of working fluid where by increasing the inlet temperature from 70 °C to 80 °C the

melting time is degraded to 37%. Moreover, there was a 7.3% increase in theoretical efficiency of the heat exchanger for the melting process.

According to the literature, the melting process of PCM inside an isothermal vertical cylinder insulated from bottom and opened from top has not been extensively investigated both experimentally and numerically. In this work, an experimental and numerical study is performed to investigate the melting process of RT-35 as a PCM filled a vertical cylindrical. TES system side wall is subjected to an isothermal bath, while the bottom's wall is insulated, and the top is kept opened. To perform the study, an experimental setup and COMSOL model were built to visualize and study the melting process of PCM. This work represents an early stage to study the potential improvements in the melting process by adding nanoparticles into pure PCM.

4-I.2 Problem Description

4-I.2.1 Experimental work

In this section, a detail description regarding vertical cylindrical TES system setup and experimental procedure is presented. To visualize the melting process of RT-35 as a PCM, a vertical cylindrical TES prototype is built. This setup is consisted of an acrylic pipe with an inner diameter of 4.4 cm and the height of 30 cm attached to a plate vertically by using a transparent acrylic cement (manufacturer: Scigrip). The bottom part of the enclosure is insulated while it is maintained open from the top to avoid any pressure build on the top of the PCM during the melting process. Then, the cylindrical enclosure is filled with RT-35 (manufacturer: Rubitherm) with the melting temperature (T_m) in the range of 34 -36 °C at a specific height (H) in the TES system which represents Rayleigh number (Ra) of 10^7 (i.e. the height of the PCM in the TES system is 8.3 cm). Then, the setup was kept in room temperature (i.e., $T_0 = 23°$ C) to initiate the solidification process gradually. Solidification in temperatures close to T_m and at a longer time provides the advantage of less trapped air effect, which leads to having fewer holes inside solid part that happens due to the shrinkage of PCM. This offers a more uniform solid part shape during melting process and leads to have a fair comparison with numerical results. Next, a transparent water tank equipped with a circulation pump, heater and temperature regulator were used to provide isothermal boundary condition around the sides of the TES system. Temperature of the water inside the tank is set to 45 ° C and suddenly the cylindrical TES system is placed inside the hot

bath to initiate the melting process. Moreover, a digital camera is used to capture images periodically. A schematic of the experimental setup can be seen in Figure 1.

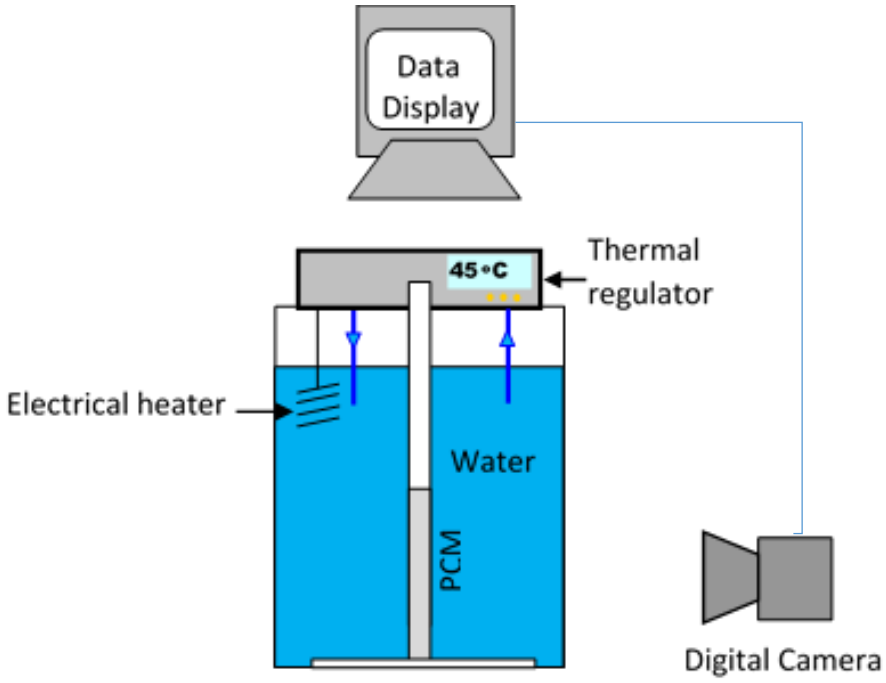

Fig.1. A schematic of the experimental setup

4-I.2.2 Numerical model

To investigate on the flow and thermal fields, a numerical model based on finite element approach using COMSOL Multi-physics software was developed. To do so, a 3-D axisymmetric model representing the cylindrical TES system having the same dimensions of experimental TES system (i.e. inner diameter of the pipe 4.4 cm and the height of 30 cm) was built. The model was insulated from the bottom and kept open from the top and it was assumed to be filled with RT-35 at a height of H to replicate the experimental conditions. The initial temperature of PCM was assumed as T_0 ,which was equal to room temperature and lower than melting temperature T_m. The model was isothermally heated from the sides at a temperature of T_h which was 10 ° C above the melting temperature to initiate the melting process. As melting process progresses, the liquid-solid interface can be seen. In this simulation, the liquid phase of PCM was considered as Newtonian

incompressible fluid. In addition, all the thermo-physical properties of RT-35 was collected from the literature [10, 11].

The principal equations representing the conservation of mass, momentum and transferred energy are presented below.

$$\text{Continuity equation: } \frac{\partial u}{\partial r}+\frac{u}{r}+\frac{\partial w}{\partial z}=0 \quad (1)$$

where *u* and *w* are the components of velocity in r-direction and z- direction, respectively.

$$\text{Energy equation : } \frac{\partial T}{\partial t}+u\frac{\partial T}{\partial r}+w\frac{\partial T}{\partial z}=\frac{k}{\rho C_p}\left[\frac{1}{r}\frac{\partial}{\partial r}\left(r\frac{\partial T}{\partial r}\right)+\frac{\partial^2 T}{\partial z^2}\right], \quad (2)$$

where *t, K,ρ* and C_p represent time, thermal conductivity, density and specific heat at constant pressure, respectively.

z-momentum equation :

$$\frac{\partial w}{\partial t}+u\frac{\partial w}{\partial r}+w\frac{\partial w}{\partial z}=-\frac{1}{\rho}\frac{\partial p}{\partial z}+\frac{\mu}{\rho}\left(\frac{\partial^2 w}{\partial r^2}+\frac{1}{r}\frac{\partial w}{\partial r}+\frac{\partial^2 w}{\partial z^2}\right)+g\beta\left(T-T_m\right) \quad (3)$$

$$r\text{-momentum equation: } \frac{\partial u}{\partial t}+u\frac{\partial u}{\partial r}+w\frac{\partial u}{\partial z}=-\frac{1}{\rho}\frac{\partial p}{\partial r}+\frac{\mu}{\rho}\left(\frac{\partial^2 u}{\partial r^2}+\frac{1}{r}\frac{\partial u}{\partial r}-\frac{u}{r^2}+\frac{\partial^2 u}{\partial z^2}\right) \quad (4)$$

,

where *μ, g, β* and *T* represent viscosity, gravitational acceleration and coefficient of thermal expansion and temperature, respectively.

4-I.2.3 Boundary conditions

At the beginning of the simulation (*t=0*), the cylindrical TES system is filled with a certain height of PCM (i.e. z=H) having a temperature of T_0 which is lower than melting temperature (T_m). The bottom wall (i.e. z=0) is assumed thermally insulated. In order to initiate the melting process, the surrounding walls of cylindrical TES system is subject to a temperature, T_h which is 10 ˚C higher than melting temperature (T_m). A schematic of the numerical model is presented below.

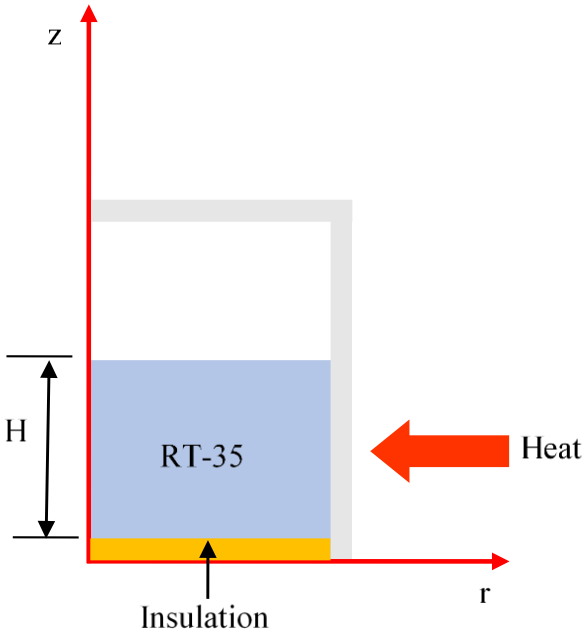

Fig.2. A schematic of numerical model

4-I.2.4 Mesh independency test

Three grid sizes are tested to examine the grid dependency test. The tested grid sizes are fine mesh, number of elements= 6965, simulation time= 50 minutes; finer mesh, number of elements= 15062, simulation time= 1 hour and 38 minutes, and extra fine mesh, number of elements= 33905, simulation time= 3 hours, 47 minutes. The melting fraction is numerically calculated for different mesh sizes, as shown below. Figure 3 shows that using finer mesh and extra fine mesh lead to almost identical results. However, extra fine mesh takes longer time to complete the simulation. Therefore, considering the time and the accuracy of simulation, the finer mesh is considered in the present study.

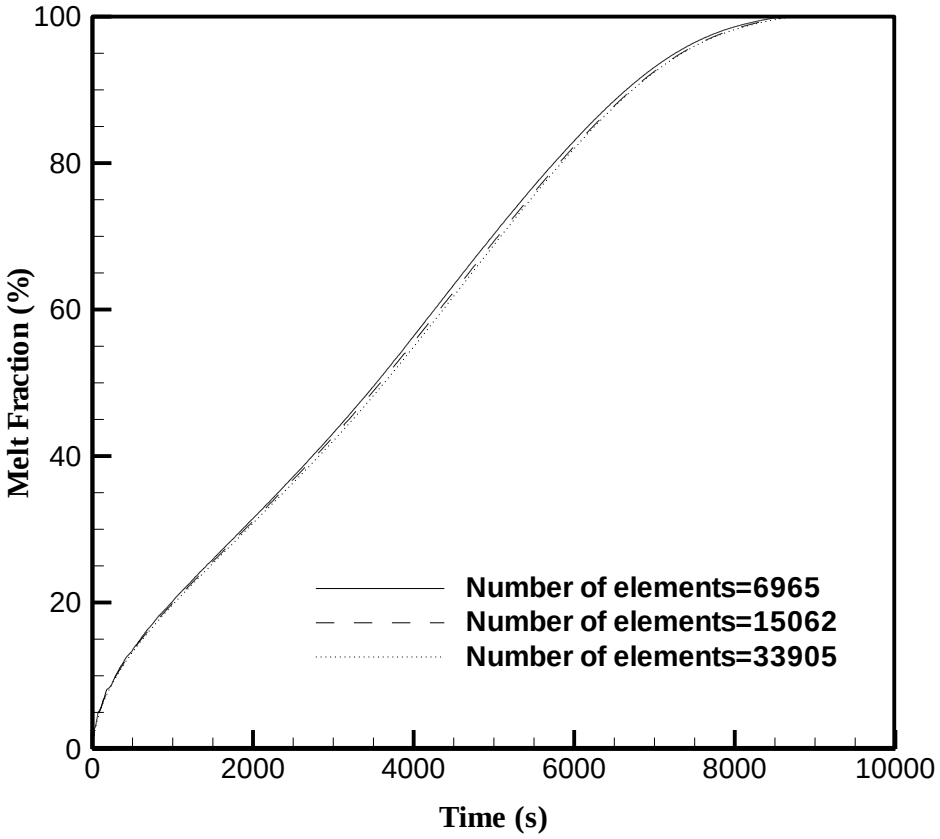

Fig.3. Melt fraction for different mesh quality

4-I.3 Results and discussion

Figure 4 shows experimentally and numerically the evolution of the melting process of RT-35. The melting process is tracked from time= 300 sec. to 7500 sec. The RT-35 starts melting after applying a heat source at constant temperature at the walls of the cylinder. The interface shortly appears after initiating the melting process. At 300 sec., the interface is parallel to the walls of the cylinder. The parallel interface indicates that the dominant mode of heat transfer is conduction. Between 1000 and 1800 sec., the melted RT-35 occupies more space at the upper part of the cylinder. With ongoing heating, the interface deforms, and the remaining solid RT-35 takes the shape of a cone starting from 3900 sec. to the end of the melting process. Most of the melted RT-35 occupies the upper part of the cylinder, while less amount of solid RT-35 is available at the lower part of the cylinder. The warm liquid RT-35 that has been heated through the walls of the cylinder rises up as it becomes lighter. The warm melted RT-35 accumulates at the top of the cylinder due to the thermal stratification effect. Since the melted RT-35 cannot cross the impermeable surface, the colder melted RT-35 moves downwards to give space for the warmer

melted RT-35. As a result, the transferred thermal energy to the solid RT-35 gradually drops as the melted RT-35 moves downwards. The figure below shows that the calculated numerical results are in a good agreement with the conducted experiment results.

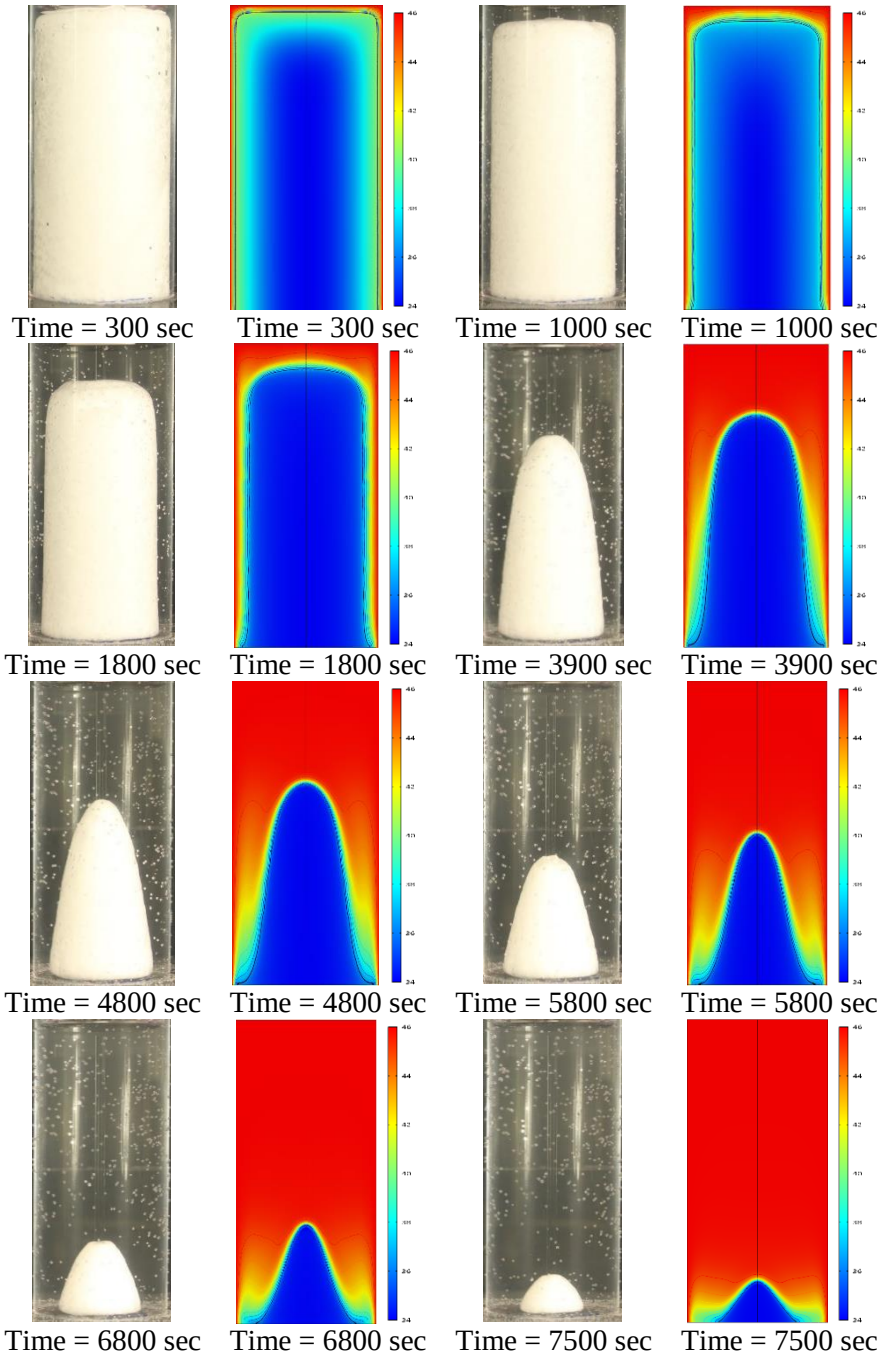

Fig.4. Comparison of melting pattern between the experimental and numerical results.

Figure 5 shows the comparison of melting faction with time between the experimental and numerical results. An almost linear trend is observed between the melting faction and time in both results with a higher melting at the beginning followed by a slower melting rate as melting progresses. At the beginning of the melting process, the temperature difference between the PCM in the TES system and the constant temperature bath is highest and therefore, melting rate of PCM is highest. As the melting progresses, the amount of liquid PCM in the TES system increases and so does its temperature. As a result, the temperature difference between the PCM in the TES system and the constant temperature bath decreases and the melting rate of PCM decreases.

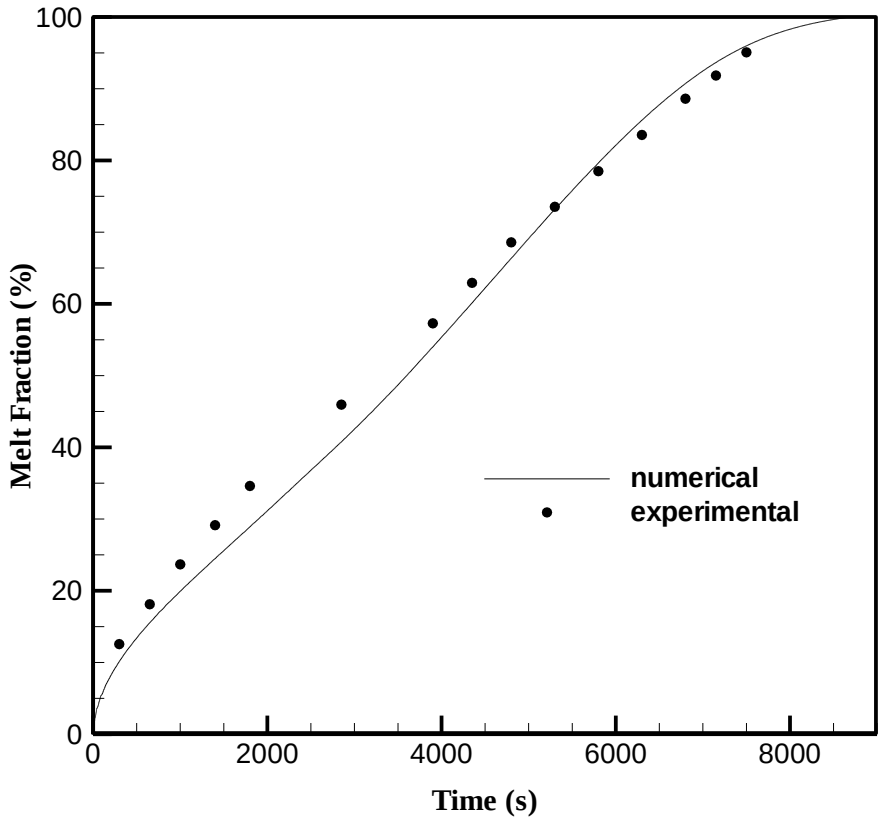

Fig.5. A comparison of melting faction with time between the experimental and numerical results.

Figure 6 shows the amount of transferred heat flux into the TES with time. At the beginning of the melting process, the PCM which is attached to the TES wall is solid and at a lower temperature than the bath temperature. At this point, the temperature difference is high which causes high heat transfer into the TES. With ongoing heating, the PCM close to the wall becomes warmer which reduces the temperature difference between inside and outside the TES. As a result, the heat transfer drops with time.

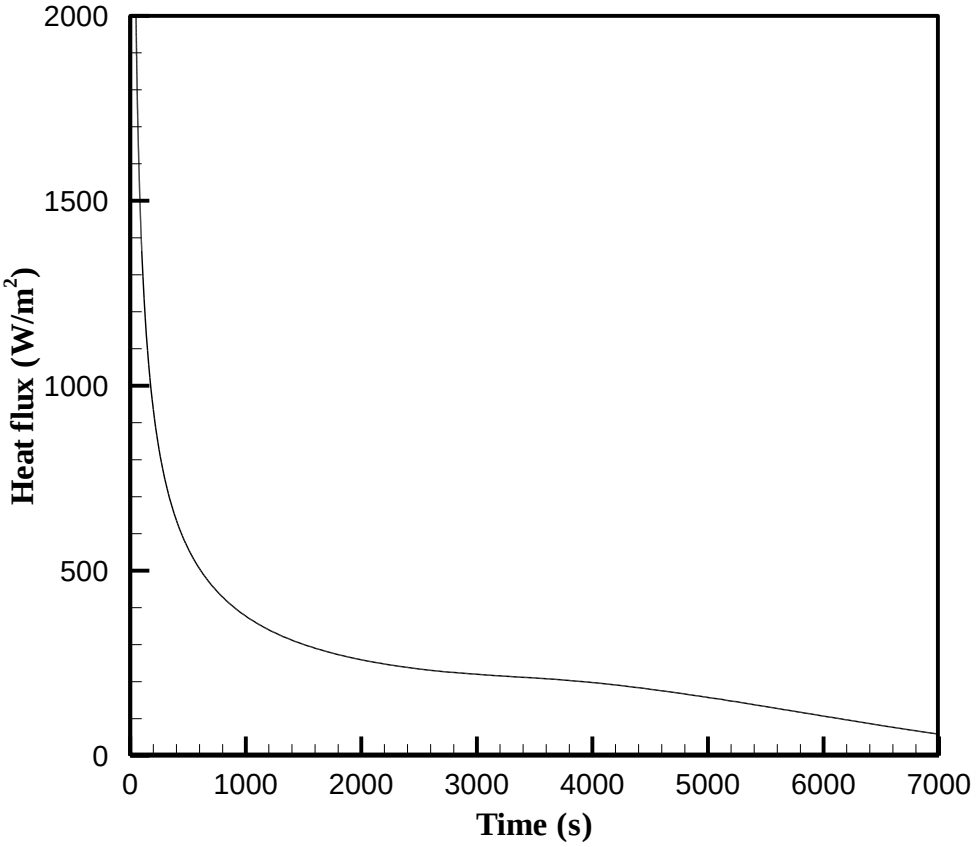

Fig.6. The heat flux transferred into the TES

Figure 7 shows the trend of Nusselt number, Nu throughout the melting of RT-35. The heat transfer rate at the beginning of the melting process is high due to the high difference temperature between the hot walls of the cylinder and the cold solid RT-35. When the RT-35 starts to melt, its temperature increases, which reduces the temperature difference. As a result, Nu is high at the beginning of the melting process then decreases with time.

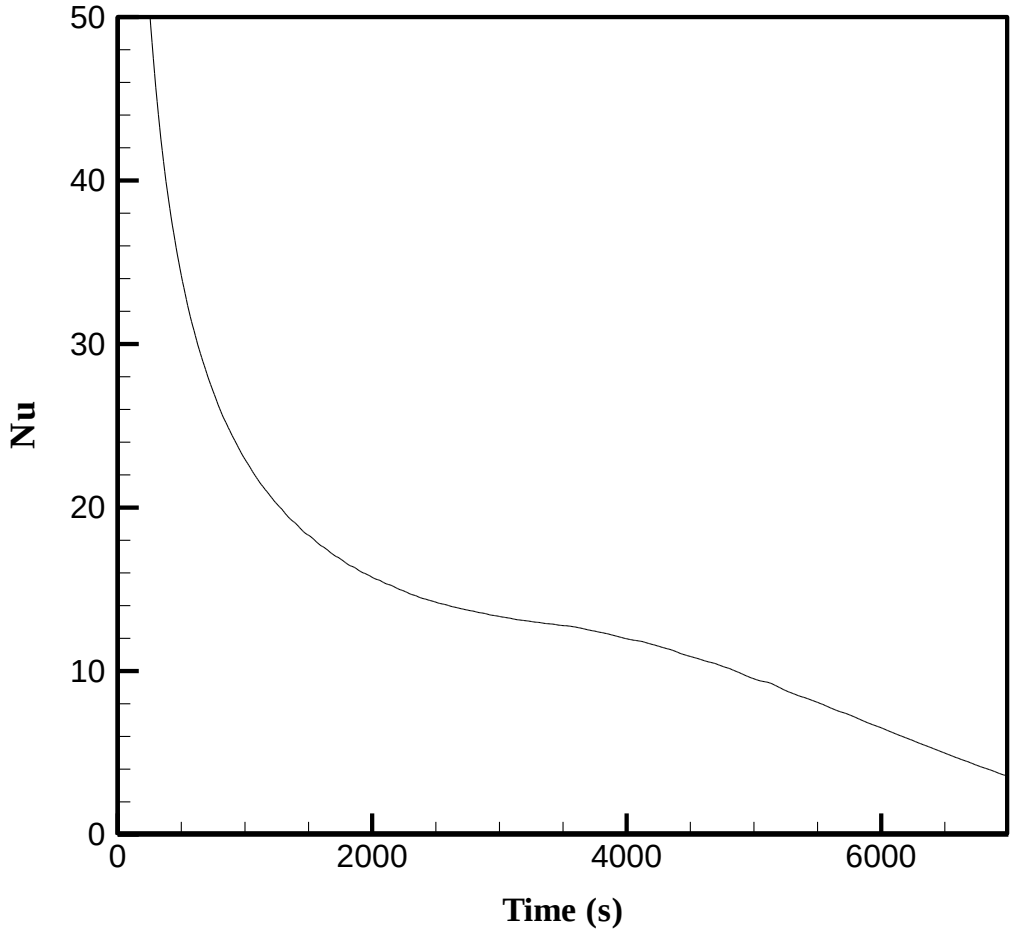

Fig.7. Nusselt number behavior throughout melting process.

4-I.4 Conclusion

A numerical and experimental investigation on the melting process of RT-35 filled in a vertical cylindrical enclosure is performed. The numerical model results are compared with experimental work and good agreement are achieved. Visualization of melting comparison shows a good agreement; however, some discrepancy is observed. The reason for the discrepancy may be attributed to the fact that (i) air is trapped inside the TES system and (ii) the bottom of the TES system may not be properly insulated. It is seen that at the early stage of melting process conduction is the dominant form of heat transfer from the walls. As the melting process progresses, natural convection is developed until dominates the heat transfer process. At the early stages of

the process, the heat transfer rate is high which is degraded at the later stages due to decreases in temperature difference.

4-I.5 Nomenclature

H height of the filled PCM in TES system [cm]

T temperature [$^{\circ}$C]

k thermal conductivity [W/m.K]

c_p specific heat at constant pressure [kJ/kg K]

h latent heat of fusion [kJ/kg]

g gravitational acceleration [m/s^2]

Greek symbols

β coefficient of thermal expansion [1/K]

μ dynamic viscosity [Pa.s]

ρ density [kg/m^3]

Subscripts

m melt

h hot

0 room

Abbreviations

TES thermal energy storage

PCM phase change material

RT Rubitherm

Ra Rayleigh number

Part II: An Investigation on the melting process of nano-PCM : Copper oxide nanoparticles dispersed into RT-35

"A version of this part has been accepted for publication in CSME transaction: Soroush Ebadi, Mohamadhossein Hjiyan, Syeda Tasnim, Amir. A. Aliabadi, Shohel Mahmud "Effect of Dispersing Copper Oxide Nanoparticles into RT-35 filled Circular Thermal Energy Storage System, CSME transactions, 2018."

4-II.1 Introduction

The increase in the amount of greenhouse gasses especially Carbon dioxide caused by burning fossil fuels has caused a serious environmental concern known as global warming. On the other hand, the increase in the worldwide population and industrial units have forced energy suppliers to search for alternate energy sources (i.e. renewable energy) and or use of energy efficiently. Thermal Energy Storage (TES) systems have developed with the aim of storing thermal energy effectively and release that energy in the demand time. TES systems are divided into three main groups including: (i) Sensible Heat TES system, (ii) Latent Heat TES system and, (iii) Thermo-Chemical TES system. However, among these three groups, LHTES system is more attractive. LHTES systems use PCMs to store or release thermal energy which offers two main advantages: (i) higher capacity of storing energy (i.e. 5-14 times higher than sensible heat TES) and (ii) smoother temperature fluctuations during the operation [1,2]. A wide variety of PCMs are available with different melting temperatures (Tm) which have been used for both cooling and heating purposes. Paraffin waxes, hydrated salts and organic compounds (e.g. Coconut oil) are the most available types of PCMs. Although PCMs seem to be a proper material for store/release of thermal energy, they suffer from a low thermal conductivity. This disadvantage leads to longer melting/solidification time, which affect the performance of the LHTES system [3]. Several methods have been proposed to enhance the thermal conductivity of PCMs such as (i) dispersing highly conductive nanoparticles into the PCM, which is the main purpose of this study, (ii) inserting metal fins, and (iii) the use of conductive porous medium [4]. Different weight fractions/volume fractions of nanoparticles can be dispersed in to the PCM to increasing its thermal conductivity. However, in practical, sedimentation is an issue caused by using high weight/volume fractions of nanoparticles [5,6]. Different configuration of PCM container such as rectangular, cylindrical (both horizontal/vertical), and spherical can be

used. Cylindrical can be installed both vertically and horizontally according to a specific application/ occupied space [7]. In this paper, the main aim of study is to investigate the melting process of a nano-PCM filled in a vertical cylindrical enclosure. By surveying the literature, it can be found that a considerable number of researchers have studied the use of vertical cylindrical enclosures filled with nano-PCM. Wu et al. [8] performed a numerical study on the melting process of Paraffin enhanced with Copper nanoparticles filled in a cylindrical enclosure which was heated from the bottom. It was found that the melting rate was 13.1 % improved by using 1wt. % of nanoparticles. Sciacovelli et al. [9] numerically studied the melting of paraffinic PCM with copper nanoparticles. In their investigation, the nano-PCM was isothermally heated by placing an inner tube at the center of cylindrical enclosure. It was reported that by using 4% volume fraction of nanoparticles, the melting time was decreased by 15%. Das et al. [10] numerically studied the melting process of n-eicosane enhanced with carbon allotropes. The enclosure was isothermally heated placing an inner pipe at the center. It was concluded that by using 1 % volume fraction of single-walled carbon nanotubes, the melting time melting time was decreased by 15%. The melting time was decreased up to 25% with the use of 1% volume fraction of graphene. An experimental study on melting process of 1-dodeconal enhanced with carbon nanotubes was performed by Zeng et al. [11]. In their experiment, the cylindrical enclosure was insulated from the surroundings and heated from the bottom. It is reported that by dispersing the carbon nanotubes, melting rate was degraded due to the increase of viscosity and decrease in the natural convection. Fan et al. [12] experimentally investigated the effect of adding Graphene nanoplatelets in to tetradecanol on the melting rate. The cylindrical enclosure was isothermally heated from the bottom. It was reported that by using 3 wt.% of nanoparticles at the temperature of 55 $^{\circ}$C, a 8% decrease in the melting time is observed.

According to the literature, the melting process of a nano-PCM inside a vertical cylindrical enclosure, insulated from the bottom, and isothermally heated from the sides has not been extensively investigated. In this work, an experimental and numerical investigation are performed to study the effect of adding Copper oxide nanoparticles into RT-35 with the melting temperature (T_m) in a range of 34 $^{\circ}$C- 36 $^{\circ}$C. To do so, an experimental setup is built to visualize and compare the melting process of pure PCM and nano-PCM. Moreover, a COMSOL simulation is developed to compare the energy stored in PCM and nano-PCM.

4-II.2 Experimental investigation

4-II.2.1 Experimental setup

The primary objective of the experimental work is to visualize and compare the melting process of PCM and nano-PCM. The experimental setup is consisted of two transparent acrylic pipe with the inner diameter of 4.4 cm, a transparent water bath equipped with temperature regulator, a circulation pump, and a digital camera to capture the melting pattern periodically. Two cylindrical acrylic pipes are vertically attached to a thick plastic plate (thickness= 3.5 cm) with the center-to-center distance of 13 cm. The cylindrical pipes are thermally insulated from the bottom and to avoid any pressure at the top of PCM/nano-PCM, it is kept open from the top. A schematic of the experimental setup is shown in Fig.1.

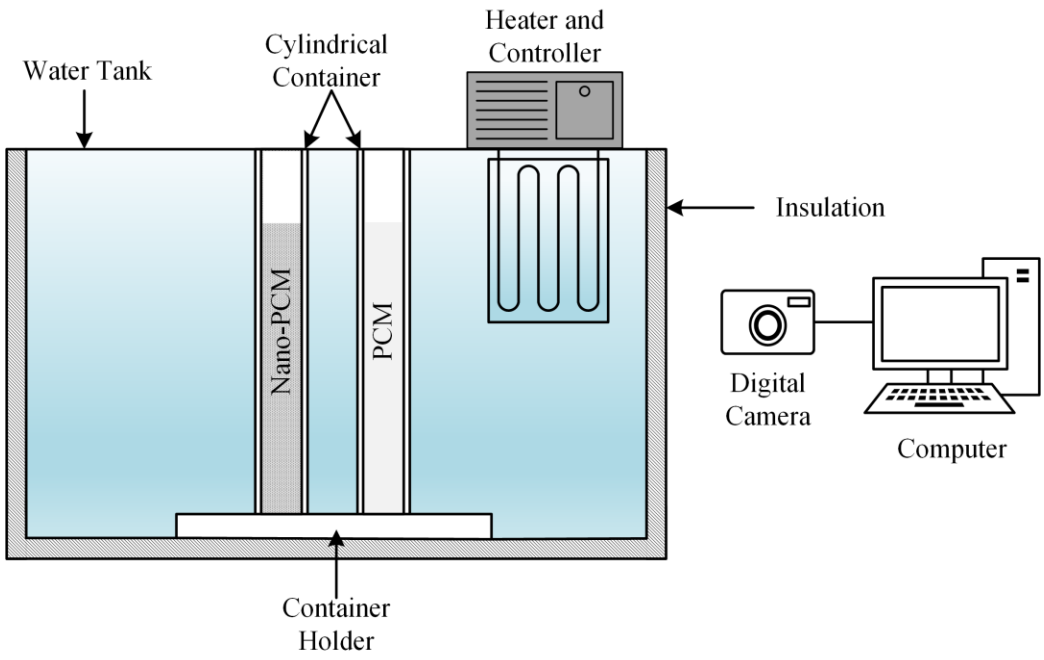

Fig.1. A schematic of the experimental setup

4-II.2.2 Nano-PCM preparation

One of the main challenges associated with the use of nano-PCM is the sedimentation of nanoparticles at the bottom of enclosure after several cycles of operation. Therefore, preparation of the nano-PCM is an important step for the experimental work. At the first step, the required amount of RT-35 and Copper oxide nanoparticles to have a 0.2 wt.% nano-PCM was weighed by

a precise balance. It should be mentioned that dispersing Copper oxide nanoparticles into RT-35 results to a dark black fluid. Thus, to have a clear melting visualization, low amount of nanoparticles is used. Then, the mixture was heated up to 60 ˚C and stirred by using a magnetic stirrer for 24 hours. To ensure the homogeneity of mixture and release the trapped air inside the nano-PCM, an ultrasound sonicator was used for two hours. At the next step, the nano-PCM was kept in a bath with the temperature of 45 ˚C for three hours (more than the time required for melting experiment) to see the amount of sedimentation. After ensuring the homogeneity of mixture, the nano-PCM was solidified gradually at the room temperature (i.e., $T_0 = 23$ ˚C). Solidification at the temperatures close to the T_m requires a longer time, however, it provides the advantages of having less trapped air inside the nano-PCM and avoiding the sub-cooling effect. Table.1 shows the thermophysical properties of RT-35 and Copper Oxide nanoparticles.

Table 1. Properties of RT-35 and CuO nanoparticles

Property	RT-35 [13]	Copper oxide[14]
β (1/K)	6×10^{-4}	85×10^{-7}
h_{sf} (kJ/kg)	170	___
k (W/m K)	0.2	18
μ (Pa.s)	0.023	___
c_p (kJ/kg K)	2	0.54
ρ (kg/m^3)	815	6500

4-II.2.3 Experimental procedure

Several steps were taken to start the experiment. First, a predetermined amount of molten Pure PCM and nano-PCM was poured in cylindrical pipes at the same height (H= 8.3 cm) representing Rayleigh number of 10^7. Then, the PCM/nano-PCM were gradually solidified by keeping the setup at the room temperature. Next, the temperature of the constant bath was set to 45 ˚C. To ensure the accuracy of the thermal regulator, a T-type OMEGA thermocouple was placed inside the bath and monitored the temperature. The Cylindrical TES system enclosures were suddenly placed inside

the bath to initiate the melting process. A digital camera was used to record the melting pattern periodically (i.e. every five minutes) during melting process.

4-II.3 Numerical investigation

4-II.3.1 Numerical model

To study the effect of dispersing nanoparticles to pure PCM on the thermal fields, melting fraction and energy stored, a numerical model with the same geometry as the experimental setup was developed by using COMSOL Multiphysics. The model is insulated from the bottom, isothermally heated from its sides, and filled with PCM/nano-PCM at the height of H. The liquid phase of PCM/nano-PCM is assumed as a Newtonian incompressible fluid. A 2-D view of the numerical model is shown below.

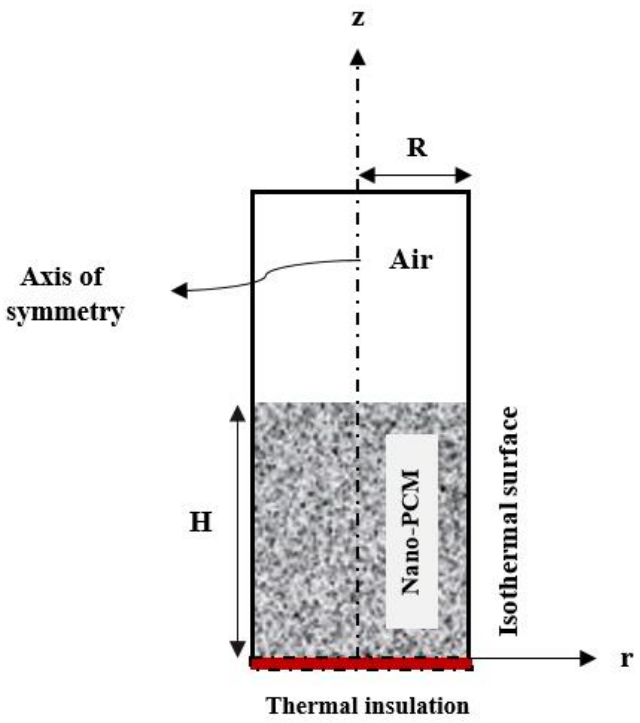

Fig. 2. A 2-D view of the numerical model

The governing equations representing the conservation of mass, momentum and transferred energy are presented below [15]:

$$\text{Continuity equation: } \frac{\partial u}{\partial r}+\frac{u}{r}+\frac{\partial w}{\partial z}=0 \tag{1}$$

where u and w are the components of velocity in r-direction and z- direction, respectively.

$$\text{Energy equation: } \frac{\partial T}{\partial t}+u\frac{\partial T}{\partial r}+w\frac{\partial T}{\partial z}=\frac{k}{\rho C_p}\left[\frac{1}{r}\frac{\partial}{\partial r}\left(r\frac{\partial T}{\partial r}\right)+\frac{\partial^2 T}{\partial z^2}\right] \tag{2}$$

where t, K,ρ and C_p represent time, thermal conductivity, density and specific heat at constant pressure, respectively.

$$\text{Momentum (z-direction): } \frac{\partial w}{\partial t}+u\frac{\partial w}{\partial r}+w\frac{\partial w}{\partial z}=-\frac{1}{\rho}\frac{\partial p}{\partial z}+\frac{\mu}{\rho}\left(\frac{\partial^2 w}{\partial r^2}+\frac{1}{r}\frac{\partial w}{\partial r}+\frac{\partial^2 w}{\partial z^2}\right)+g\beta\left(T-T_m\right) \tag{3}$$

$$\text{Momentum(r-direction): } \frac{\partial u}{\partial t}+u\frac{\partial u}{\partial r}+w\frac{\partial u}{\partial z}=-\frac{1}{\rho}\frac{\partial p}{\partial r}+\frac{\mu}{\rho}\left(\frac{\partial^2 u}{\partial r^2}+\frac{1}{r}\frac{\partial u}{\partial r}-\frac{u}{r^2}+\frac{\partial^2 u}{\partial z^2}\right) \tag{4}$$

where μ, g, β and T represent viscosity, gravitational acceleration and coefficient of thermal expansion and temperature, respectively. The amount of stored energy is one of the main parameters for designing a LTES system which can be determined by Eq. 5 [16].

$$E=\int_0^t \dot{Q}(t)dt \tag{5}$$

In this equation, $\dot{Q}(t)$ is the transferred heat during the melting process which can be determined by Eq.6 below.

$$\dot{Q}(t) = (\pi \mathrm{d}) \int_0^H \left(-k \frac{\partial T}{\partial r}\right) dz \; + (2\pi) \int_0^R \left(-k \frac{\partial T}{\partial z}\right) r \, dr \qquad (6)$$

Where *d* and *k* are the inner diameter of the circular pipe and thermal conductivity of the nano-PCM respectively.

Dispersion of nanoparticles to PCM results to new properties such as density, viscosity, thermal conductivity, and heat capacity. The thermophysical property relationships for the nano-PCM can be found in [17]. Moreover, as the change in the phase of the nano-PCM occurs within a transition stage, the properties of the nano-PCM are affected by a transition temperature range (i.e. $T= T_m-\Delta T$, and $T= T_m+\Delta T$). The thermophysical properties of the nano-PCM at the transition stage can be found in [18]. In addition, a Gaussian function is used to approximate the heat capacity during the phase change process [19].

4-II.3.2 Grid size and time step independency test

To test the mesh size and time intervals independency, simulations were carried out in different steps. First, the melting fraction was calculated by using three different mesh sizes including (i) 6965 elements, (ii) 15062 elements and (iii) 33905 elements. The result of this test is shown in Fig.3.

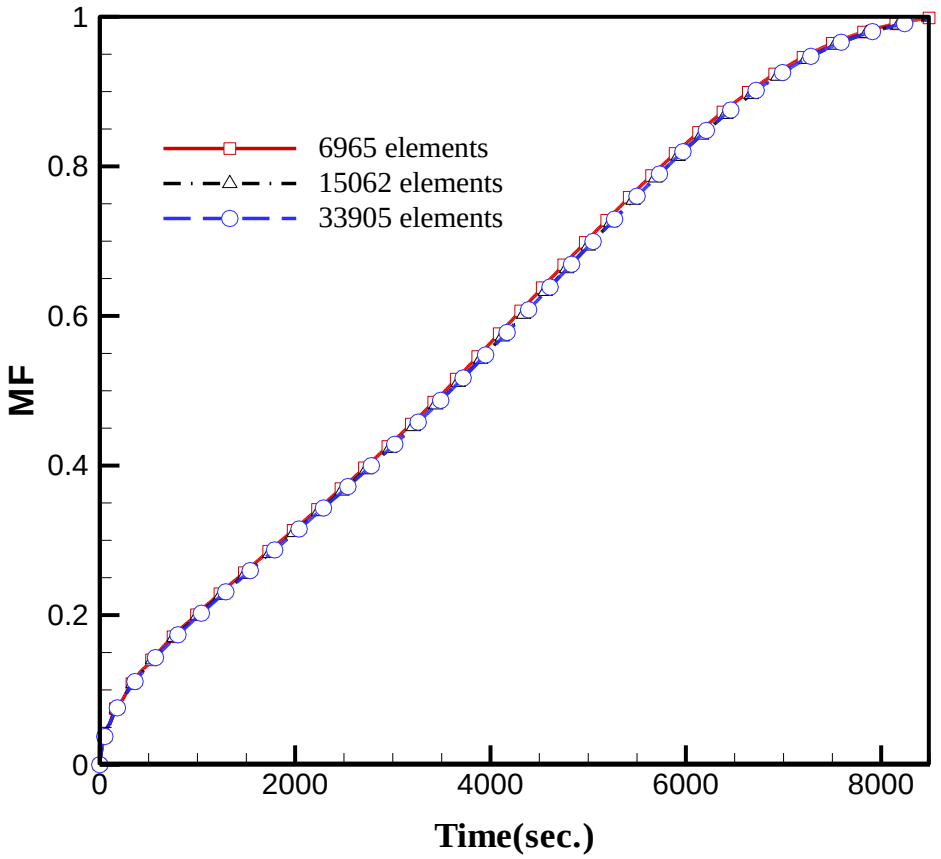

Fig. 3. Grid size independency test

As it can be seen from Fig. 3, the values of melting fraction for different meshes are almost identical. Hence, to obtain the proper accuracy and less simulation time, the mesh quality with 15062 elements was selected. At the next step, the time step independency is examined. In this test, melting fraction was calculated by using three different simulations with different time steps. Table 2 shows the different time steps used in these series of tests.

Table 2. Time intervals used to examine the time step independency

Time zone (s)	Time step (s)		
	Test 1	Test 2	Test 3
0 to 10	0.01	0.1	0.005
10 to 100	0.1	1	0.05

Figure 4 presents the result of these tests. As it can been seen, there is a slight difference in the values of melting fraction resulted by these three time steps. Therefore, to have both accuracy and less simulation time, the simulations were carried out by using the time interval in Test 2.

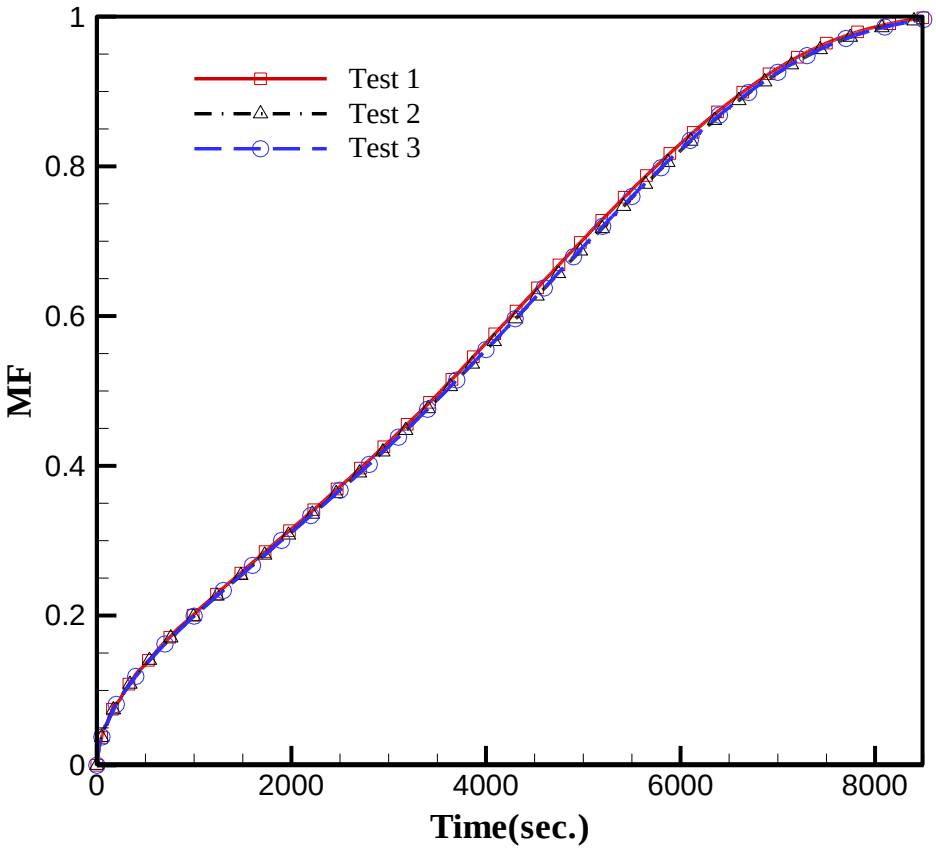

Fig. 4. Time step independency test

4-II.3.3 Validation with experimental work

Figure 5 presents a melting visualization comparison between numerical results and experimental work for 0.2 wt.% of nano-PCM. To do so, some selected results obtained from numerical and experimental are compared. In general, a good agreement is achieved. However, there are some discrepancies in melting pattern, which may be due to the two main factors. First, the air trapped inside the nano-PCM in the experimental work was seen to cause a non-uniform melting at the times that trapped air was released. The other major factor is neglecting of the thermal resistance of the acrylic pipe in the numerical model. As a result, more heat could be transferred between hot wall and the nano-PCM during numerical simulation.

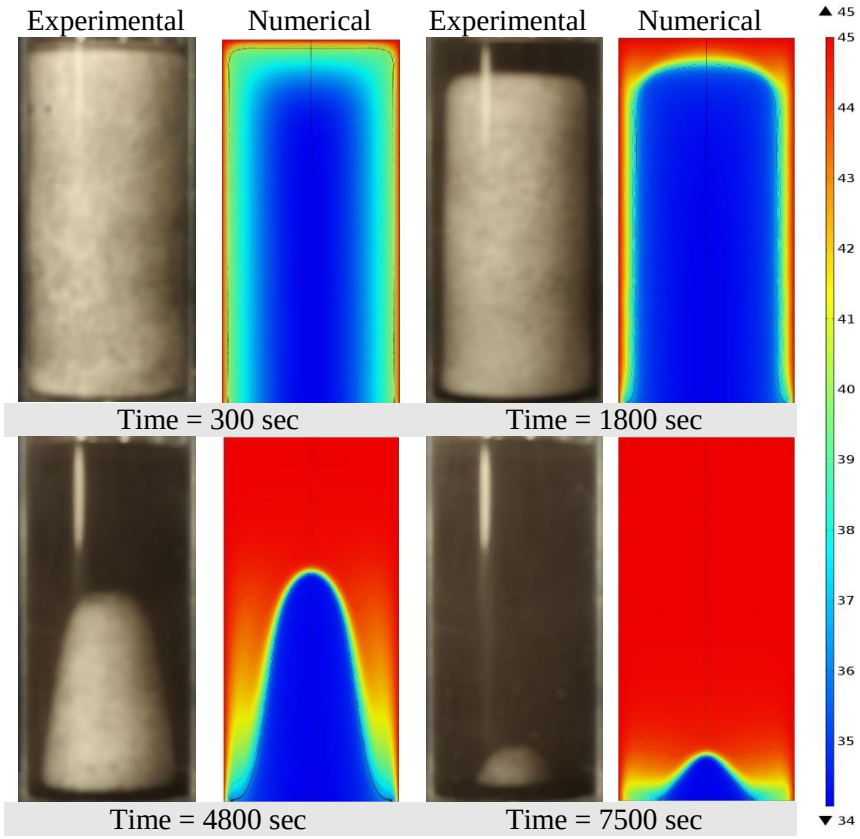

Fig. 5. Validation of numerical model with experimental work

4-II.4 Results and discussion

4-II.4.1 Melting pattern and visualization

In this section a comparison of melting pattern between pure PCM and Nano-PCM is presented. Some selected results are presented in figure 6. After a few minutes of initiating the experiment, a thin layer of molten PCM/nano-PCM appeared which lead to a solid-liquid interface. At the early stages of melting process (up to 300 s), conduction was the dominant mode of heat transfer since the solid-liquid interface is parallel to the lateral walls. As time furthered, the buoyancy force started to dominate the viscous force and natural convection started to establish. This phenomenon can be clearly observed from the remaining shape of the solid PCM/nano-PCM. At the later stages of melting process (i.e. after 3600s), convection became the dominant mode of heat transfer which resulted to a dome shape solid PCM/nano-PCM. As it can be seen from the figure 6, an

improvement in the melting rate is observed by using 0.2 wt. % nano-PCM. To assist the discussion, the melting fractions for both PCM and nano-PCM at different times was calculated from the digital photos by using a software called Grafula. Calculation of melting fraction from digital image was also used in other published works in the literature such as [20].

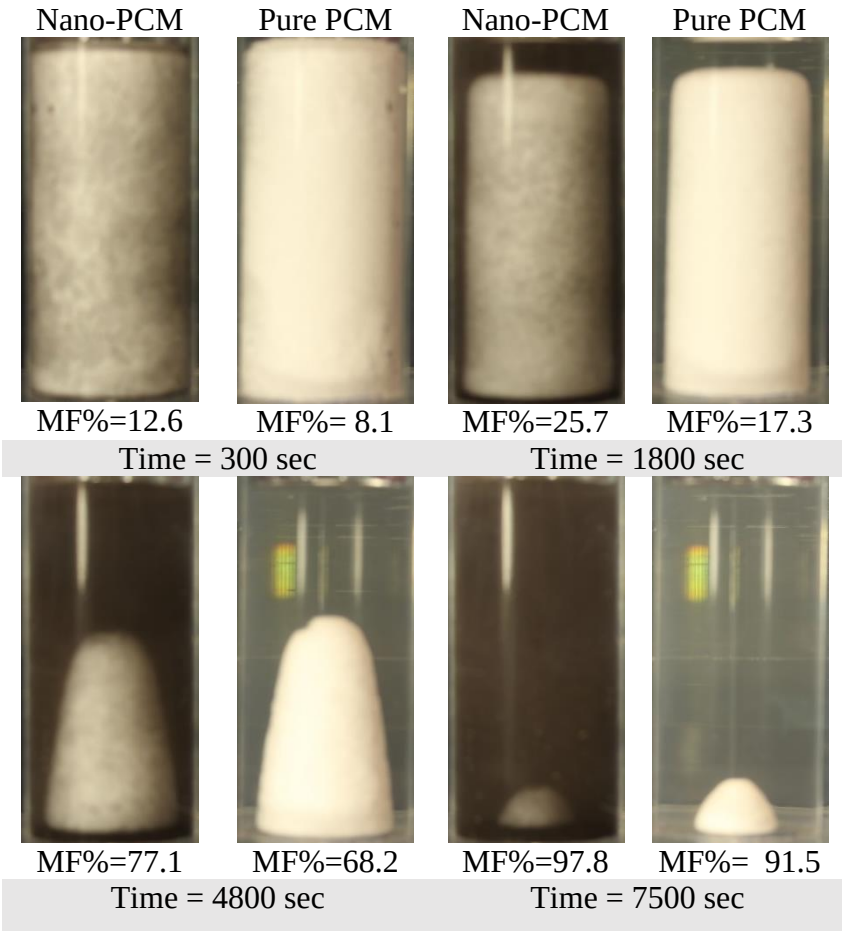

Fig. 6. Visualization of melting pattern for nano-PCM and pure PCM

4-II.4.2 Energy stored

Figure 7 presents the stored energy during the melting process for both the nano-PCM and the pure PCM cases. At the beginning of melting process, the temperature difference between hot lateral walls of the circular enclosure and cold PCM/nano-PCM is more than the later stages of melting process. As a result, the slope of energy stored is higher at the early stages (i.e. up to 600s) than

other times. From this point onward, the rate of energy-stored decreases until it reaches to zero by reaching to the thermal equilibrium. The amount of energy stored during the melting process mainly depends on the specific heat capacity and the latent heat capacity of nano-PCM/PCM. As it can be seen from the thermophysical relations of the nano-PCM presented in [21], adding nanoparticles to the PCM at the liquid phase increases the heat capacity, while, it decreases the latent heat capacity of the PCM. Therefore, it is expected to have a lower amount of energy stored in the nano-PCM which will be further degraded by adding higher weight/volume fractions of nano-particles. The amount of this decrease in the energy stored is not significant in this work due to the use of low weight fractions of nanoparticles in the experimental work. However, this phenomenon is more apparent in Groulx's numerical study [19].

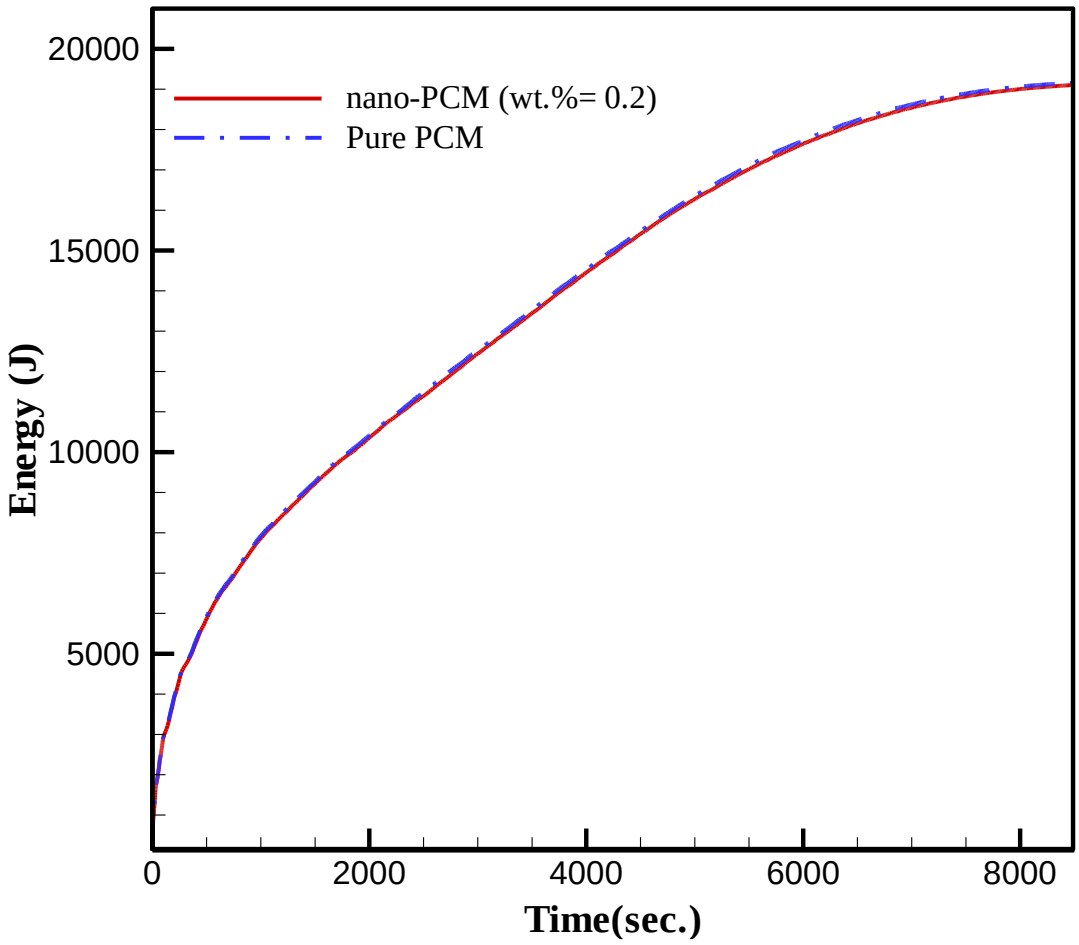

Fig.7. Stored energy

4-II.5 Conclusion

A numerical and experimental study were conducted to investigate the effect of dispersing copper oxide nanoparticles into the RT-35 as the base PCM on the melting rate and energy stored. The followings can be concluded from the results obtained from this work:

- Dispersion of the Copper oxide nanoparticles in to the RT-35 increased the melting rate due to enhancing the thermal conductivity of base PCM. From the numerical simulations, it can be found that this improvement increases by using higher weight/volume fractions of the nanoparticles. However, it is worth mentioning that in practical, dispersion of high weight/volume fractions of nanoparticles results to the sedimentation issue.
- The rate of energy stored is seen to be high at the beginning of melting process due to the high temperature gradient. This stored energy rate degraded to zero at the end of melting process due to the thermal equilibrium. In addition, nano-PCM showed a lower amount of energy stored.
- Finally, as both melting time (charging) and the total energy stored are important for an optimal design of a LHTES system, it is recommended to maintain a balance between improvement in the thermal conductivity and decrease in the energy stored if use of nano-PCM is required.

4-II.6 Nomenclature

H height of the filled PCM in TES system [cm]

T temperature [$^{\circ}$C]

k thermal conductivity [W/m.K]

c_p specific heat at constant pressure [kJ/kg K]

h latent heat of fusion [kJ/kg]

g gravitational acceleration [m/s^2]

Greek symbols

β coefficient of thermal expansion [1/K]

μ dynamic viscosity [Pa.s]

ρ density [kg/m^3]

Subscripts

m melt

h hot

0 room

Abbreviations

TES thermal energy storage

PCM phase change material

RT Rubitherm

Ra Rayleigh number

Chapter 5

Thermal Energy Storage System with Metal Mesh Porous Medium

A version of this chapter is under preparation to be submitted to a journal: **Soroush Ebadi**, Syeda Tasnim, Amir A. Aliabadi, Shohel Mahmud, 2018.

5.1 Introduction

Thermal Energy Storage (TES) systems have been developed with the aim of storing/releasing thermal energy efficiently. Latent Heat Thermal Energy Storage (LHTES) system, Sensible Heat Thermal Energy Storage (SHTES) system, and Thermo-Chemical Energy Storage (TCES) systems are the major categories of TES systems. However, LHTES systems have invoked more interest than SHTES and TCES systems due to the larger storage capacity and smoother temperature fluctuations during their operation [1-3]. LHTES systems have been used in various applications including energy management of buildings [4-7], solar thermal systems for storing the heat [8-11], and thermal management of electronic devices [12-14] and batteries [15-17]. Phase Change Materials (PCMs) are used as the storage medium to store and release thermal energy in LHTES systems. Different PCMs with a wide range of phase change temperature (T_m) including Paraffin waxes, hydrated salts, and organic compounds have been used as the storage media in LHTES systems for cooling/heating purposes. Different configurations of PCM holding containers, such as, spherical, rectangular, and cylindrical have been used as LHTES system. Cylindrical LHTES systems offer the advantages of ease of manufacturing and can be installed both vertically and horizontally. A comprehensive review of different configurations of LHTES systems is available in [18, 19]. Despite all of the good features of PCMs, they suffer from a low thermal conductivity, which degrades the performance of LHTES systems by increasing the required time for charging (melting) and discharging (solidifications) processes [20-22]. Several methods such as inserting highly conductive porous materials, dispersing metal nanoparticles, and inserting metal fins have been purposed by the researchers to enhance the effective thermal conductivity of the PCMs [23-24]. However, there are some disadvantages for each of the purposed methods. For instance,

sedimentation of nanoparticles due to the use of high weight/volume fractions leads to an insignificant enhancement in thermal conductivity [24]. Moreover, inserting metal fins and porous materials such as metal foams occupies a portion of the volume of LHTES systems that results in a lower amount of filled PCM, which degrades the amount of stored energy in LHTES [25, 26]. Several research works are available in the literature regarding the use of porous material to enhance the thermal performance of LHTES systems with different configurations filled with PCM/nano-PCM or in the heat exchangers.

5.1.1 Metal Foam

Many researchers have used highly conductive metal porous foams (i.e. mainly copper and aluminum) in different configurations of PCM containers such as rectangular and cylindrical to improve the thermal performance of LHTES systems. It is reported that this approach offers the advantages of improving the heat transfer rate and the effective surface of heat transfer. Starting with rectangular LHTES system, Baby and Balagi [27] experimentally studied the heat transfer characteristic of an aluminum LHTES system during melting process by embedding copper foam into n-eicosane. Different angles of inclination of LHTES were examined. It is concluded that heat transfer rate was enhanced by the presence of metal foam while changing the orientation of the LHTES system didn't show significant influence on the thermal performance. Chen et al. [28] experimentally and numerically studied the impact of using aluminum porous foam embedded in a LHTES system filled with paraffin wax. It is reported that melting process was enhanced by the presence of the metal foam. Mancin et al. [29] experimentally analyzed the effects of embedding different copper matrixes into different PCMs subjected to various heat fluxes. It is concluded that although use of copper foam delayed the onset of phase change process, it ended earlier due to a uniform temperature distribution among the enclosure. In addition, an insignificant effect of different copper matrixes on heat transfer enhancement was reported. Hossein et al. [25] numerically studied the melting performance of nano-PCM (CuO nanoparticles dispersed in Cyclohexane PCM) inside isothermally heated porous medium (i.e., composite porous medium). Authors concluded that lower porosities and higher volume fractions resulted in a faster melting process. Tasnim et al. [30] used numerical simulation and scale analysis to study the convection effect on the melting process of a nano-PCM (CuO nanoparticles dispersed in Cyclohexane PCM) embedded inside a Darcy porous medium. Authors identified the qualitative similarity in melting

process for porous and non-porous medium. Moreover, the authors reported that by using nano-particles, the heat transfer by conduction and convection decreased. Al-Jethelah et al. [31] used Brinkman model to study the melting process of a nano-PCM (CuO nanoparticles dispersed in water) in porous medium. Authors detailed numerical study and scale analysis concluded that the melting process can be enhanced by increasing Rayleigh number, Darcy number and volume fraction of nanoparticles. Yang et al. [32] experimentally investigated the thermal performance of a shell and tube LHTES system filled with paraffin wax in the presence of copper foam and a fin at the bottom. The results indicated that the melting process was shortened significantly comparing with use of pure PCM. Zhang and He [33] numerically studied the heat transfer enhancement using composite PCM. To do so, an aluminum porous material with different porosities from bottom to the top was embedded in a rectangular container filled with paraffin. The findings indicated that embedding a metal foam with a porosity gradient enlarged the rate of heat storage. In addition, it is stated that conduction is the dominant form of heat transfer during the melting process when porous metal foam is used. Li et al. [34] experimentally studied the effect of using microencapsulated PCM embedded in the pores of a copper foam on the thermal behaviour of a LHTES system. A uniform temperature distribution inside the PCM due to the thermal conductivity enhancement is reported. Because of such enhancement, the surface temperature of the metal foam/PCM decreased significantly compared to the pure PCM. A numerical study on the effects of pores configuration of a metal foam on thermal characteristic of a LHTES system was performed by Deng et al. [35]. Comparing porous metal foams with the same porosity and different fractal sizes, revealed that smaller fractal had a better heat transfer rate than the porous foam with larger pores dimensions. In addition, it is concluded that different independent solid-liquid interface existed while porous metal foam is used. Kohyani et al. [36] numerically investigated the melting process of nano-PCM in porous medium in the presence of a magnetic field. Results obtained by this work showed that varying the volume fraction of nanoparticles had less effect on the melting rate than changing porosity. Moreover, it is concluded that applying an intense magnetic field increased the melting rate. The thermal performance of a LHTES system in the presence of a copper foam was numerically and experimentally investigated by Zheng et al. [37]. It is concluded that the melting time was 20.5% decreased by embedding the copper foam and a uniform temperature distribution was existed. In addition, it is reported that natural convection is not ignorable during melting process of paraffin wax in the presence of the metal

foam. Jourabian et al. [38] numerically investigated the melting process of PCM in the presence of porous medium and nanoparticles. It is reported that the melting rate enhanced by the use of nanoparticles and metal foam. In addition, it is concluded that use of high volume fractions of nanoparticles lead to an increase in the dynamic viscosity of the PCM, which degraded natural convection. Moreover, decreasing the porosity of metal porous foam enhanced the heat transfer rate.

Regarding the use of metal foam in a cylindrical geometry, Siahpush et al. [39] experimentally investigated the effects of embedding porous copper foam in a vertical cylindrical LHTES system filled with eicosane on the heat transfer characteristics. A copper foam was inserted inside an annular copper, which was heated isothermally from its sides. It is concluded that heat transfer was enhanced due to the increase in the effective thermal conductivity by using porous copper foam. Liu et al. [40] numerically investigated the influence of embedding metal foam inside a shell and tube LHTES which was heated from a pipe located at the center of the shell. The authors reported that heat transfer could be improved by more than seven times by using metal foam. In addition, it is concluded that structure configuration of the metal matrix and the inlet conditions of the heat transfer fluid had a significant impact on the performance of the shell and tube LHTES system. An investigation on the shell and tube LHTES system enhanced with porous material was conducted by Atal et al. [41]. The authors experimentally and numerically studied the impact of embedding aluminum porous material in LHTES system filled with paraffin wax. The effect of porosity of the metal matrix on the heat transfer enhancement was studied by using two different porosities of aluminum foam. It is reported that the operation time (i.e. melting and solidification) was significantly reduced due to use of porous material. Moreover, it was observed that the porous metal foam with lower porosity had better enhancement in the operation time due to higher overall thermal conductivity. Mahdi and Nsofor [42] numerically studied the effect of adding nanoparticles and porous foam to the PCM on thermal behaviour of a triplex-tube heat exchanger as a LHTES system. In their work, the effect of different volume fractions of the nanoparticles, porosity of the metal foam, and the temperature of heat transfer fluid on the thermal characteristics of LHTES were studied. Although it is found that combination of high volume fraction of nanoparticles with low porosity of the metal foam had better improvement on the melting rate, it is suggested to use low volume fractions of nanoparticles with higher porosity of metal foam which lead to lower reduction in the amount of PCM and natural convection. A numerical study on the

thermal performance of shell and tube LHTES system in the presence of porous medium was performed by Xu et al. [43]. In their work, the LHTES was partially filled with porous material with different configurations and at different locations. The authors proposed a criteria called *TES Density Rate* to optimize the performance of the LHTES systems. It is concluded that locating of the porous medium at the lower part had the best thermal performance. In addition, it is suggested to use highly conductive porous material with higher porosity and larger pore size. Xu et al. [44] numerically studied the optimal configuration of a metal foam embedded in horizontal shell and tube LHTES system filled with PCM. The effects of location, porosity, and configuration of the porous inserts on the thermal performance of the LHTES system during melting process were investigated. It is reported that the partial porous medium should be located at the bottom of LHTES system, which lead to a better thermal performance. In addition, a faster melting rate was observed due to the use of porous material.

In recent days, PCM and porous medium combination (i.e., composite PCM) is successfully used in battery thermal management applications for electric vehicles. Lithium-ion batteries have been widely used in hybrid/electrical vehicles due to their high power density. However, during the charging/discharging phase of the battery it is necessary to maintain a specific range of operating temperature of the battery to have an optimal life [45]. One of the methods for thermal management of batteries is the use of PCMs for heat dissipation during the operation cycles due to their high thermal energy density, reasonable price, and a wide range of phase change temperature [46]. As it is mentioned earlier, the low thermal conductivity of the PCM restricts the performance of LHTES systems, combination of the PCM and highly conductive porous foam have been suggested by several researchers to increase the thermal conductivity of the PCM. It is reported that use of composite PCM maintains the battery temperature within a safe zone and a more uniform temperature distribution in the battery is observed [47-51].

Another high potential application of PCMs is the thermal management of electronic devices. As the electronic devices are required to occupy a small space, the electrical kits should be built compactly. This leads to tremendous heat dissipations, which will greatly affect the performance of the electrical system or even it may lead to devise failure. In this application, PCMs are used to absorb the generated heat by electrical kits and maintains the operating temperature in a specific range (i.e. this range depends on the type of the chips). However, according to the low thermal conductivity of PCMs, it is required to be combined with nano-particles and porous material. In

this regard, Alshaer et al. [52] conducted an experimental investigation to study the effect of adding nanoparticles and porous material on thermal conductivity of a PCM. To serve this aim, RT-65, carbon foam, and multi wall carbon nanotubes (MWCNT) were used as the PCM, porous material and nanoparticles respectively. In their work, two different carbon foams called CF-20 and KL1-250 with different thermal conductivities were used. Different power densities were applied to study the effect of using each case on the thermal conductivity enhancement. Results showed that the adding carbon foam and MWCNT to RT-65 leaded to a higher thermal conductivity enhancement comparing adding only one of MWCNT or carbon foam. A numerical study on using carbon foam/PCM/nano carbon tubes in thermal management of electronic devices was conducted by Alshaer et al. [53]. In their investigation, different models called CF-20, CF-20 +RT-65, and CF-20+RT-65/ Nano carbon models with different carbon foam porosities were tested. The model was based on volume average technique and single domain energy equation. A CFD code was developed to solve the governing equations and results were validated by comparing with previous experimental works. It is reported that using a combination of RT-65, carbon nano tube and carbon foam with the porosity of less than 76 % reduced the model surface temperature up to 11.5%. However, this reduction in temperature is degraded to 7.8% when a carbon foam with a porosity of 88% is used. The thermal management of photovoltaic/thermal system in the presence of copper metal foam and different PCMs was numerically investigated by Mousavi et.al [54]. The impact of various parameters including solar radiation, inclination, and the inlet condition of the working fluid on the performance of the PV/thermal system were tested.

5.1.2 Wire mesh

Highly conductive metal wire meshes have been used in heat exchangers to increase the thermal performance of the system by increasing the heat transfer surface. Metal wire meshes can be built in different configurations (i.e. different wire diameters and porosities) with the advantages of ease of manufacturing and low manufacturing cost [55]. Interestingly, it is seen to be more efficient than use of porous metal foams due to effectively promoting the heat conduction to the outer walls while limiting axial conduction due to minimal contact between each mesh [56]. Several published works are available regarding the improvement of thermal performance of a heat exchanger by using wire meshes. Xu et al. [57] numerically and experimentally studied the heat transfer behaviour of a wire-screen mesh heat exchanger. It is reported that the heat transfer is dominated

by the porosity and density of the surface area of the wire mesh. In addition, conduction heat transfer was decreased by increasing the porosity of the mesh while the convection regime enlarged. In addition, it is reported that the material properties of wire such as thermal conductivity and heat capacity are other important parameters affecting the performance of the wire mesh heat exchangers. Dyga and Placzek [58] experimentally investigated the heat transfer and pressure drop during flowing air and passing water through a channel where wire mesh was embedded. It is reported that use of wire mesh inside the channel increased the heat transfer rate and smaller temperature gradient between the hot surface and fluid as air was passed through the channel was achieved. However, it is concluded that in terms of energy point of view, their method was not reasonable for heating the liquid, as the increase in the heat transfer couldn't compensate the pressure drop caused by wire meshes. Kurian et al. [59] experimentally compared the thermal performance of three heat exchangers which were plain copper tubes, copper tubes embedded in aluminium porous foam and copper tubes embedded in stainless steel wire mesh. The outlet temperature fluid and pressure drop were measured by passing air and water with different flow rates. It is reported that wire mesh heat exchangers had better overall thermal performance and it is more cost effective than use of metal foam. An experimental study on the effect of adding aluminium wire meshes to plain tube heat exchanger was performed by Fu et al. [60]. Three different porosities and wire diameter of aluminium mesh were examined. In general, it is found that the thermal performance of the heat exchanger was improved in presence of wire meshes. In addition, a very limited number of researchers have studied the melting process of PCMs integrated with wire mesh. Mustaffar et al. [61] experimentally investigated the melting process of Salt hydrate as the PCM which filled the void spaces of an aluminum mesh embedded in a rectangular enclosure. The melting process time was reduced by 14% in presence of the aluminum mesh. Shuja et al. [62] numerically studied the effect of using different geometries of metal mesh during the melting process of n-octadecane. Three different mesh geometries including triangular, rectangular, and hexagonal were examined. The results showed that triangular mesh geometry had the best heat transfer enhancement during melting process compare to the rectangular and hexagonal geometries. Regarding the thermal management of batteries, Wu et al. [63] conducted an experimental study on the thermal management of power batteries by integration of copper mesh and paraffin wax as the composite PCM. It is found that using the composite PCM resulted to better heat dissipation and a uniform temperature distribution. An experimental and numerical

study on the thermal management of lithium-ion batteries was performed by Azizi and Sadrameli [64]. In their work, Poly Ethylene Glycol 1000 (PEG100) and aluminum wire mesh are used as the composite PCM. The batteries were placed in a rectangular enclosure filled with composite PCM. The results indicated that use of composite PCM for the heat dissipation from batteries, surface temperature of the batteries can be significantly reduced which improves the performance and the operation life time of the battery. Wei and Malen [65] investigated the impact of the using spatially-enhanced metal mesh on the thermal performance of a LHTES system during meting and solidification processes. They [65] have concluded that although embedding uniformly structured metal mesh improved the heat transfer rate, the spatially- enhanced design of metal mesh depicted better performance. In this regard, comparing the performance of uniformly and spatially enhanced design showed that melting rate was 140% improved by the suggested spatially-enhanced design. According to the literature reviewed, no published work is identified regarding the use of metal mesh as the porous medium embedded inside a vertical cylindrical LHTES (C-LHTES) system which is the primary novelty of the present paper. In the present work, we have experimentally investigated the detailed melting process of n-octadecane with the melting temperature (T_m) of 28˚C, filled vertical cylindrical LHTES systems with the presence of copper wire mesh as the thermal enhancer. The cylindrical LHTES system was thermally insulated from the bottom and isothermally heated from its lateral walls. Effects of the displacing two different porosities of wire mesh inside the C-LHTES system on the temperature distribution, Nusselt number, total and local heat transfer rate, and rate of energy stored at three different isothermal condition including T_h= 38 ˚C, T_h= 48˚C, T_h= 58˚C were examined.

5.2 Experimental approach

A detailed information regarding the C-LHTES system, preparation of porous medium, and the experimental procedures is presented in this section.

5.2.1 C-LHTES system

A transparent Unthreaded Polyvinyl Chloride (UPVC) pipe with the total length of 33 cm, thickness of 6 mm, and inner diameter of 4.8 cm was used as the cylindrical enclosure. It should be mentioned that the reason of using UPVC pipe is due to its potential for operation in sudden temperature changes without causing any fracture due to thermal stress. Moreover, it was seen to have better machinability such as drilling and surface polishing. Initially, acrylic pipe was used as

the cylindrical enclosure, however, during the experimental procedures the C-LHTES system failed since several fractures appeared due to applying different temperatures to the wall of the enclosure.). The cylindrical UPVC pipe was vertically attached to a thick plastic plate with the thickness of 3 cm by using the specific cement for attaching UPVC material to plastics. The plastic plate acted as the thermal insulator at the bottom of cylindrical enclosure as well as the cap to seal one side of the UPVC pipe. As a result, one side of the UPVC pipe was closed while the other side was kept open to avoid any pressure on the top of the PCM during the melting process. To monitor the temperature distribution at the inner wall of UPVC pipe, eight T-type thermocouples from Omega attached to the inner wall of the UPVC pipe at different heights (i.e. 1 cm to 8cm from the bottom). In addition, to monitor the temperature profile at the center of the C-LHTES system, a thin acrylic rod (diameter= 3.23 mm) was installed in the center of the enclosure where four T-type thermocouples at different heights (i.e. 2 cm, 4 cm, 6 cm, and 8 cm from the bottom) were attached to it.

5.2.2 Composite PCM preparation

To prepare the composite PCM, 150 ml of n-octadecane ($CH_3(CH_2)_{16}CH3$) with the purity of 99% And the melting temperature (T_m) of 28˚C was used as the base PCM.The properties of n-octadecane with the purity of 99% is shown in Table.1.

Table.1. Thermophysical property of n-octadecane [66]

Thermophysical property	Value
Thermal conductivity (solid/liquid)	0.358/ 0.148 (W/m.K)
Specific heat (solid/liquid)	1934/ 2196 (J/Kg.K)
Density (solid/liquid)	865/ 770 (kg/m^3)
Kinematic viscosity	5×10^{-6} (m^2/s)
Latent heat of fusion	243.5 (KJ/kg)
Thermal expansion coefficient	9.1×10^{-4} (1/K)

At the next step, two sheets of copper meshes with different porosities and wire diameters having dimensions of 9 cm ᵡ 140 cm were rounded within the inner diameter of C-LHTES system. A

sample of the copper meshes and the physical properties of it is shown in Fig.1. and Table. 2 respectively.

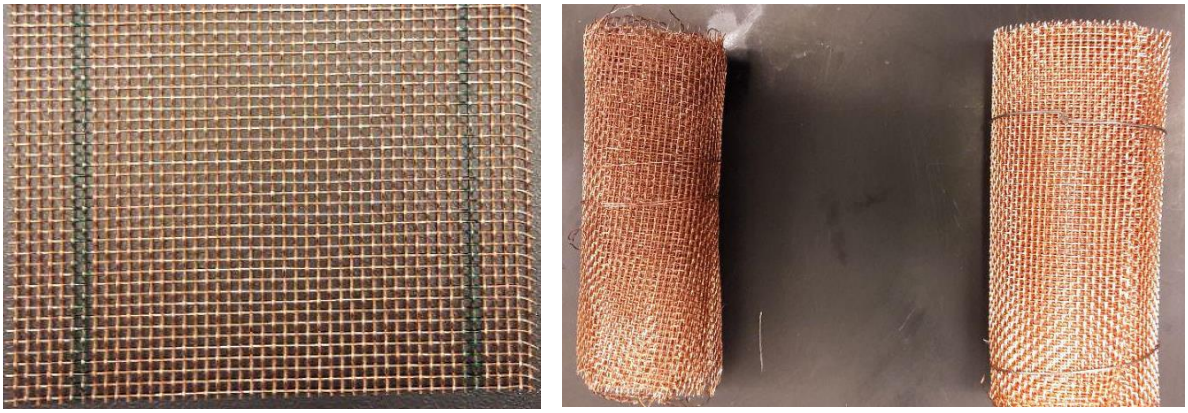

(a) (b)

Fig.1. A sample of the copper mesh used in the experiments: (a) flat copper mesh (b) rounded copper mesh

Table 2. Properties of copper mesh [67]

Property	Value
Thermal conductivity	401 (W/m.K)
Density	8960 (kg/m^3)
Specific heat	390 (J/Kg.K)

The C-LHTES system was initially filled with molten n-octadecane. The rounded copper meshes were placed inside the C-LHTES system separately. The increase in the height of the PCM due to displacing the copper meshes was recorded. According to the Eq. 1, the porosities of copper meshes were calculated as 87% and 75%.

$$\Phi = 1 - \frac{Solid\ volume\ of\ the\ copper\ mesh}{Total\ volume\ of\ the\ copper\ mesh} \quad (1)$$

5.2.3 Description of the Experimental setup

The experimental setup was consisted of C-LHTES system as it is discussed in section 2.1, an transparent acrylic tank with the dimensions of 30 cm X30 cmX30 cm filled with deionized water, a thermal regulator (model: HCTB-3020) equipped with circulating pump for providing the isothermal condition, and a 16 channel DAQ system connected to the T-type thermocouples. The thermal regulator was placed at one side of the acrylic water tank while the C-LHTES system was placed at the other side inside the water tank during the experiments. To prevent the possible effects of turbulent flow caused by the direct movement of water due to the operation of circulating pump, an acrylic barrier was placed between the circulating pump and the C-LHTES system. A 5 cm gap between the bottom of the acrylic water tank and the barrier was maintained to allow the water circulation. As a result, by checking the temperature distribution among different locations inside the acrylic water tank using T-type thermocouples, a uniform temperature distribution was seen. To decrease the heat losses between the acrylic water tank and the experimental environment, the acrylic water tank was insulated from its lateral walls. In addition, another water tank equipped with another thermal regulator (model: CR250WU) was used for solidification processes and maintaining an identical initial temperature of 25°C for different cases of the experiment. It should be noted that solidification at temperatures close to the melting point of a PCM, provides the advantages of less trapped air inside the PCM and avoiding the sub-cooling effect during early stages of the melting process. A photograph of the experimental setup is shown below in Fig.2.

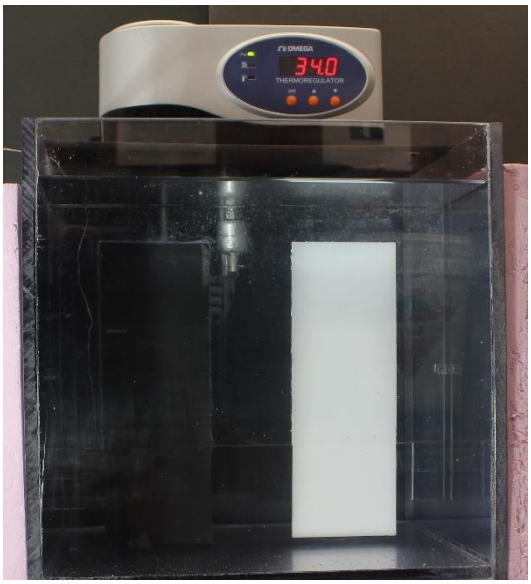

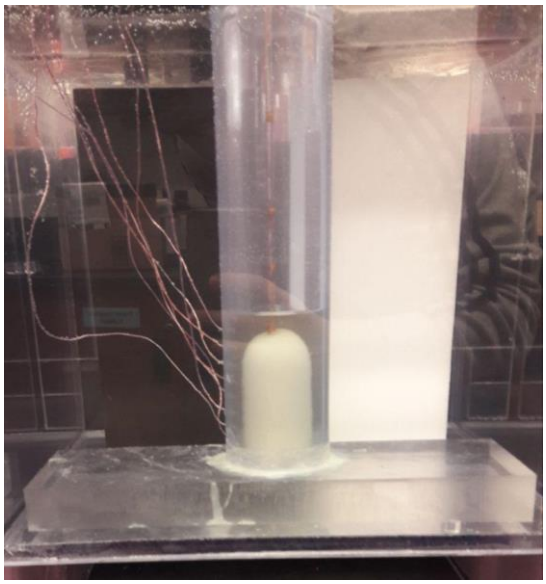

(a) (b)

Fig.2. A photograph of the experimental setup: (a) Omega thermal regulator placed in the acrylic water tank (b) C-LHTES system inside the acrylic water tank.

5.2.4 Experimental Procedure

The experimental procedures were carried out in different stages. The first set of experiments were conducted for the case using pure n-octadecane without embedding copper mesh. To do so, the C-LHTES system was maintained at the temperature of 25˚C for approximately 15 hours. After ensuring the uniformity temperature of 25˚C inside the solidified n-octadecane by monitoring the temperatures using installed T-type thermocouples, The C-LHTES was prepared to initiate the melting experiment. At this point, the temperature of the acrylic water tank was set to 38˚C, 48˚C, and 58˚C for different experimental stages. Two T-type thermocouples were attached inside the acrylic water tank to ensure the accuracy of the temperature inside the water of acrylic tank. After ensuring the uniformity of the temperature distribution inside the acrylic water tank, the C-LHTES system having the initial temperature of 25˚C was immediately placed inside the acrylic water tank with the temperatures of 38˚C, 48˚C, and 58˚C to initiate the melting process. The T-type thermocouples at the inner wall and the center of the C-LHTES system recorded the temperature distribution every 10 seconds until the end of the melting process and reaching to the thermal equilibrium condition. The same experimental steps were taken for the Th= 48 ˚C (20 ˚C above the melting point) and Th= 58 ˚C (30 ˚C above the Tm) with same initial temperature of 25 ˚C. The justification of selecting these temperature sets was due to having a proper difference with the melting temperature of the n-octadecane and the operation temperature limitation of the cement used to attach the UPVC pipe to the plastic plate. The second sets of experiment were conducted for the composite PCM (i.e. n-octadecane integrated with copper mesh) with the porosity of 87%. The same amount of n-octadecane was maintained inside the C-LHTES system and the rounded copper mesh was placed inside the molten n-octadecane. This offers the advantage of a fair comparison of thermal performance of C-LHTES system filled with the pure PCM and the composite PCM. The increase in height of the PCM inside the C-LHTES system by placing the copper meshes with porosity of 87% seen to be 3.8 mm. The amount of PCM inside the C-LHTES

system was checked every time before starting the next set of experiments. The C-LHTES system was placed in the water tank having temperature of 25 ˚C for the solidification process. Again, the C-LHTES system was kept inside the bath for approximately 15 hours. Then the melting experiment was performed for the Th= 38, 48, and 58 ˚C. The last sets of experiments were conducted for the composite PCM having porosity of 75%. The copper mesh having porosity of 87% from the previous experiment was taken out and instead of that copper mesh with porosity of 75% was placed inside the C-LHTES system filled with molten n-octadecane. At this time, the amount of n-octadence inside the C-LHTES was checked to be the same as previous sets of experiment. The same experimental procedure was followed for this case. It should be motioned that each set of experiments was repeated at least twice to ensure the reliability of the results obtained from experiments.

5.3 Results and Discussion

In this section, the results obtained from experimental work are discussed. The results are included as temperature variations, local heat transferred, the trend of surface averaged Nusselt number, the heat flux, and stored energy, which are presented in time domain and SteχFo dimensionless number.

5.3.1 Temperature variations

In this section, the temperature distributions recorded by the thermocouples located at the inner wall and center of the C-LHTES system during the melting process are discussed. For the sake of brevity, only the temperature distributions for the set of experiments subjected to T_H = 48˚C are discussed since a similar behavior was seen for the experiments subjected to T_H = 38˚C and 58˚C. Figure 4 shows the temperature profiles recorded by the eight calibrated T-type thermocouples installed at the inner wall of the C-LHTES system. To have a fair comparison, the initial temperature of the n-octadecane and the isothermal boundary temperature for all of the following selected experiments (i.e. PCM without copper mesh, composite PCMs with the porosities of 87% and 75%) were maintained at 25˚C and 48˚C, respectively.

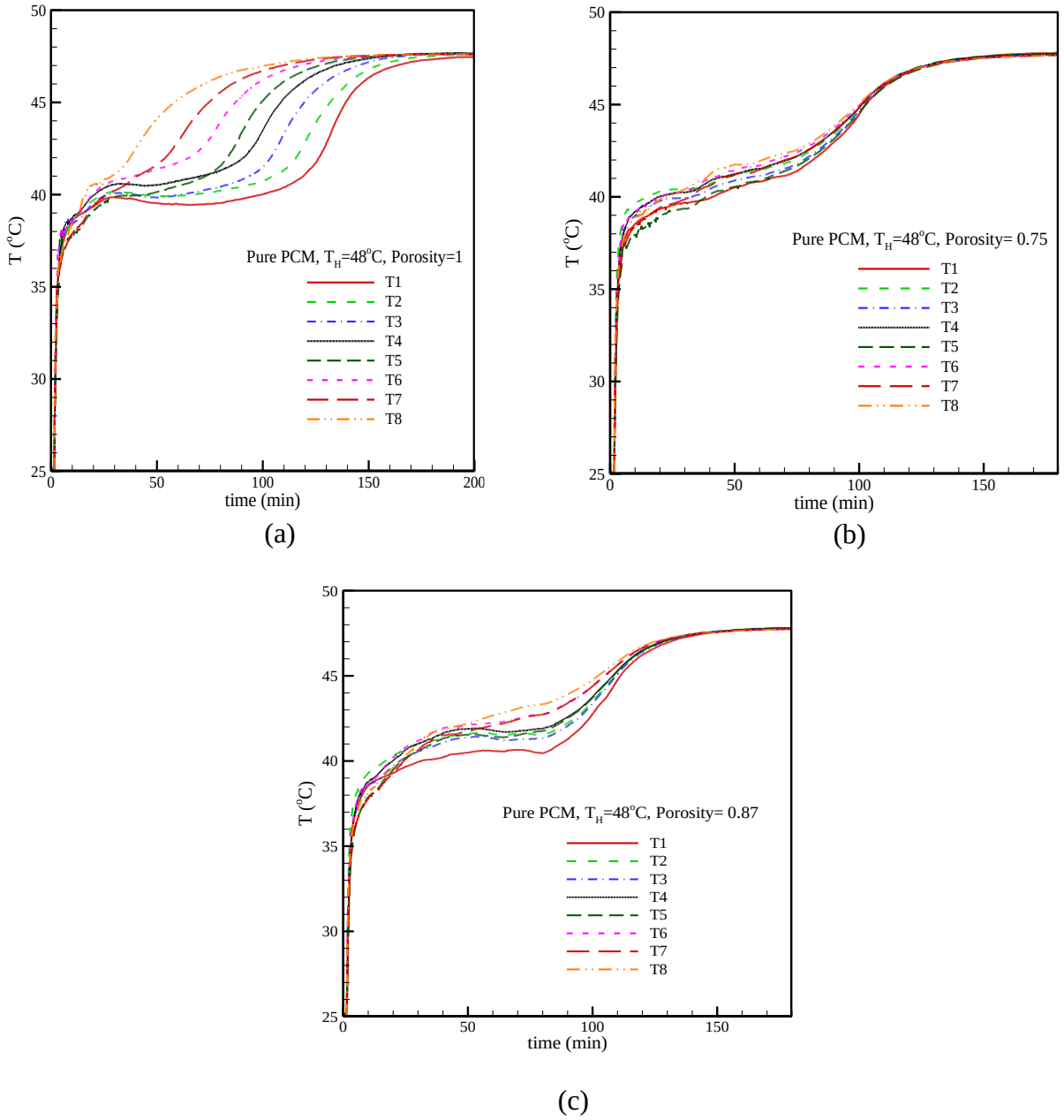

Fig. 3. Temperature variations recorded by the thermocouples attached to the inner wall of C-LHTES system and $T_H = 48^{\circ}C$: (a) without copper mesh, (b) Composite PCM ($\varepsilon = 0.75$), and (c) Composite PCM ($\varepsilon = 0.87$).

As it can be seen from Fig. 3(a) to Fig. 3(c), at the early stages of the melting process (i.e. up to 10 minutes), there is a sharp linear increase in the temperatures profile which is as a result of near wall conduction dominated melting process and heat transfer. From this point onward, natural convection appeared as the buoyancy force overcame the viscous force in the liquid PCM. As a result, the heat transfer occurred by a mixed regime of convection and conduction and convection dominant at the last stages of melting process. The rate of increase in the temperatures recorded by T-type thermocouples degrades due to the decrease in the temperature gradient between solid PCM and hot isothermal wall. This pattern continues until thermal equilibrium is reached. Comparing the experiment without copper mesh (see Fig. 3(a)) with the experiments which composite PCMs (see Fig. 3(b) and Fig. 3(c)) were examined, reveals a uniform temperature distribution along the C-LHTES system that resulted by using copper mesh as the porous medium embedded inside the C-LHTES system. To assist the discussion, Table 1 compares the temperatures recorded by the thermocouple located at the lowest height of the inner wall (i.e. T_{C1} and H= 1 cm) and the thermocouple located at the highest height of the inner wall (i.e. T_{C8} and H= 8cm) at two selected times of 50 and 100 minutes.

Table 3: Temperature values at two selected times and $T_H = 48^{\circ}C$.

	50 min			100 min		
	T_{C1}	T_{C8}	ΔT	T_{C1}	T_{C8}	ΔT
Pure PCM (ε =1)	39.5˚C	44.1˚C	4.6˚C	40˚C	47˚C	7˚C
Composite PCM (ε = 0.75)	40.5˚C	41.7˚C	1.2˚C	44.5˚C	45˚C	0.5˚C
Composite PCM (ε = 0.87)	40.5˚C	42.2˚C	1.7˚C	42.7˚C	44.8˚C	2.1˚C

As it is shown in Table 1, by embedding the copper mesh in the C-LHTES system, heat is transferred through the copper mesh along the C-LHTES, which resulted to a uniform temperature distribution in the PCM as it was also reported Mancin et al. [21]. This effect is enlarged by using composite PCM having $\varepsilon = 0.75$, which is due to a larger effective thermal conductivity than using composite PCM with $\varepsilon = 0.87$. As it can be seen from Fig. 3(a) to Fig. 3(c), comparing the temperatures at the top of the C-LHTES system (i.e. T_{C7} and T_{C8}) at the times before reaching to the thermal equilibrium shows that the onset of natural convection is delayed due to the obstacles in upward current of the molten PCM caused by using copper mesh. This can be identified by

lower temperatures recorded by T_{C7} and $T_{C8.}$ However, in overall, the thermal equilibrium was reached earlier by using composite PCM as the thermal conductivity of PCM was enhanced. This is shown in Table. 4. below.

Table 4: Time required to reach the thermal equilibrium for pure PCM and composites PCMs having $\varepsilon = 0.75$ and 0.87, $T_H = 48^{\circ}C$.

T_H	Pure PCM (ε =1)		Composite PCM (ε = 0.75)		Composite PCM (ε = 0.87)	
	Wall	Center	Wall	Center	Wall	Center
38°C	280 min	275 min	235 min	235 min	245 min	250 min
48°C	185 min	180 min	135 min	140 min	150 min	155 min
58°C	160 min	145 min	110 min	115 min	115 min	120 min

Figure 4 shows the reported temperatures recorded by four T-type thermocouples at the center of the C-LHTES system during the melting process. Comparison of Fig 4(a) with Figs. 4(b) and 4(c) shows that the discrepancies in temperatures are decreased by using composite PCM that is resulted by a uniform temperature distribution along with the C-LHTES system. In addition, as it is shown in Table.4, the time required for reaching the thermal equilibrium at the center of the C-LHTES system was also decreased due to embedding copper mesh inside the C-LHTES systems. By monitoring the temperature distributions reported by the thermocouple located at the lowest height of the rod installed at the center of C-LHTES systems (i.e. T_{C1}, H= 2cm), it can be identified that the melting process at that location occurred at 100 minutes for pure PCM and at 90 minutes after initiating the melting process for the experiments which composite PCMs were used. From this point onward, there is a sharp increase in the temperature reported by T_{C1} for composite PCMs, which proves a faster melting process due to embedding copper mesh inside the C-LHTES system. The ratio of the increase in the temperature profile reported by T_{C1}, is enlarged when composite PCM having $\varepsilon = 0.75$ was used since a larger overall thermal conductivity was reached.

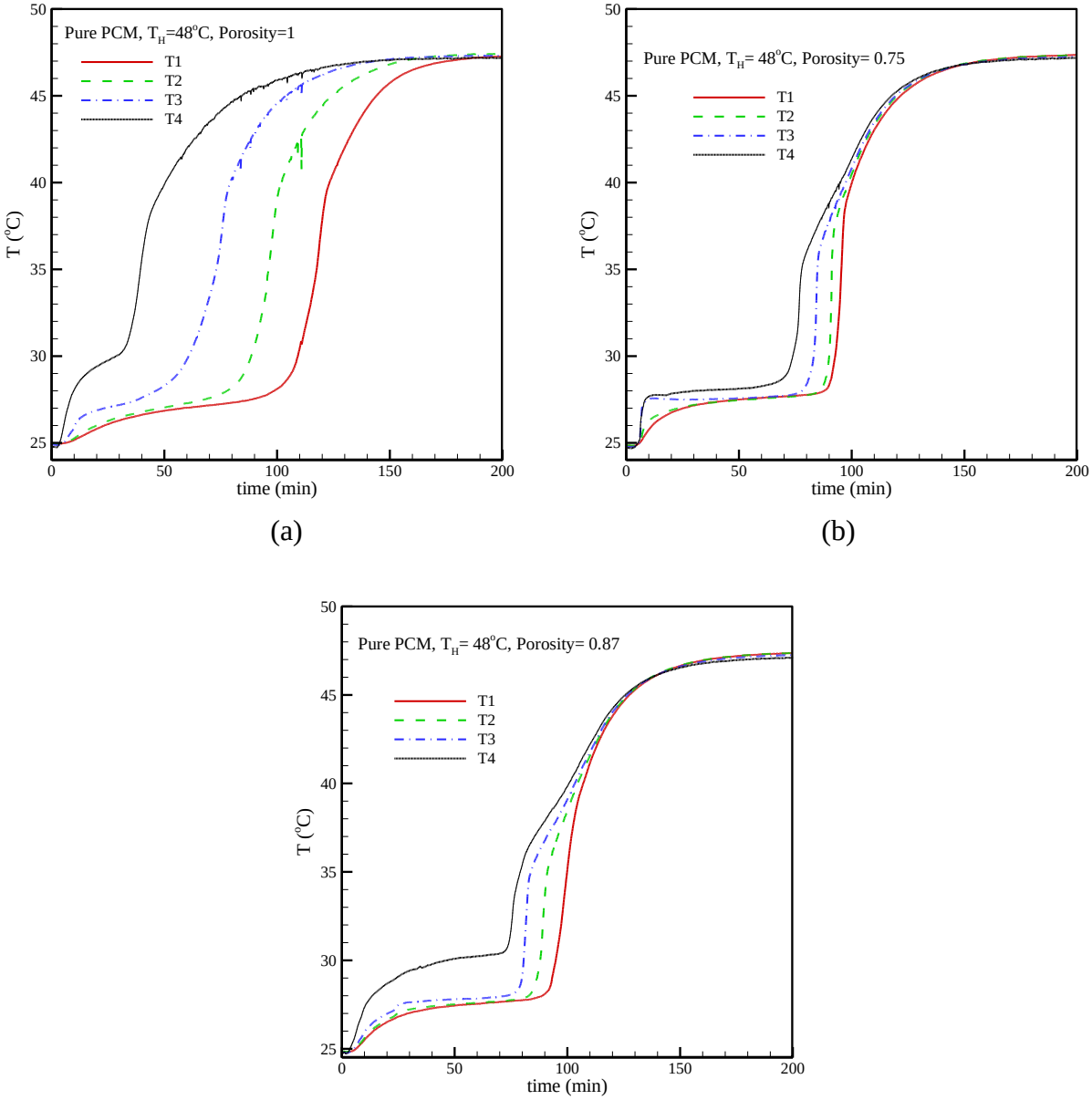

Fig. 4. Temperature variations recorded by the thermocouples located at the center of C-LHTES system and TH= 48˚C: (a) Without copper mesh, (b) Composite PCM (ε = 0.75), and (c) Composite PCM (ε = 0.87).

Figure 5 presents the temperature distributions during melting process for Composite PCM having $\varepsilon = 0.75$ at three different operation conditions including $T_H = 38^{\circ}C$, $48^{\circ}C$, and $58^{\circ}C$. In this regard, Fig. 5(a) depicts the temperature profile at the inner wall of C-LHTES system and Fig. 5(b) shows the temperature distribution at the center of C-LHTES system.

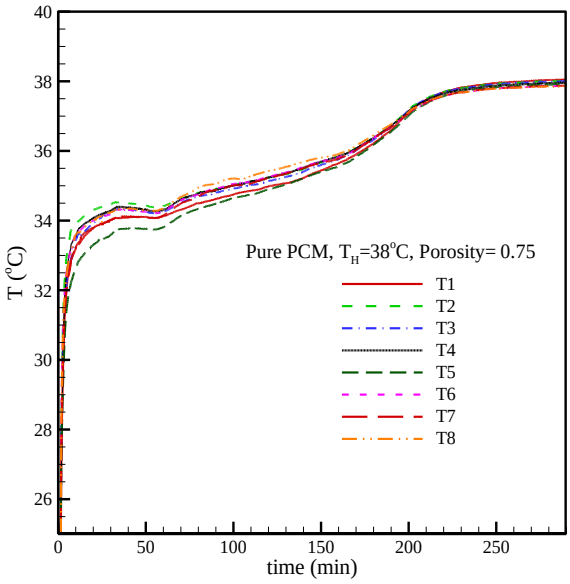

(i)

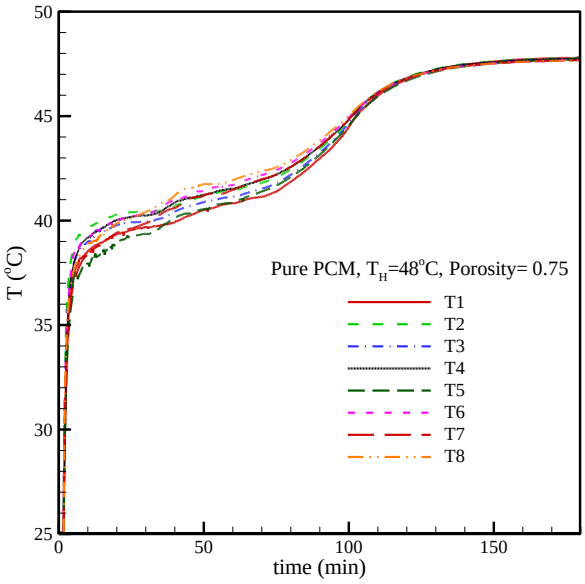

(ii)

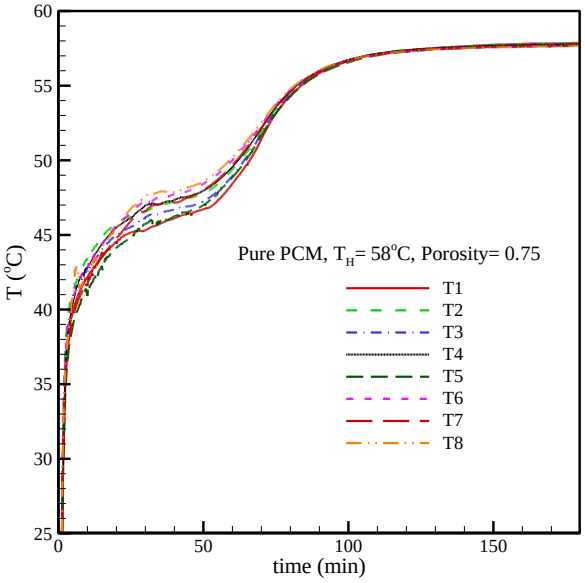

(iii)

Fig. 5(a). Temperature variations recorded by the thermocouples located at the inner wall of C-LHTES system for composite PCM with ε = 0.75 at three different operating conditions: (i) T_H= 38°C, (ii) T_H= 48°C, and (iii) T_H= 58°C.

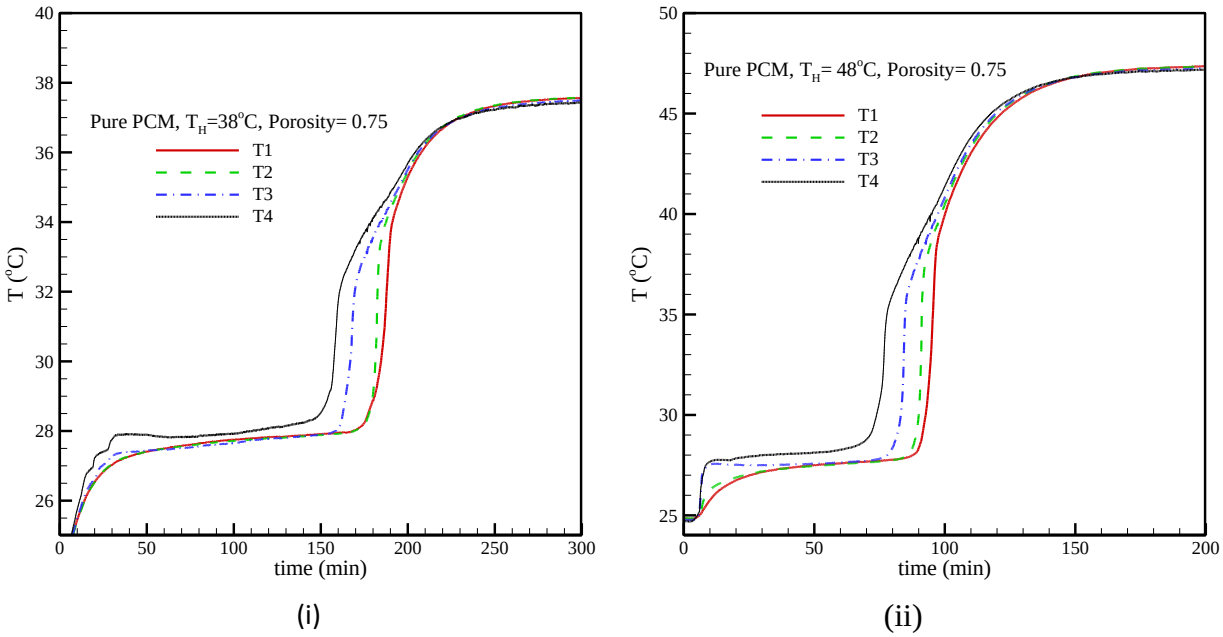

(i) (ii)

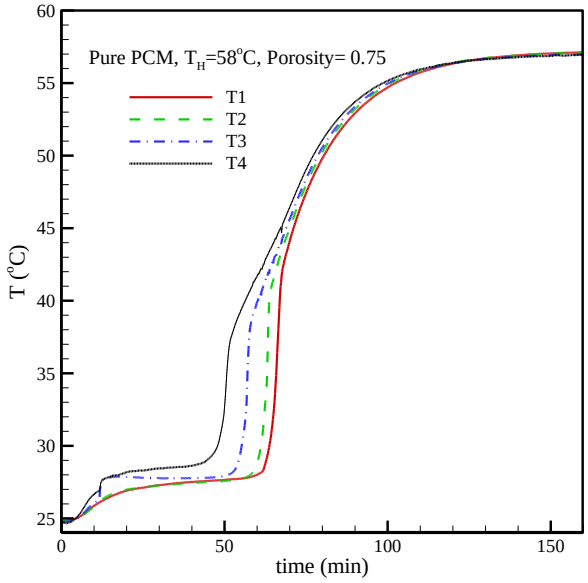

(iii)

Fig. 5(b). Temperature variations recorded by the thermocouples located at the center of C-LHTES system for composite PCM with $\varepsilon = 0.75$ at three different operating conditions: (i) T_H= 38˚C, (ii) T_H= 48˚C, and (iii) T_H= 58˚C.

As it can be seen from Figs. 5(a) and 5(b), the temperature of isothermal boundary wall significantly decreased the required time for complete melting process and reaching the thermal equilibrium condition. For instance, the required time to reach the thermal equilibrium was shortened by 42% by increasing the temperature of the isothermal wall from T_H= 38˚C to T_H= 48˚C, and 53% for the experiment which T_H = 58˚C was set. This improvement in melting process is due to the higher heat transfer rate between cold PCM and isothermal wall due to the larger temperature gradient. The stable temperature of the PCM is slightly lower than the isothermal wall temperature for T_H = 48˚C and 58˚C due to the increase in the heat losses from the C-LHTES system and the environment. In overall, a similar pattern with a sharper increase in the temperature for T_H= 58˚C can be seen.

5.3.2 Local heat transfer

Figure 6 presents the local heat transferred from hot water bath through the inner wall of the C-LHTES system in the form of conduction at eight different locations where thermocouples are installed. Figure 6(a) presents some selected results to show the effect of embedding copper mesh at different porosities (i.e., ε =75% and 87%) at T_H = 58˚C. At the beginning of the melting process, the magnitude of the heat transfer is high due to the large temperature difference between the hot isothermal wall and the cold PCM. The heat is transferred in form of conduction at the early stages of melting (i.e. up to 10 minutes) where the local heat transfer profile is parallel to y-axis of the plots below. After approximately 10 minutes of the experiment, the thin layer of molten PCM adjacent to the wall of the C-LHTES system started to move upward due to the convection heat transfer regime. This can be identified by the change in the slope of the q-t plots. As time advanced, the local heat transfer decreased due to the decrease in the temperature difference between the hot isothermal wall and the molten PCM. The local heat transfer decreases to its minimum value by the end of melting process and reaching to the thermal equilibrium condition. As it is discussed in

Section 3.1, using composite PCM resulted in a uniform temperature distribution inside the C-LHTES system. Distributing heat uniformly inside the C-LHTES system led to a uniform local heat transferred through the PCM as it is depicted in Fig. 6a(ii) and Fig. 6a(iii). As a result of that, the thermal equilibrium condition is reached faster for the experiments with composite PCM. The local heat transfer distribution is more uniform when the composite PCM having $\varepsilon = 0.75$ was examined.

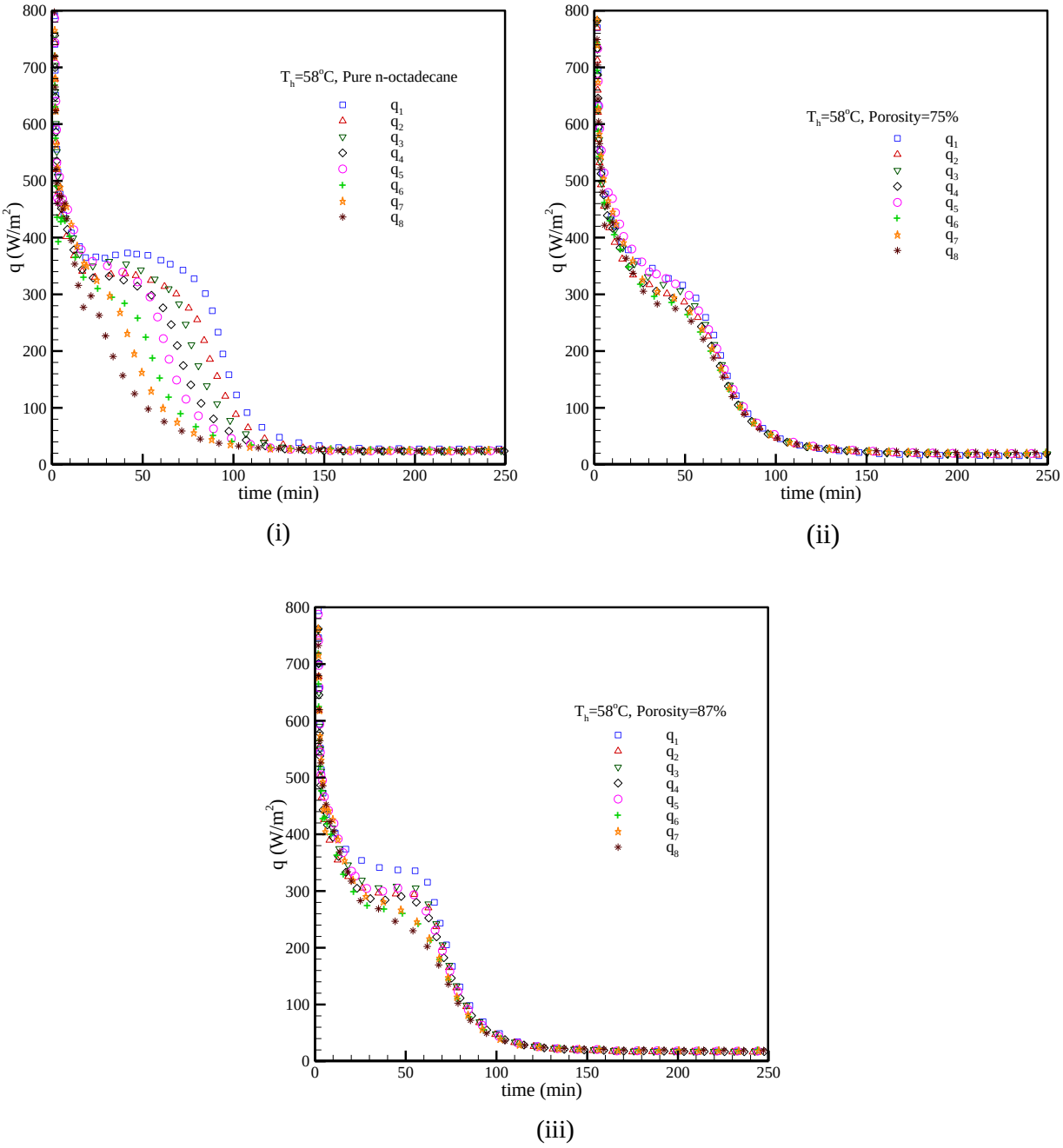

(i)

(ii)

(iii)

Fig. 6(a). Trend of local heat transferred through the inner wall of C-LHTES system at T_H= 58°C: (i) Pure PCM, (ii) Composite PCM (ε = 0.75), and (iii) Composite PCM (ε = 0.87).

Fig. 6(b) presents the effect of different isothermal wall temperatures (T_H) on the trend of local heat transferred. As it can be seen from Fig. 6b(i to iii), the magnitude of the local heat transfer increases by increasing the T_H . For instance, the magnitude of local heat transfer was increased by approximately 74% and 147% by increasing T_H= 38°C to 48°C and 58°C, respectively. As a result, the melting process was shortened.

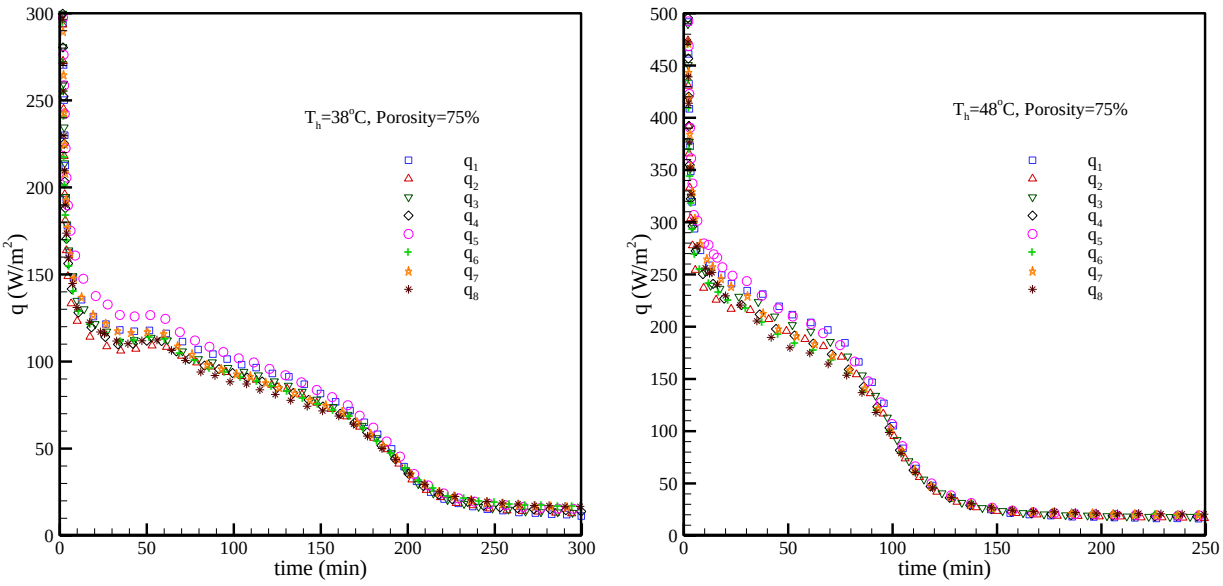

(i) (ii)

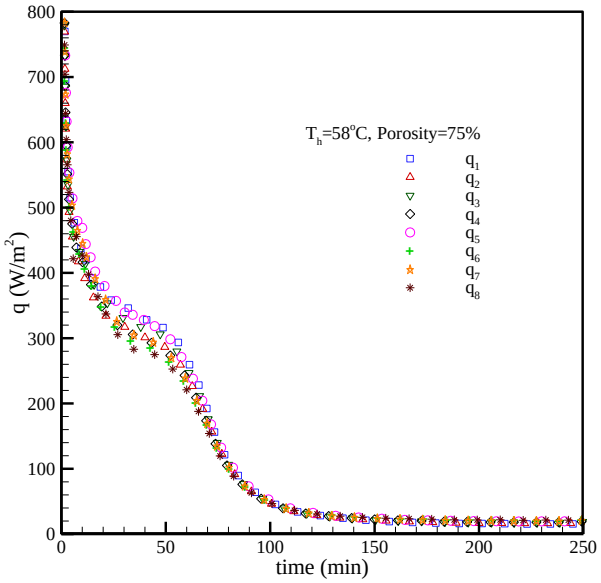

(ii)

Fig. 6(b). Trend of local heat transferred through the inner wall of C-LHTES system for Composite PCM having $\varepsilon = 0.75$ at three different T_H: (i) T_H= 38°C, (ii) T_H= 48°C, (iii) T_H= 58°C.

5.3.3 Surface averaged Nusselt number

The trend of surface averaged Nusselt number (Nu) for pure n-octadecane, composite PCM with porosity of 87%, and the composite PCM with porosity of 75% are presented in Fig. 7. Figure 7(a) presents the trend of surface averaged Nusselt number for the set of experiments performed with pure n-octadecane (i.e. without copper mesh). At the initial stages of the melting process, the conduction heat transfer dominated the melting process. As a result of that, a thin layer of liquid PCM parallel to the lateral walls appeared. The thermal resistance of this thin molten layer is relatively low which results to a high magnitude of Nusselt number and heat transfer rate due to the large temperature difference between hot lateral walls and cold solid PCM. As time furthered, the temperature gradient decreased which caused a sharp drop in the Nu number. At this moment, a change in the slope of the magnitude of Nussselt is seen which is due to appearance of the convection regime. As melting process furthered, natural convection became the dominant regime of the heat transfer, which can be identified by another change in the slope of Nusselt number. At the last stages of the melting process, the temperature gradient degraded significantly until thermal equilibrium was reached which resulted to a decrease in the magnitude of Nu number. The increase

in the temperature of acrylic water tank from 38 ˚C to 48 and 58 ˚C resulted to a faster melting process and thermal equilibrium condition. An almost similar behaviour can be seen for the composite PCM having porosity of 87% and 75%.

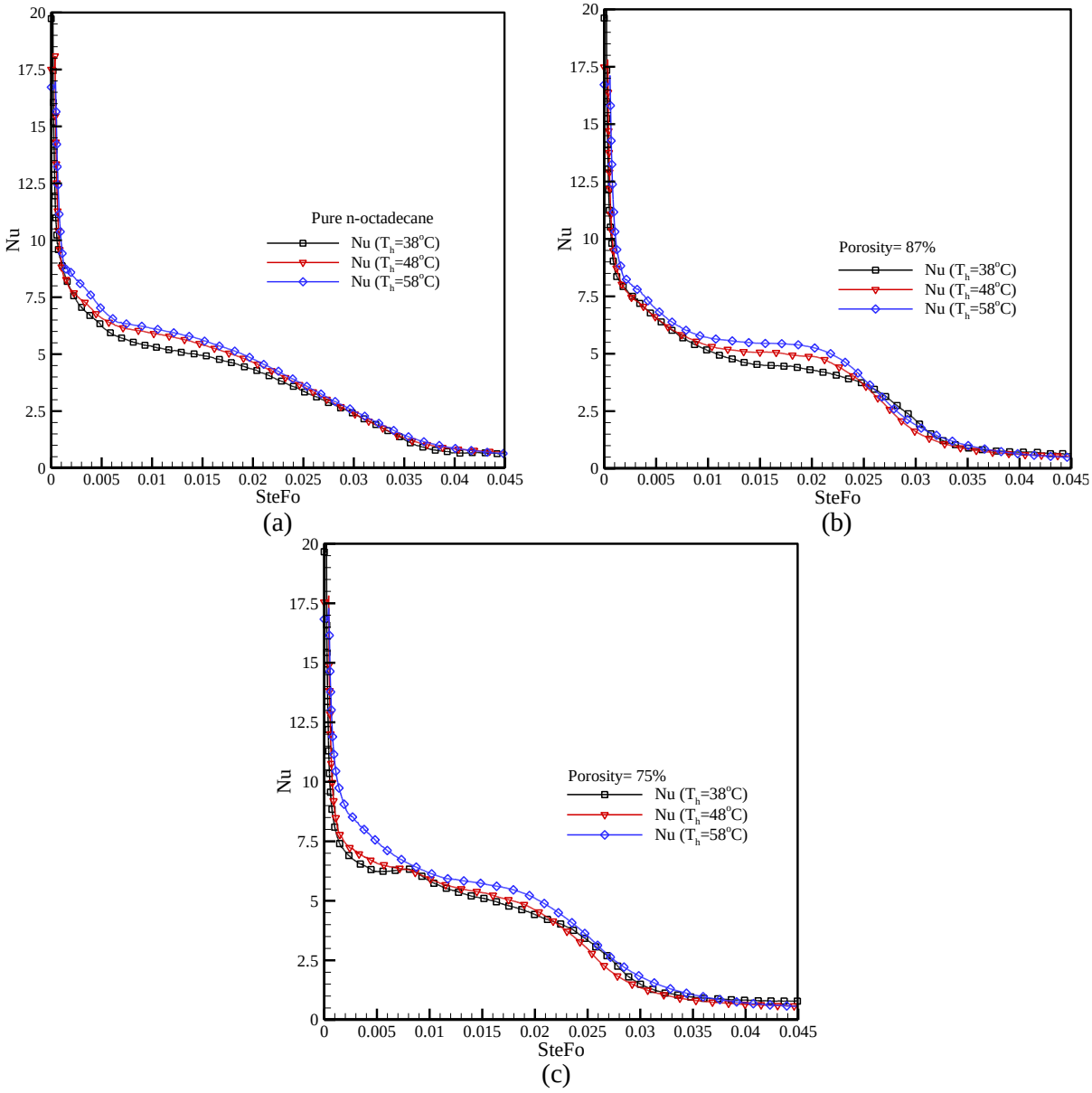

Fig.7. Trend of surface averaged Nu number for: (a) pure n-octadecane , (b) composite PCM with porosity of 87% , (c) and composite PCM with porosity of 75% .

5.3.4 Energy stored

In this section, the stored energy inside the C-LHTES system is presented. Figures 8(a) and 8(b) present the stored energy in the C-LHTES system for the case using pure n-octadecane. At the early stages of the melting process, the rate of the increase in stored energy is high due to the large temperature gradient between cold PCM and hot lateral walls. As time advances, the rate of the stored energy decreased due to the degradation of the temperature gradient until it reaches to its maximum value and become saturated. As it can be seen figures 8(a) and 8(b), by increasing the T_h, the amount of energy increases which is as a result of higher heat transfer rate. A identical pattern can be seen for composite PCMs as shown in figures 8(c) -8(f).

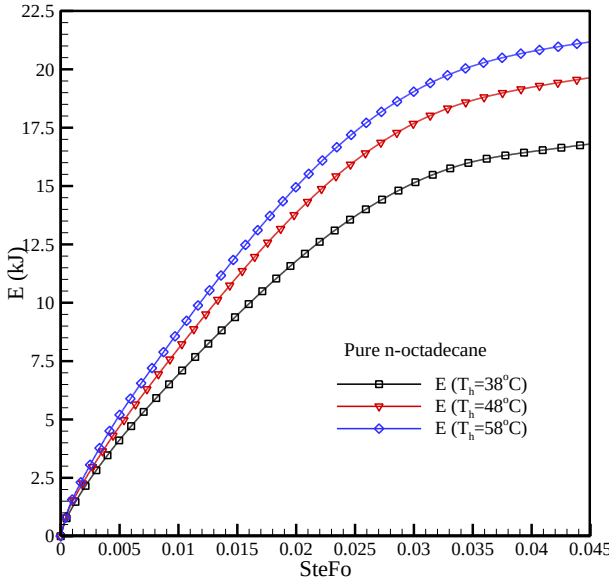

(a)

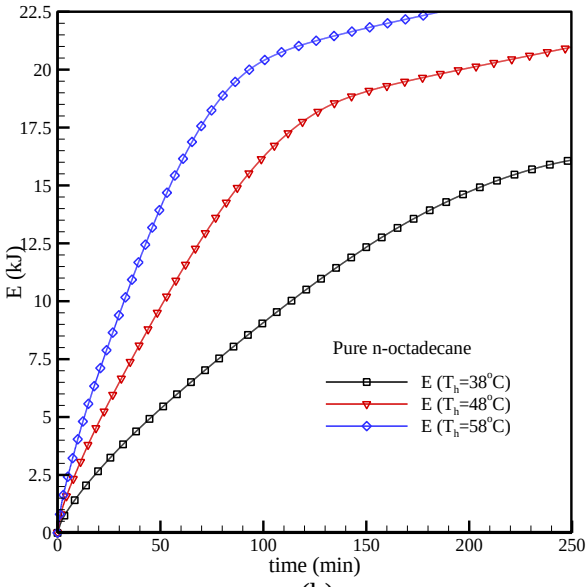

(b)

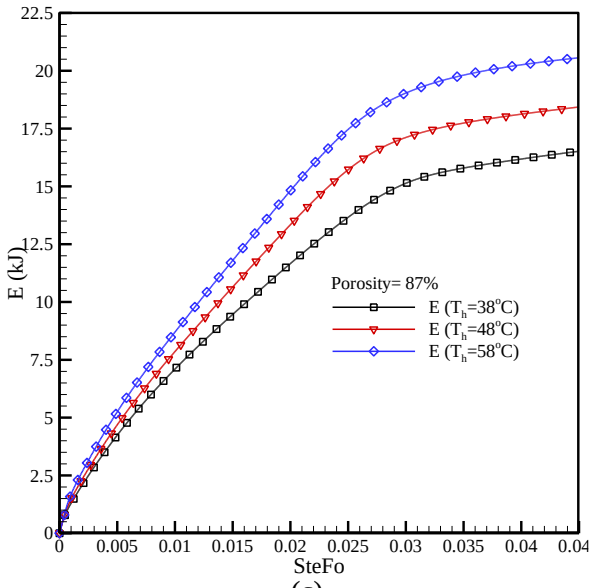

(c)

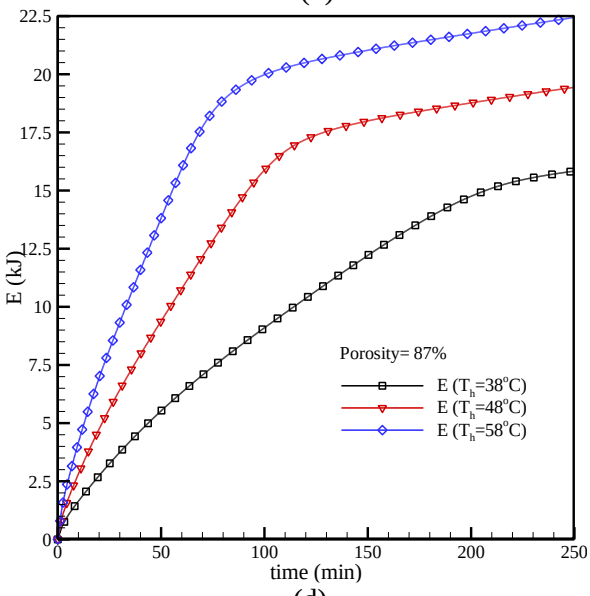

(d)

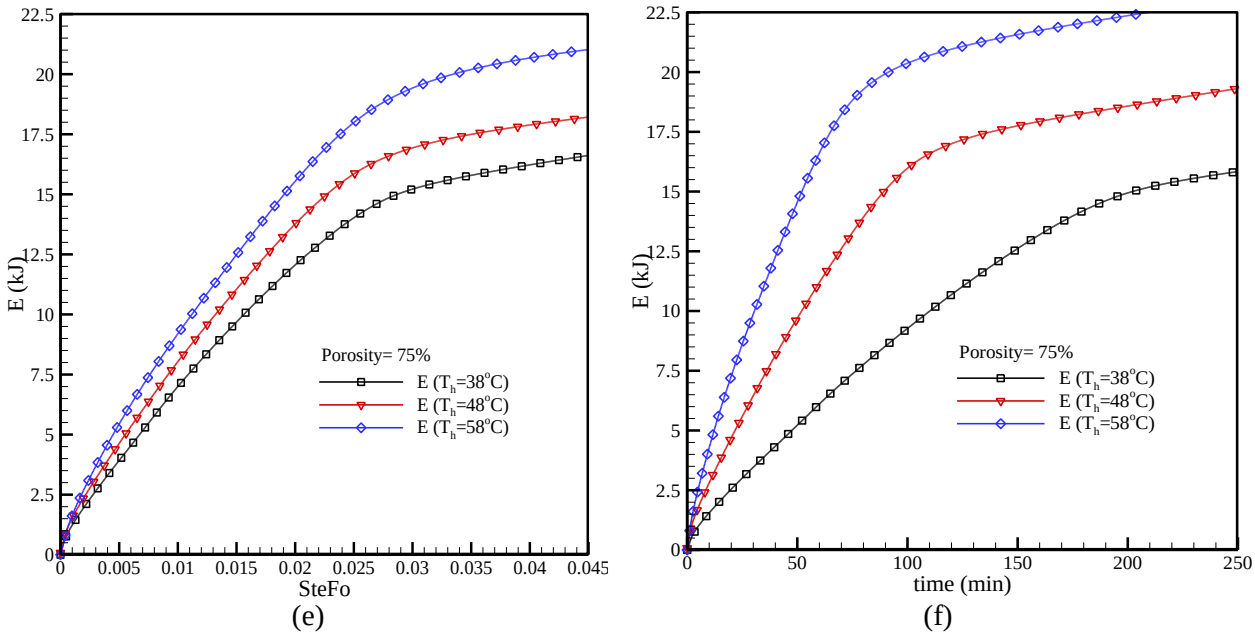

Fig.8. Energy stored for pure n-octadecane ((a) and (b)), composite PCM with porosity of 87% ((c) and (d)), and composite PCM with porosity of 75% ((e) and (f)).

5.3.5 Trend of the heat transferred

Figure 9 presents the heat transferred through the C-LHTES system during the melting process. As it is discussed earlier, the heat transfer rate is high at the early stages of the melting process where its enlarged for the cases which higher T_h was applied. The same as trend of Nu number discussed in section 3.3, a sharp drop in the magnitude of (Q) can be seen at the initial stages of the melting process where conduction dominated the heat transfer process. As time furthered, the buoyancy force overcame the vicious force that caused an upward flow of molten PCM. As a result of that, natural convection appeared and started to be grown. Hence, at this period of time, heat transferred was occurred by mixed regime of conduction and convection, which can be distinguished from the change in the slope of Q-t curve. As melting process advanced, the melting process was dominated by natural convection as it can be seen from another change in the slope of the Q-t. The heat transfer decreased to its minimum value due to the degradation of the temperature gradient between hot lateral walls and the warm molten PCM. The heat transfer rate

remains constant at its minimum value as the thermal equilibrium condition was achieved. The trend of heat transfer is approximately similar to the cases, which composite PCM was used.

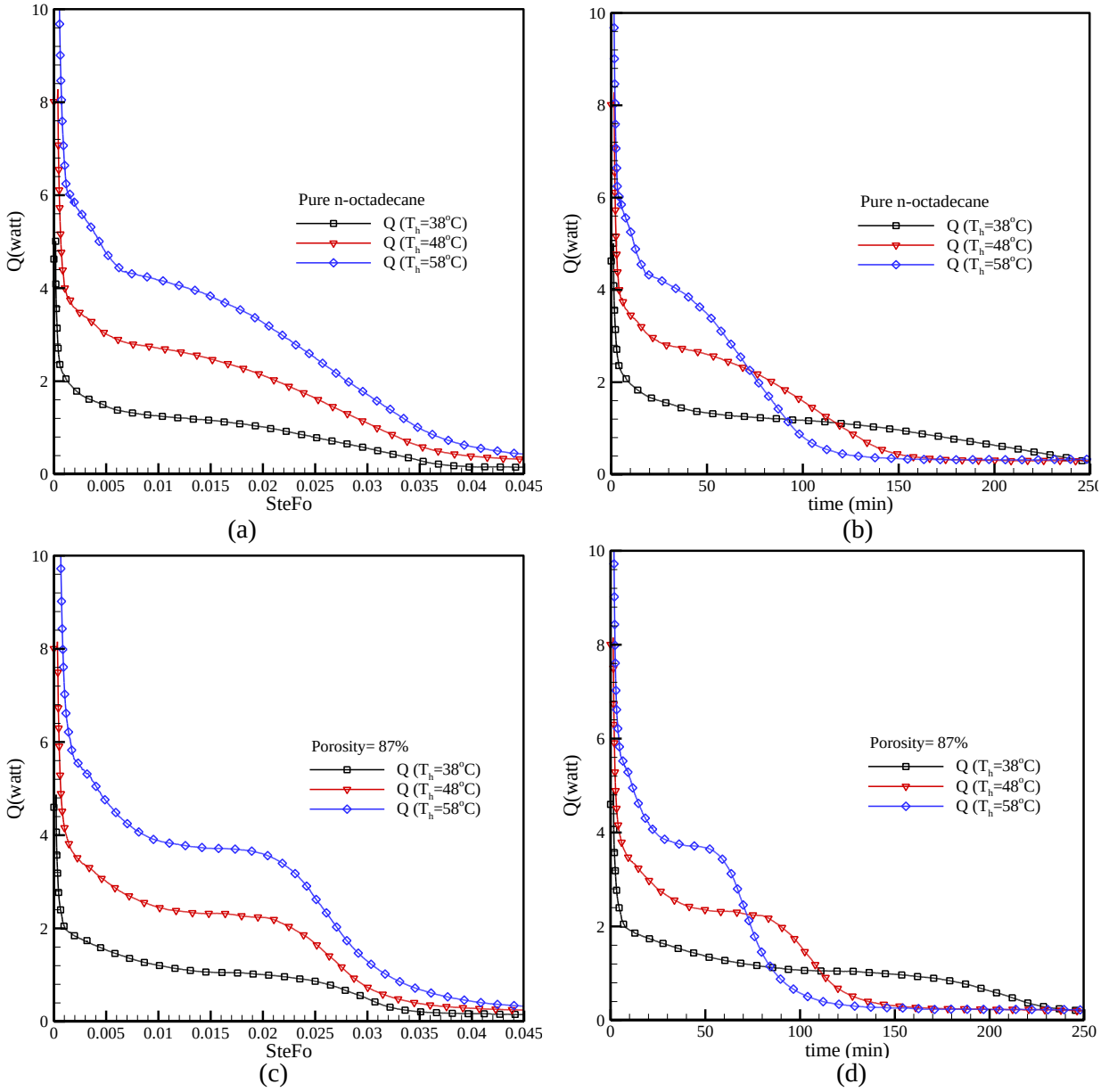

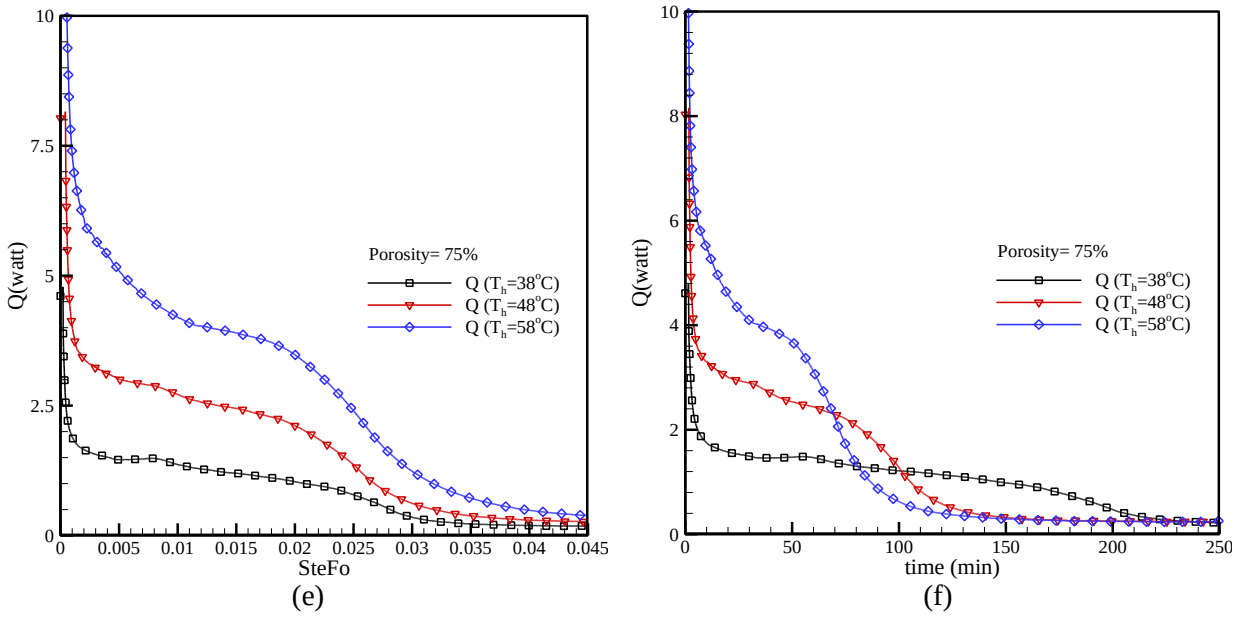

Fig.9. Trend of heat transfered for pure n-octadecane ((a) and (b)), composite PCM with porosity of 87% ((c) and (d)), and composite PCM with porosity of 75% ((e) and (f)).

5.4 Conclusion

Several sets of experiment were conducted to investigate the performance of a C-LHTES in presence of copper mesh as the porous medium. The C-LHTES system was subjected to three different temperatures of the acrylic tank (i.e. 38°C, 48 °C, and 58°C) to initiate the melting process. The temperature distribution recorded by T-type thermocouples were used to calculate the stored energy, surface averaged Nusselt number and heat transferred. At the beginning of the melting process the magnitude of the Nusselt number and heat transferred was seen to be high due to large temperature gradient. In addition, the rate of energy stored was high at the initial stages of the melting process. As time furthered, there was a decrease in the magnitude of the Nusselt number, heat transferred and the ratio of energy stored until a steady state condition was reached by the thermal equilibrium condition.

Chapter 6

Conclusions and Future Work

6.1 Conclusions

The thermal performance of a cylindrical LHTES system enhanced with nanoparticles and porous material was numerically and experimentally studied in this thesis. Different PCMs with different phase change temperature including (i) coconut oil, (ii) RT-35, and (iii) n-octadecane were used in this investigations. The highlights of this research are summarized as follows:

(i)The melting process inside the cylindrical LHTES which was subjected to isothermal boundary condition was dominated by conduction heat transfer at the initial stages. As melting process progressed, the buoyancy force overcame the viscous force, which leaded to an upward flow of the molten PCM/nano-PCM. This was the starting point that natural convection appeared and heat transfer occurred by a mixed regime of convection and conduction. After a while, natural convection dominated the melting which was identified by a significant change in the shape (i.e. an inverted paraboloid was seen) of the remaining solid PCM/nano-PCM.

(ii) An insignificant improve in the melting rate was seen by using nano-PCM at the early stages of melting process. However, as melting process progressed, the melting rate was enhanced by dispersing nanoparticles into the PCM. In overall, using nano-PCM did not show a significant improvement on the melting rate. The reason of that could be due to the increase in the viscosity of PCM by dispersing nanoparticles which degrades the natural convection. In addition, the volume/weight fraction of nanoparticles is limited to the sedimentation issue in the experimental works. Moreover, using the nano-PCM degraded the amount of energy stored inside the C-LHTES system due to the changes in the PCM's properties. To put everything in a nutshell, dispersion of nanoparticles is only suggested for the cases where a thin layer of PCM is existed.

(iii) Displacing of the copper mesh into the PCM's container showed a significant improvement on the thermal performance of the C-LHTES system. However, it should be mentioned that a portion of the container's volume is occupied by the porous medium. As a result of that, less amount of PCM can be used, which means less thermal energy would be stored inside the C-LHTES system.

6.2 Future Work

In terms of fundamental side, future work will focus on the optimization of the geometry of a LHTES system which can enhance the heat transfer rate. In addition, use of extended surfaces such as metal fins would be considered. In terms of the applied side, the design and development of large-scale LHTES systems that can be installed in buildings for thermal management applications and in solar thermal power plants for storing the thermal energy will be conducted.

References

References for Chapter 2

[1] S.L. Batley, D.Colbourne, P.D. Fleming, P. Urwin, Citizen versus consumer: challenges in the UK green power market, Energy Policy, 29 (2001) 479-487.

[2] S. Fuss, J.A. Johasson, J. Szolgayova, M. Obersteiner, Impact of climate policy uncertainty on the adoption of electricity generating technologies, Energy Policy, 37 (2009) 733-743.

[3] D. Georgakellos, Impact of a possible environmental externalities internalization on energy prices: the case of the greenhouse gases from the Greek electricity sector, Energy Econ, 32 (2009) 202-209.

[4] A Longo, A Markandya, M. Petrucci, The internalization of externalities in the production of electricity: willingness to pay for the attributes of a policy for renewable energy Ecol Econ, 67 (2008), pp. 140-152.

[5] N.S. Dhaidan, J.M. Khodadadi, Melting and convection of phase change materials in different shape containers: A review, Renewable and Sustainable Energy Reviews, 43 (2015) 449-477.

[6] N.S. Dhaidan, Nanostructures assisted melting of phase change materials in various Cavities, Applied Thermal Engineering, 111 (2017) 193–212.

[7] Z. Khan, Z. Khan, A. Ghafoor, A review of performance enhancement of PCM based latent heat storage system within the context of materials, thermal stability and compatibility, Energy Conversion and Management 115 (2016) 132–158.

[8] B. Zalba, J. Marın, L.F. Cabeza, H. Mehling, A review on thermal energy storage with phase change materials: heat transfer analysis and applications, Applied Thermal Engineering, 23 (2003) 251–283.

[9] N.S. Dhaidan, J.M. Khodadadi, T. A. Al-Hattab, S.M. Al-Mashat, Experimental and numerical investigation of melting of phase change material/nanoparticle suspensions in a square container subjected to a constant heat flux, International Journal of Heat and Mass Transfer, 66 (2013) 672–683.

[10] Y. Zeng, L. Fan, Y. Xiao, Z. Yu, K. Cen, An experimental investigation of melting of nanoparticle-enhanced phase change materials (NePCMs) in a bottom heated vertical cylindrical cavity, International Journal of Heat and Mass Transfer, 66 (2013) 111-117.

[11] L. Fan, J.M. Khodadadi, Thermal conductivity enhancement of phase change materials for thermal energy storage: A review, Renewable and Sustainable Energy Reviews, 15 (2011) 24–46.

[12] N. I. Ibrahim, F. A. Al-Sulaiman, S. Rahman, B. S. Yilbas, A. Z. Sahin, Heat transfer enhancement of phase change materials for thermal energy storage applications: A critical review, Renewable and Sustainable Energy Reviews, 74 (2017) 26–50.

[13] M. Jourabian, M. Farhadi, A. Rabienataj Darzi, Constrained ice melting around one cylinder in horizontal cavity accelerated using three heat transfer enhancement techniques, International Journal of Thermal Sciences, 125 (2018) 231–247

[14] J.M. Khodadadi, L. Fan, H. Babaei, Thermal conductivity enhancement of nanostructure-based colloidal suspensions utilized as phase change materials for thermal energy storage: A review, Renewable and Sustainable Energy Reviews, 24 (2013) 418–444.

[15] X. Zhang, X. Chen, Z. Han, W. Xu, Study on phase change interface for erythritol with nano-copper in spherical container during heat transport, International Journal of Heat and Mass Transfer, 92 (2016) 490–496.

[16] R. Hossain, S. Mahmud, A. Dutta, I. Pop, Energy storage system based on nanoparticle-enhanced phase change material inside porous medium, International journal of thermal sciences, 91 (2015) 49-58.

[17] E.M. Sparrow, J.A. Broadbent, Inward melting in a vertical tube which allows free expansion of the phase-change medium, ASME Journal of Heat Transfer, 104 (1982) 309-315.

[18] C. Wenzhen, C. Shangmo, L. Zhen, G. Wangmin, Study of contact melting inside isothermally heated vertical cylindrical capsules, Journal of Thermal Science, 2 (1993) 190–195.

[19] Y.K. Wu, M. Lacroix, Melting of a PCM inside a vertical cylindrical capsule, International Journal for Numerical Methods in Fluids, 20 (1995) 559–572.

[20] B.J. Jones, D. Sun, S. Krishnan, S.V. Garimella, Experimental and numerical study of melting in a cylinder, International Journal of Heat and Mass Transfer, 49 (2006) 2724–2738.

[21] H. Shmueli, G. Ziskind, R. Letan, Melting in a vertical cylindrical tube: Numerical investigation and comparison with experiments, International Journal of Heat and Mass Transfer, 53 (2010) 4082–4091.

[22] S. Wu, H. Wang, S. Xia, D. Zhu, Numerical simulation on thermal energy storage behavior of cu/paraffin nanofluids PCMs, Procedia Engineering, 31 (2012) 240-244.

[23] A. Sciacovelli, F. Colella, V. Verda, Melting of PCM in a thermal energy storage unit: Numerical investigation and effect of nanoparticle enhancement, International Journal of Energy Research, 37 (2013) 1610-1623.

[24] L. Fan, Z. Zhu, Y. Zeng, Q. Lu, Z. Yu, Heat transfer during melting of graphene based composite phase change materials heated from below, International Journal of Heat and Mass Transfer, 79 (2014) 94-104.

[25] W.G. Alshaer, S.A. Nada, M.A. Rady, E. P. Del Barrio, A. Sommier, Thermal management of electronic devices using carbon foam and PCM/nano-composite, International Journal of Thermal Sciences, 89 (2015) 79-86.

[26] N. Das, Y. Takata, M. Kohno, S. Harish, Effect of carbon nano inclusion dimensionality on the melting of phase change nanocomposites in vertical shell-tube thermal energy storage unit, International Journal of Heat and Mass Transfer, 113 (2017) 423-432.

[27] M. Bechiri, K. Mansouri, Analytical study of heat generation effects on melting and solidification of nano-enhanced PCM inside a horizontal cylindrical enclosure, Applied Thermal Engineering, 104 (2016) 779–790.

[28] J. M. Mahdi, E. C. Nsofor, Solidification of a PCM with nanoparticles in triplex-tube thermal energy storage system, Applied Thermal Engineering, 108 (2016) 596–604.

[29] A. M. Abdulateef, S. Mat, J. Abdulateef, K. Sopian, A. A. Al-Abidi, Thermal performance enhancement of triplex tube latent thermal storage using fins-nano-phase change material technique, Heat transfer engineering, 0 (2017) 1-14.

[30] Y. Pahamli, M.J. Hosseini, A.A. Ranjbar, R. Bahrampoury, Effect of nanoparticle dispersion and inclination angle on melting of PCM in a shell and tube heat exchanger, Journal of the Taiwan Institute of Chemical Engineers, 81 (2017) 316–334.

[31] M. Parsazadeh, X. Duan, Numerical and statistical study on melting of nanoparticle enhanced phase change material in a shell-and-tube thermal energy storage system, Applied Thermal Engineering, 111 (2017) 950–960.

[32] J.M. Mahdi, E. C. Nsofor, Melting enhancement in triplex-tube latent thermal energy storage system using nanoparticles-fins combination, International Journal of Heat and Mass Transfer, 109 (2017) 417–427.

[33] M. Parsazadeh, X. Duan, Numerical study on the effects of fins and nanoparticles in a shell and tube phase change thermal energy storage unit, Applied Energy, 216 (2018) 142-156.

[34] S. Motahar, A. A. Alemrajabi, R. Khodabandeh, Experimental study on solidification process of a phase change material containing TiO_2 nanoparticles for thermal energy storage, Energy Conversion and Management, 138 (2017) 162–170.

[35] M. Arici, E. Tutuncu, M. Kan, H. Karabay, Melting of nanoparticle-enhanced paraffin wax in a rectangular enclosure with partially active walls, International Journal of Heat and Mass Transfer, 104 (2017) 7–17.

[36] S. Motahar, A. A. Alemrajabi, R. Khodabandeh, Experimental investigation on heat transfer characteristics during melting of a phase change material with dispersed TiO2 nanoparticles in a rectangular enclosure, International Journal of Heat and Mass Transfer, 109 (2017) 134–146.

[37] M. Al-Jethelah, S. H. Tasnim, S. Mahmud, A, Dutta, Melting of nano-PCM in an enclosed space: Scale analysis and heatline tracking, International Journal of Heat and Mass Transfer, 119 (2018) 841–859.

[38] S. Sharma, L. Micheli, W. Chang, A.A. Tahir, K.S. Reddy, T.K. Mallick, Nano-enhanced phase change material for thermal management of BICPV, Applied Energy, 208 (2017) 719-733.

[39] A. H.A. Al-Waeli, K. Sopian, M. T. Chaichan, H. A. Kazem, A. Ibrahim, S. Mat, M. H. Ruslan, Evaluation of the nanofluid and nano-PCM based photovoltaic thermal (PVT) system: An experimental study, Energy Conversion and Management, 151 (2017) 693–708.

[40] F. Bahiraei, A. Fartaj, G.A. Nazri, Experimental and numerical investigation on the performance of carbon-based nanoenhanced phase change materials for thermal management applications, Energy Conversion and Management, 153 (2017) 115–128.

[41] M. Hosseinzadeh, M. Sardarabadi, M. Passandideh-Fard, Energy and exergy analysis of nanofluid based photovoltaic thermal system integrated with phase change material, Energy 147 (2018) 636-647.

[42] S. Choi, S. Kim, T. Lee, D. Hahn, Computation of the natural convection of nanofluid in a squared cavity with homogeneous and nonhomogeneous models, Numerical heat transfer, 65 (2014) 287-301.

[43] S.P. Jang, S.U. Choi, Effects of various parameters on nanofluid thermal conductivity, ASME J. Heat transfer, 129 (2007) 617-623.

[44] A. Bejan, Convection Heat Transfer, Wiley, New York, 2013.

[45] J.M. Khodadadi, S.F. Hosseinzadeh, Nanoparticle-enhanced phase change materials (NEPCM) with great potential for improved thermal energy storage, International Communications in Heat and Mass Transfer 34 (2007) 534–543.

[46] S.F. Hosseinzadeh, A.A. Rabienataj Darzi, F.L. Tan, Numerical investigations of unconstrained melting of nano-enhanced phase change material (NEPCM) inside a spherical container, International Journal of Thermal Sciences 51 (2012) 77-83.

[47] N.S. Dhaidan, J.M. Khodadadi, T.A. Al-Hattab and S.M. Al-Mashat, Experimental and numerical investigation of melting of phase change material/nanoparticle suspensions in a square container subjected to a constant heat flux, International Journal of Heat and Mass Transfer, 66 (2013) 672-683.

[48] N.S. Dhaidan, J.M. Khodadadi, T.A. Al-Hattab and S.M. Al-Mashat, Experimental and numerical investigation of melting of NePCM inside an annular container under a constant heat flux including the effect of eccentricity, International Journal of Heat and Mass Transfer, 67 (2013) 455-468.

[49] N.S. Dhaidan, J.M. Khodadadi, T.A. Al-Hattab and S.M. Al-Mashat, Experimental and numerical study of constrained melting of n-octadecane with CuO nanoparticle dispersions in a

horizontal cylindrical capsule subjected to a constant heat flux, International Journal of Heat and Mass Transfer, 67 (2013) 523-534.

[50] N.S. Dhaidan, J.M. Khodadadi, T.A. Al-Hattab and S.M. Al-Mashat, Experimental and numerical investigation of melting of NePCM inside an annular container under a constant heat flux including the effect of eccentricity, International Journal of Heat and Mass Transfer, 67 (2013) 455-468.

[51] D. Groulx, P.H. Biwole, Solar PV passive temperature control using phase change materials, Proceedings of the 15th international heat transfer conference, IHTC-15, August 10-15, 2014, Kyoto, Japan.

[52] Y. Xu, M. Li, Z. Zheng, X. Xue, Melting performance enhancement of phase change material by a limited amount of metal foam: Configurational optimization and economic assessment, Applied Energy, 212 (2018) 868–880.

[53] C.J. Ho, J.Y. Gao, An experimental study on melting heat transfer of paraffin dispersed with Al_2O_3 nanoparticles in a vertical enclosure, International Journal of Heat and Mass Transfer, 62 (2013) 2-8.

[54] S.F. Hosseinizadeh, A.A.R. Darzi, F.L. Tan, Numerical investigations of unconstrained melting of nano-enhanced phase change material (NEPCM) inside a spherical container, International Journal of Thermal Sciences, 51 (2012) 77-83.

[55] T. Li, J. Lee, R. Wang, Y. Tae Kang, Heat transfer characteristics of phase change nanocomposite materials for thermal energy storage application, International Journal of Heat and Mass Transfer 75 (2014) 1–11.

[56] F.L. Tan, Constrained and unconstrained melting inside a sphere, International Communications in Heat and Mass Transfer, 35 (2008) 466–475.

References for Chapter 3

[1] A. Kumar, S.K. Shukla, A Review on thermal energy storage unit for solar thermal power plant application, Journal of Energy Procedia, 74 (2015) 462 - 469.

[2] B. Zalba, J. Marın, L.F. Cabeza, H. Mehling, A review on thermal energy storage with phase change materials: heat transfer analysis and applications, Applied Thermal Engineering, 23(2003) 251–283.

[3] G. Fang, H. Li, F. Yang, X. Liu, S. Wu, Preparation and characterization of nano-encapsulated *n*-tetradecane as phase change material for thermal energy storage, Journal of Chemical Engineering, 153 (2009) 217–221.

[4] N. Dhaidan, Nanostructures assisted melting of phase change materials in various cavities, Applied Thermal Engineering, 111 (2017) 193–212

[5] X. Zhang, X. Chen, Z. Han, W. Xu, Study on phase change interface for erythritol with nano-copper in spherical container during heat transport, International Journal of Heat and Mass Transfer, 92 (2016) 490–496.

[6] R.K. Sharma, P. Ganesan, V.V. Tyagi, H.S.C. Metselaar , S.C. Sandaran, Thermal properties and heat storage analysis of palmitic acid-TiO2 composite as nano-enhanced organic phase change material (NEOPCM), Applied Thermal Engineering, 99 (2016) 1254–1262.

[7] S. Zhang, J.Wu, C. Tse, J. Niu, Effective dispersion of multi-wall carbon nano-tubes in hexadecane through physiochemical modification and decrease of super cooling, Solar Energy Materials & Solar Cells, 96 (2012) 124–130.

[8] N. Dhaidan, J. Khodadadi, Melting and convection of phase change materials in different shape containers: A review, Journal of Renewable and Sustainable Energy Reviews, 43 (2015) 449–477.

[9] M. Jourabian, M. Farhadi, K. Sedighi, A. Rabienataj Darzi, Y. Vazifeshenas, Melting of NEPCM within a Cylindrical Tube: Numerical study using the Lattice Boltzmann Method, Numerical Heat Transfer, Part A: Applications, 61 (2012) 929-948.

[10] N. Dhaidan, J. Khodadadi, T. Al-Hattab, S. Al-Mashat, An experimental and numerical study of constrained melting of n-octadecane with CuO nanoparticle dispersions in a horizontal cylindrical capsule subjected to a constant heat flux, International Journal of Heat and Mass Transfer, 67 (2013) 523-534.

[11] M. Bechiri, K. Mansouri, Analytical study of heat generation effects on melting and solidification of nano-enhanced PCM inside a horizontal cylindrical enclosure, Applied Thermal Engineering, 104 (2016) 779-790.

[12] M. Jourabian, M. Farhadi, Melting of nanoparticles-enhanced phase change material (NEPCM) in a vertical semicircle enclosure: numerical study, Journal of Mechanical Science and Technology, 29 (9) (2015) 3819-3830.

[13] Y. Zeng, L. Fan, Y. Xiao, Z. Yu, K. Cen, An experimental investigation of melting of nanoparticle-enhanced phase change materials (NePCMs) in a bottom-heated vertical cylindrical cavity, International Journal of Heat and Mass Transfer, 66 (2013) 111-117.

[14] A. Sciacovelli, F. Colella, V. Verda, Melting of PCM in a thermal energy storage unit: numerical investigation and effect of nanoparticles enhancement, International journal of Energy Research, 37 (13) (2013) 1610–1623.

[15] H. Shamueli, G. Ziskind, R. Letan, Melting in a vertical cylindrical tubes: Numerical investigation and comparison with experiments, International Journal of Heat and Mass Transfer, 53 (2010)4082-4091.

[16] E. M. Sparrow, J.A. Broadbent, Inward melting in a vertical tube which allows free expansion of the phase-change medium, Journal of Heat Transfer, 104 (1982) 309-315.

[17] C. Wenzhen, C. Shangmo, L. Zhen, G. Wangmin, Study of contact melting inside isothermally heated vertical cylindrical capsules, Journal of Thermal Science, 2 (1993) 190-195.

[18] B. Jones, D. Sun, S. Kishan, S. Garimella, Experimental and numerical study of melting in a cylinder, International Journal of Heat and Mass Transfer, 49 (2006) 2724-2738.

[19] S. Ebadi, S.H. Tasnim, A.A. Aliabadi, S. Mahmud, Melting of nano-PCM inside a cylindrical thermal energy storage system: Numerical study with experimental verification, Energy Convers. Manag. 166 (2018) 241–259.

[20] C.J. Ho and J.Y. Gao, An experimental study on melting heat transfer of paraffin dispersed with Al2O3 nanoparticles in a vertical enclosure, International Journal of Heat and Mass Transfer 62 (2013) 2–8.

[21] M.M. Farid, A.M. Khudhair, S.A.K. Razack, S. Al-Hallaj, A review on phase change energy storage: materials and applications, Energy Convers. Manag. 45 (2004) 1597–1615.

[22] Li-Wu Fan, Zi-Qin Zhu, Yi Zeng, Q. Ding, Min-Jie Liu, Unconstrained melting heat transfer in a spherical container revisited in the presence of nano-enhanced phase change materials (NePCM), International Journal of Heat and Mass Transfer 95 (2016) 1057-1069.

[23] H. Shokouhmand, B. Kamkari, Experimental investigation on melting heat transfer characteristics of lauric acid in a rectangular thermal storage unit, Experimental Thermal and Fluid Science 50 (2013) 2001-2012.

[24] M. Al-Jethelah, S.H. Tasnim, S. Mahmud, A. Dutta, Nano-PCM filled energy storage system for solar-thermal applications, Renewable Energy, 126 (2018) 137-155.

[25] F.L. Tan, Constrained and unconstrained melting inside a sphere, International Communications in Heat and Mass Transfer, 35 (2008) 466–475.

References for Chapter 4 (Part I)

[1] N.S. Dhaidan, J.M. Khodadadi, Melting and convection of phase change materials in different shape containers: A review, Renewable and Sustainable Energy Reviews, 43 (2015) 449-477.

[2] M. Medrano, M.O. Yilmaz, M. Nogues, I. Martorell, J. Roca, L. Cabeza, Experimental evaluation of commercial heat exchangers for use as PCM thermal storage systems, Applied Energy, 86 (2009)2047-2055.

[3] Y. K. Wu, M. Lacroix, Melting of a PCM inside a vertical cylindrical capsule, 20 (1995) 559-572.

[4] B. Jones, D. Sun, S. Kishan, S. Garimella, Experimental and numerical study of melting in a cylinder, International Journal of Heat and Mass Transfer, 49 (2006) 2724-2738.

[5] H. Shmueli, G. Ziskind, R. Letan, Melting in a vertical cylindrical tube: Numerical investigation and comparison with experiments, International Journal of Heat and Mass Transfer, 53 (2010) 4082–4091

[6] S. Wang, A. Faghri, T. L. Bergman, Melting in Cylindrical Enclosures: Numerical Modeling and Heat Transfer Correlations, Numerical Heat transfer, 61 (2012) 837-859.

[7] A. Regin, S.C. Solanki, J.S. Saini, Latent heat thermal energy storage using cylindrical capsule: Numerical and experimental investigations, Renewable Energy, 32 (2006) 2025-2041.

[8] M. Mahdaoui, T. Kousksou, S. Blancher, A. Ait Msaad, T.El Rhafiki, M. Mouqalid, A numerical analysis of solid–liquid phase change heat transfer around a horizontal cylinder, Applied Mathematical Modelling, 38 (2014) 1101-1110.

[9] M.J.Hosseini, M.Rahimi, R.Bahrampoury**,** Experimental and computational evolution of a shell and tube heat exchanger as a PCM thermal storage system, International Communications in Heat and Mass Transfer, 50 (2014) 128-136.

[10] A. Soupart, J. Fourmigue, P. Marty, R. Couturier, Performance analysis of thermal energy storage systems using phase change material, Applied Thermal Engineering, 98 (2016) 1286-1296.

[11] Y. K. Wu, M. Lacroix, Melting of a PCM inside a vertical cylindrical capsule, 20 (1995) 559-572.

References for Chapter 4 (Part II)

[1] A. Kumar, S.K. Shukla, A Review on thermal energy storage unit for solar thermal power plant application, Journal of Energy Procedia, 74 (2015) 462 - 469.

[2] Zalba, J. Marın, L.F. Cabeza, H. Mehling, A review on thermal energy storage with phase change materials: heat transfer analysis and applications, Applied Thermal Engineering, 23(2003) 251–283.

[3] G. Fang, H. Li, F. Yang, X. Liu, S. Wu , Preparation and characterization of nano-encapsulated n-tetradecane as phase change material for thermal energy storage, Journal of Chemical Engineering, 153 (2009) 217–221.

[4] N. Dhaidan, Nanostructures assisted melting of phase change materials in various cavities, Applied Thermal Engineering, 111 (2017) 193–212.

[5] X. Zhang, X. Chen, Z. Han, W. Xu, Study on phase change interface for erythritol with nano-copper in spherical container during heat transport, International Journal of Heat and Mass Transfer, 92 (2016) 490–496.

[6] R.K. Sharma, P. Ganesan, V.V. Tyagi, H.S.C. Metselaar , S.C. Sandaran, Thermal properties and heat storage analysis of palmitic acid-TiO2 composite as nano-enhanced organic phase change material (NEOPCM), Applied Thermal Engineering, 99 (2016) 1254–1262.

[7] N. Dhaidan, J. Khodadadi, Melting and convection of phase change materials in different shape containers: A review, Journal of Renewable and Sustainable Energy Reviews, 43 (2015) 449–477.

[8] S. Wu, H. Wang, S. Xia, D. Zhu, Numerical simulation on thermal energy storage behavior of cu/paraffin nanofluids PCMs, Procedia Engineering, 31 (2012) 240-244.

[9] A. Sciacovelli, F. Colella, V. Verda, Melting of PCM in a thermal energy storage unit: Numerical investigation and effect of nanoparticle enhancement, International Journal of Energy Research, 37 (2013) 1610-1623.

[10] N. Das, Y. Takata, M. Kohno, S. Harish, Effect of carbon nano inclusion dimensionality on the melting of phase change nanocomposites in vertical shell-tube thermal energy storage unit, International Journal of Heat and Mass Transfer, 113 (2017) 423-432.

[11] Y. Zeng, L. Fan, Y. Xiao, Z. Yu, K. Cen, An experimental investigation of melting of nanoparticle-enhanced phase change materials (NePCMs) in a bottom heated vertical cylindrical cavity, International Journal of Heat and Mass Transfer, 66 (2013) 111-117.

[12] L. Fan, Z. Zhu, Y. Zeng, Q. Lu, Z. Yu, Heat transfer during melting of graphene based composite phase change materials heated from below, International Journal of Heat and Mass Transfer, 79 (2014) 94-104.

[13] M. Esapour, M.J. Hosseini, A.A. Ranjbar, R. Bahrampoury, Numerical study on geometrical specifications and operational parameters of multi-tube heat storage systems. Applied Thermal Engineering, 109, 351–363.

[14] Choi, S. Kim, T. Lee, D. Hahn, Computation of the natural convection of nanofluid in a squared cavity with homogeneous and nonhomogeneous models, Numerical heat transfer, 65 (2014) 287-301.

[15] A. Bejan, Convection Heat Transfer, Wiley, New York, 2013.

[16] C.J. Ho, J.Y. Gao, An experimental study on melting heat transfer of paraffin dispersed with Al_2O_3 nanoparticles in a vertical enclosure, International Journal of Heat and Mass Transfer, 62 (2013) 2-8.

[17] J.M. Khodadadi, S.F. Hosseinzadeh, Nanoparticle-enhanced phase change materials (NEPCM) with great potential for improved thermal energy storage, International Communications in Heat and Mass Transfer 34 (2007) 534–543.

[18] N.S. Dhaidan, J.M. Khodadadi, T.A. Al-Hattab and S.M. Al-Mashat, Experimental and numerical investigation of melting of phase change material/nanoparticle suspensions in a square container subjected to a constant heat flux, International Journal of Heat and Mass Transfer, 66 (2013) 672-683.

[19] D. Groulx, “Numerical study of nano-enhanced PCMs: Are they worth it?” Proceedings of the 1st Thermal and Fluid Engineering Summer Conference, TFESC August 9-12, 2015, New York City, USA

[20] F.L. Tan, Constrained and unconstrained melting inside a sphere, International Communications in Heat and Mass Transfer, 35 (2008) 466–47.

References for Chapter 5

[1] B. Zalba, J. Marın, L.F. Cabeza, H. Mehling, A review on thermal energy storage with phase change materials: heat transfer analysis and applications, Applied Thermal Engineering,23(2003) 251–283.

[2] A. Kumar, S.K. Shukla, A Review on thermal energy storage unit for solar thermal power plant application, Journal of Energy Procedia, 74 (2015) 462 - 469.

[3] N.S. Dhaidan, Nanostructures assisted melting of phase change materials in various Cavities, Applied Thermal Engineering, 111 (2017) 193–212.

[4] E. Osterman, V. Butala, U. Stritih, PCM thermal storage system for 'free' heating and cooling of buildings, Energy and Buildings, 106 (2015) 125–133.

[5] M. Kheradmand, M. Azenha, J. Aguiar, Experimental and numerical studies of hybrid PCM embedded in plastering mortar for enhanced thermal behaviour of buildings, Energy, 94 (2016) 250-261.

[6] V.V. Tyagi, A.K. Pandey, D. Buddhi, R. Kothari, Thermal performance assessment of encapsulated PCM based thermal management system to reduce peak energy demand in buildings, Energy and Buildings,117 (2016) 44–52.

[7] F. Guarino, A. Athienitis, M. Cellura, D. Bastien, PCM thermal storage design in buildings: Experimental studies and applications to solaria in cold climates, Applied Energy 185 (2017) 95–106.

[8] X. Xiao, P. Zhang, M. Li, Experimental and numerical study of heat transfer performance of nitrate/expanded graphite composite PCM for solar energy storage, Energy Conversion and Management, 105 (2015) 272–284.

[9] D.K. Singh , S. Suresh , H. Singh , B.A.J. Rose , S. Tassou , N. Anantharaman, Myo-inositol based nano-PCM for solar thermal energy storage, Applied Thermal Engineering, 110 (2017) 564–572.

[10] M. Faegh, M.B. Shafii, Experimental investigation of a solar still equipped with an external heat storage system using phase change materials and heat pipes, Desalination, 409 (2017) 128–135.

[11] A.E. Kabeel, M. Abdelgaied, Solar energy assisted desiccant air conditioning system with PCM as a thermal storage medium, Renewable Energy, 122 (2018) 632-642.
[12] R. Baby, C. Balaji, Experimental investigations on phase change material based finned heat sinks for electronic equipment cooling, International Journal of Heat and Mass Transfer, 55 (2012) 1642–1649.
[13] A. Arshad, H.M. Ali , M. Ali, S. Manzoor, Thermal performance of phase change material (PCM) based pin-finned heat sinks for electronics devices: Effect of pin thickness and PCM volume fraction, Applied Thermal Engineering, 112 (2017) 143–155.
[14] C. Kinkelin , S. Lips , U. Soupremanien , V. Remondière , J. Dijon , H. Poche , E. Ollier , M. Zegaoui , N. Rolland , P.A. Rolland , S. Lhostis , B. Descouts , Y. Kaplan , F Lefèvre, Theoretical and experimental study of a thermal damper based on a CNT/PCM composite structure for transient electronic cooling, Energy Conversion and Management, 142 (2017) 257–271.
[15] Y. Huo, Z. Rao, Investigation of phase change material based battery thermal management at cold temperature using lattice Boltzmann method, Energy Conversion and Management, 133 (2017) 204-215.
[16] S. Shi, Y. Xie, M. Li, Y. Yuan, J. Yu, H. Wu, B. Liu, N. Liu, Non-steady experimental investigation on an integrated thermal management system for power battery with phase change materials, Energy Conversion and Management, 138 (2017) 84-96.

[17] W. Wu, X. Yang, G. Zhang, K. Chen, S.Wang, Experimental investigation on the thermal performance of heat pipe-assisted phase change material based battery thermal management system, Energy Conversion and Management, 138 (2017) 486-492.

[18] N.S. Dhaidan, Nanostructures assisted melting of phase change materials in various cavities, Applied Thermal Engineering, 111 (2017) 193–212.
[19] N.S. Dhaidan, J.M. Khodadadi, Melting and convection of phase change materials in different shape containers: A review, Renewable and Sustainable Energy Reviews, 43 (2015)
449-477.

[20] G. Fang, H. Li, F. Yang, X. Liu, S. Wu, Preparation and characterization of nano-encapsulated *n*-tetradecane as phase change material for thermal energy storage, Journal of Chemical Engineering, 153 (2009) 217–221.

[21] N.S. Dhaidan, J.M. Khodadadi, T. A. Al-Hattab, S.M. Al-Mashat, Experimental and numerical investigation of melting of phase change material/nanoparticle suspensions in a square container subjected to a constant heat flux, International Journal of Heat and Mass Transfer, 66 (2013) 672–683.

[22] Y. Zeng, L. Fan, Y. Xiao, Z. Yu, K. Cen, An experimental investigation of melting of nanoparticle-enhanced phase change materials (NePCMs) in a bottom heated vertical cylindrical cavity, International Journal of Heat and Mass Transfer, 66 (2013) 111-117.

[23] L. Fan, J.M. Khodadadi, Thermal conductivity enhancement of phase change materials for thermal energy storage: A review, Renewable and Sustainable Energy Reviews, 15 (2011) 24-46.

[24] J.M. Khodadadi, L. Fan, H. Babaei, Thermal conductivity enhancement of nanostructure based colloidal suspensions utilized as phase change materials for thermal energy storage: A review, Renewable and Sustainable Energy Reviews, 24 (2013) 418-444.

[25] R. Hossain, S. Mahmud, A. Dutta, I. Pop, Energy storage system based on nanoparticle enhanced phase change material inside porous medium, International journal of thermal sciences, 91 (2015) 49-58.

[26] X. Zhang, X. Chen, Z. Han, W. Xu, Study on phase change interface for erythritol with nano-copper in spherical container during heat transport, International Journal of Heat and Mass Transfer, 92 (2016) 490–496.

[27] R. Baby, C. Balaji, Experimental investigations on thermal performance enhancement and effect of orientation on porous matrix filled PCM based heat sink, International Communications in Heat and Mass Transfer 46 (2013) 27–30.

[28] Z. Chen, D, Gao, J. Shi, Experimental and numerical study on melting of phase change materials in metal foams at pore scale, International Journal of Heat and Mass Transfer 72 (2014) 646–655.

[29] S. Mancin, A. Diani, L. Doretti, K. Hooman, L. Rosetto, Experimental analysis of phase change phenomenon of paraffin waxes embedded in copper foams, International Journal of Thermal Sciences 90 (2015) 79-89.

[30] S.H. Tasnim, R. Hossain, S. Mahmud, A. Dutta, Convection effect on the melting process of nano-PCM inside porous enclosure, International journal of heat and mass transfer, 85(2015) 206-220.
[31] M. Al-Jethelah, S.H. Tasnim, S. Mahmud, A. Dutta , Melting of nano-phase change material inside a porous enclosure , International journal of heat and mass transfer, 102 (2016)773-787.
[32] J. Yang, L. Lijun, C. Xu, X. Du, Experimental study on enhancement of thermal energy storage with phase-change material, Applied Energy 169 (2016) 164–176.
[33] Z. Zhang, X. He, Three-dimensional numerical study on solid-liquid phase change within open-celled aluminum foam with porosity gradient, Applied Thermal Engineering 113 (2017) 298–308.
[34] W. Li, H. Wan, H. Lou, Y. Fu, F. Qin, G. He, Enhanced thermal management with microencapsulated phase change material particles infiltrated in cellular metal foam, Energy, 127 (2017) 671-679.
[35] Z. Deng, X. Liu, C. Zhang, Y. Huang, Y. Chen, Melting behaviors of PCM in porous metal foam characterized by fractal geometry, International Journal of Heat and Mass Transfer 113 (2017) 1031–1042.
[36] M. Kohyani, B. Ghasemi, A. Raisi, S.M. Aminossadati, Melting of cyclohexane–Cu nano-phase change material (nano-PCM) in porous medium under magnetic field, Journal of the Taiwan Institute of Chemical Engineers, 77 (2017) 142–151.
[37] H. Zheng, C. Wang, Q. Liu, Z. Tian, X. Fan, Thermal performance of copper foam/paraffin composite phase change material, Energy Conversion and Management, 157 (2018) 372–381.
[38] M. Jourabian, M. Farhadi, A. R. Darzi, Constrained ice melting around one cylinder in horizontal cavity accelerated using three heat transfer enhancement techniques, International Journal of Thermal sciences, 125 (2018) 231-247.
[39] A. Siahpush, J. O'Brien, J. Crepeau, Phase change heat transfer enhancement using copper foam, ASME Journal of Heat Transfer, 130 (2008) .
[40] Z. Liu, Y. Yao, H. Wu, Numerical modeling for solid–liquid phase change phenomena in porous media: Shell-and-tube type latent heat thermal energy storage, Applied Energy, 112 (2013) 1222–1232.
[41] A. Atal, Y. Wang, M. Harsha, S. Sengupta, Effect of porosity of conducting matrix on a phase change energy storage device, International Journal of Heat and Mass Transfer, 93 (2016) 9–16.

[42] J. M. Mahdi, E. C. Nsofor, Melting enhancement in triplex-tube latent heat energy storage system using nanoparticles-metal foam combination, Applied Energy, 191 (2017) 22–34.
[43] Y. Xu, Q. Ren, Z. Zheng, Y. He, Evaluation and optimization of melting performance for a latent heat thermal energy storage unit partially filled with porous media, Applied Energy, 193 (2017) 84–95.
[44] Y. Xu, M. Li, Z. Zheng, X. Xue, Melting performance enhancement of phase change material by a limited amount of metal foam: Configurational optimization and economic assessment, Applied Energy, 212 (2018) 868–880.
[45] W.Q. Li, Z.G. Qu, Y.L. He, Y.B. Tao, Experimental study of a passive thermal management system for high-powered lithium ion batteries using porous metal foam saturated with phase change materials, Journal of Power Sources, 255 (2014) 9-15.
[46] F. Agyenim, N. Hewitt, P. Eames, M. Smyth, A review of materials, heat transfer and phase change problem formulation for latent heat thermal energy storage systems (LHTESS)
, Renewable Sustainable Energy Reviws. 14 (2010) 615-628.
[47] Z.G. Qu, W.Q. Li, W.Q. Tao, Numerical model of the passive thermal management system for high-power lithium ion battery by using porous metal foam saturated with phase change material, International journal of hydrogen energy, 39 (2014) 3904-3913.
[48] Z. Rao, Y. Huo, X. Liu, G. Zhang, Experimental investigation of battery thermal management system for electric vehicle based on paraffin/copper foam, Journal of the Energy Institute, 88 (2015) 241-246.
[49] Z.Wang, Z. Zhang, L. Jia, L. Yang, Paraffin and paraffin/aluminum foam composite phase change material heat storage experimental study based on thermal management of Li-ion battery, Applied Thermal Engineering, 78 (2015) 428-436.
[50] Z. Rao, Y. Huo, X. Liu, G. Zhang, Experimental investigation of battery thermal management system for electric vehicle based on paraffin/copper foam, Journal of the Energy Institute, 88 (2015) 241-246.
[51] M. Alipanah, X. Li, Numerical studies of lithium-ion battery thermal management systems using phase change materials and metal foams, International Journal of Heat and Mass Transfer, 102 (2016) 1159–1168.

[52] W.G. Alshaer, S.A. Nada , M.A. Rady , E. P. Del Barrio , A. Sommier, Thermal management of electronic devices using carbon foam and PCM/nano-composite, International Journal of Thermal Sciences, 89 (2015) 79-86.
[53] W.G. Alshaer , S.A. Nada , M.A. Rady , C. Le Bot , E. P. Del Barrio , Numerical investigations of using carbon foam/PCM/Nano carbon tubes composites in thermal management of electronic equipment, Energy Conversion and Management, 89 (2015) 873–884.

[54] S. Mousavi, A. Kasaeian, M.B. Sgafii, M.H. Jahangir, Numerical investigation of the effects of a copper foam filled with phase change materials in a water-cooled photovoltaic/thermal system, Energy Conversion and Management, 163 (2018) 187-195.

[55] A. Corbeil, ‘‘Study of Small Hydraulic Diameter Media for Improved Heat Exchanger Compactness, 2009,’’ MASc Thesis, University of Ottawa.

[56] J. Tian, T. Kim, T.J. Lu, H.P. Hodson, D.T. Queheillalt, D.J. Sypeck, H.N.G. Wadley, The Effects of Topology Upon Fluid-Flow and Heat-Transfer Within Cellular Copper Structures, International Journal of Heat and Mass Transfer, 47 (2004) 3171-3186.

[57] J. Xu, J. Tian, T.J. Lu, H.P. Hodson, On the thermal performance of wire-screen meshes as heat exchanger material, International Journal of Heat and Mass Transfer, 50 (2007) 1141–1154.

[58] R. Dyga, M. Placzek, Efficiency of heat transfer in heat exchangers with wire mesh packing, International Journal of Heat and Mass Transfer, 53 (2010) 5499–5508.
[59] R. Kurian, C. Balaji, S.P. Venkateshan, Experimental investigation of near compact wire mesh heat exchangers, Applied Thermal Engineering, 108 (2016) 1158–1167.
[60] Y. Fu, J. Wen, C. Zhang, An experimental investigation on heat transfer enhancement of sprayed wire-mesh heat exchangers, International Journal of Heat and Mass Transfer, 112 (2017) 699–708.
[61] A. Mustaffar, A. Harvey, D. Reay, Melting of phase change material assisted by expanded metal mesh, Applied Thermal Engineering, 90 (2015) 1052-1060.
[62] S.Z. Shuja, B.S. Yilbas, M.M. Shaukat, Melting enhancement of a phase change material with presence of a metallic mesh, Applied Thermal Engineering, 79 (2015) 163-173.

[63] W. Wu, X. Yang, G. Zhang, X. Ke, Z. Wang, W. Situ, X. Li, J. Zhang, An experimental study of thermal management system using copper mesh-enhanced composite phase change materials for power battery pack, Energy, 113 (2016) 909-916.

[64] Y. Azizi, S.M. Sadrameli, Thermal management of a LiFePO4 battery pack at high temperature environment using a composite of phase change materials and aluminum wire mesh plates, Energy Conversion and Management, 128 (2016) 294–302.

[65] L.C. Wei, J.A. Malen, Amplified charge and discharge rates in phase change materials for energy storage using spatially-enhanced thermal conductivity, Applied Energy, 181 (2016) 224–231.

[66] E.M. Alawadhi, Thermal analysis of a building brick containing phase change material, Energy and Buildings. 40 (2008) 351–357.

[67] www. americanelements.com/copper-mesh